HYBRID SEMICONDUCTOR FIBER LASERS FOR TELECOMMUNICATIONS

A DISSERTATION SUBMITTED TO THE DEPARTMENT OF ELECTRICAL ENGINEERING AND THE COMMITTEE ON GRADUATE STUDIES OF STANFORD UNIVERSITY IN PARTIAL FULFILLMENT OF THE REQUIREMENTS FOR THE DEGREE OF DOCTOR OF PHILOSOPHY IN ELECTRICAL ENGINEERING

Alireza Khalili

August 2006

I certify that I have read this dissertation and that in my opinion it is fully adequate, in scope and quality, as a dissertation for the degree of Doctor of Philosophy.

Prof. James S. Harris (Principal Advisor)

I certify that I have read this dissertation and that in my opinion it is fully adequate, in scope and quality, as a dissertation for the degree of Doctor of Philosophy.

Prof. Olav Solgaard

I certify that I have read this dissertation and that in my opinion it is fully adequate, in scope and quality, as a dissertation for the degree of Doctor of Philosophy.

Prof. Shanhui Fan

Approved for the University Committee on Graduate Studies.

Abstract

Highly stable edge emitting semiconductor lasers are of utmost importance in most telecommunications applications where high-speed data transmission sets strict limits on the purity of the laser signal. Unfortunately, most edge emitting semiconductor lasers, unlike gaseous or solid-state laser sources, operate with many closely spaced axial modes, which accounts for the observed instability and large spikes in the output spectrum of such lasers. Consequently, in most telecom applications distributed feedback (DFB) or distributed Bragg reflector (DBR) techniques are used to ensure stability and single-frequency operation, further adding to the cost and complexity of such lasers. Additionally, coupling of the highly elliptical output beam of these lasers to singlemode fibers complicates the packaging procedure and sub-micron alignment of various optical components is often necessary.

Utilizing the evanescent coupling between a semiconductor antiresonant reflecting optical waveguide (ARROW) and a side polished fiber, this thesis presents an alternative side-coupled laser module that eliminates the need for the cumbersome multi-component alignment processes of conventional laser packages, and creates an inherent mode selection mechanism that guarantees singlemode radiation into the fiber without any gratings. We have been able to demonstrate the first side-coupled fiber semiconductor laser in this technology, coupling more than 3mW of power at 850nm directly into a 5/125μm singlemode fiber. This mixed-cavity architecture yields a high thermal stability (~0.06nm/ºC), and negligible spectral spikes are observed. Theoretical background and simulation results, as well as several supplementary materials are also presented to further rationalize the experimental data. A side-coupled light-emitter and pre-amplifier are also proposed and discussed. We also study different architectures for attaining higher efficiency, higher output power, and wavelength tunability in such lasers. Finally, we discuss possible venues for integration of these side-coupled devices in a telecommunication system.

Acknowledgements

First and foremost, I have to thank my Lord, Allah, for granting me all I have, and for showing me the truth. He has bestowed upon me the greatest blessings I could ever ask for, and it is in his remembrance that I find peace and happiness.

I am personally indebted to my adviser, Professor James S. Harris, for granting me privilege of joining his research group. His distinct style and his unique personality have contributed most to successful completion of my graduate studies at Stanford. I would also like to thank the members of my reading committee: Professor Olav Solgaard and Professor Shanhui Fan. Despite their busy schedules, they were kind enough to read my thesis and offer me invaluable feedback. I also owe special thanks to Professor Philip Wong who kindly accepted to chair my defense committee. I am most grateful to Gail Chun-Creech for her continuous assistance and her administrative brilliance in these past years. I would like to thank my colleagues in the Harris group who helped me develop a better understanding of the physics and technology of III-V semiconductors. I am grateful to Luigi, Rafael, Vijit, Seth, Kai, Ke, Mike, Lynford, and Vince for many fruitful discussions. In particular, I would like to express my appreciation to Mark Wistey and Hopil Bae for helping me grow the wafers, and for teaching me the basics of the MBE. My time at Stanford would not have been as enjoyable without the company of many friends and colleagues who made this experience truly exceptional. Special thanks go to Yashar, Mehdi, Mohsen, Pooya, Reza, Amir, Hamid, Vahbod, and Ali's.

I wish to thank my wife, Marzieh, for her love and support throughout the past two years. I have been most fortunate to have had her by my side. I would also like to express my gratitude to my parents for devoting all their life for the betterment of their children. I could not have accomplished anything without their constant care and support. Finally, I would like to dedicate this thesis to the memory of my late father, Mohammad Kazem. His sudden loss, at the time of this writing, left us in deep sorrow and lasting pain. May God bless his soul.

Table of Contents

List of Tables

List of Illustrations

Chapter 1

Introduction

1.1 History

The advent of optical networking technologies in the past decades has caused a dramatic increase in the capacity of telecommunication networks. Optical fibers are now the building blocks for long haul, metropolitan and many local area networks. The unique characteristics of fibers, namely large bandwidth, low attenuation, and immunity to electromagnetic interference, have made them the medium of choice for today's telecommunications. Moreover, with the aid of several newly-developed enabling technologies, optical fibers have been transformed from a mere propagation medium into an intelligent network layer with various functionalities. One notable breakthrough came with the introduction of Wavelength Division Multiplexing (WDM) techniques, which increased the capacity of a singlemode fiber beyond 1THz and set the standard for most optoelectronic devices. Different carrier wavelengths are employed in WDM channels not only to enhance the network bandwidth, but also to realize a communication layer that can intelligently route data based on the color of incoming light. In recent years, many highly sophisticated optoelectronic devices, including some photonic integrated circuits (PIC), have emerged to perform needed operations on the WDM signals. Although the idea of a full-scale PIC has been extensively pursued by many researchers, nothing analogous to the electronic ICs has been accomplished to date. Lack of a truly versatile substrate, such as silicon, for optoelectronic applications, along with the high cost and complexity of fabrication and integration of optics has slowed down the growth of PICs and until recently[1] a completely integrated optical solution was very rare. Unfortunately, most optical networking devices are not fabricated on the same, or even similar substrates[2,3,4,5].

Consequently, manufacturers have tried to fabricate fiber-coupled modules to make products suitable for network integration. Such integration of optical components and fibers is very difficult to do in free space, and the alignment costs contribute significantly to the price of the final package. In the so-called "butt-coupling" approach, which is presently the dominant method for fabricating fiber-coupled modules, the fiber is cut and devices are placed in the gap between the cleaved tips of the fiber. Since the coupling takes place in free space, the alignment and packaging process involved is typically costly and complex. This integration method is depicted in Figure 1.1.

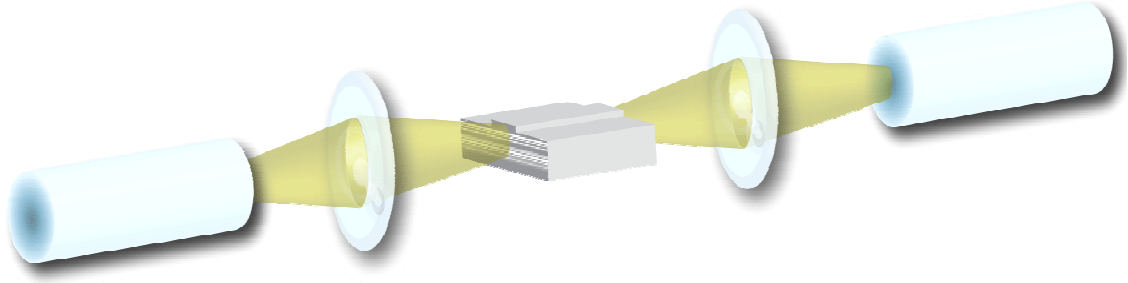

Figure 1.1: The conventional method of fabricating free-space fiber coupled modules.

Edge-emitting semiconductor lasers, in particular, are more difficult to integrate with singlemode fibers, not only because of their small mode diameters, but also due to the elliptical beam shapes of such lasers. Precision placement of various optical components, including aspheric lenses, is therefore crucial for obtaining good coupling efficiency and low insertion loss in these systems, as shown in Figure 1.2.

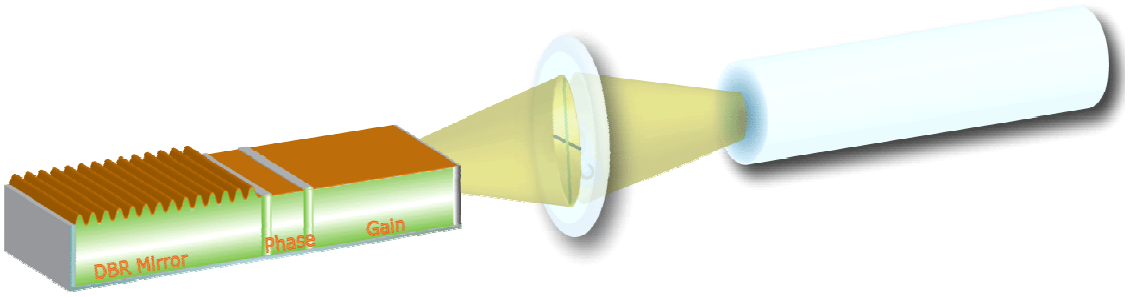

Figure 1.2: Coupling from a semiconductor laser to a singlemode fiber.

Alternatively, an "evanescent coupling" approach, which does not involve the termination of fiber and avoids the foregoing complexities, has also been used in certain applications such as directional couplers[6,7], arrayed waveguide gratings[8], and waveguide modulators[9]. This concept is pictured in Figure 1.3. The alignment tolerance in these systems is more relaxed than in butt-coupled modules, and can be easily satisfied in most conventional semiconductor processing technologies. However, due to the large index contrast between semiconductor waveguides and fibers, this method thus far has found only limited use in semiconductor-based devices.

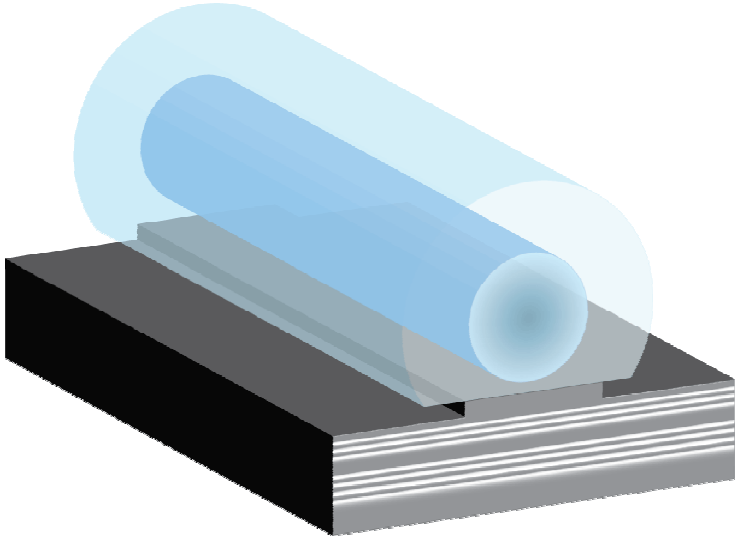

Figure 1.3: The schematic of an evanescently coupled fiber-waveguide system.

Although conventional semiconductor waveguides cannot be used for evanescent coupling to silica fibers, antiresonant reflecting optical waveguides[10] (ARROWs) can attain arbitrarily low propagation indices and can thus be used in such architectures. Moreover, ARROWs can be coupled evanescently to silica waveguides, such as in a PIC depicted in Figure 1.4. Such side-coupled devices can be used in a telecommunication link for a variety of different operations such as light emission[11], modulation, and detection. A whole WDM transmit-receive module can be easily conceptualized, once the individual functionalities are implemented.

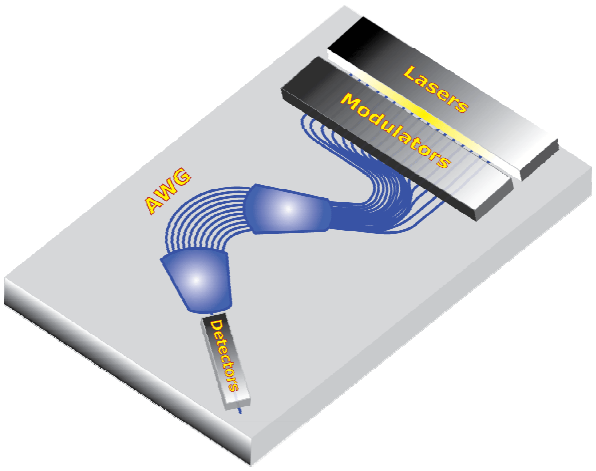

Figure 1.4: A conceptual telecom system made of evanescently coupled laser, modulator, and detector chips, flip-chip-bonded to a silica arrayed-waveguide-grating chip

Passive coupling and modulation of the fiber signal by the semiconductor were previously demonstrated[12,13]. Generating light in the semiconductor and coupling it to the fiber, on the other hand, proved to be far more challenging and very limited amount of coupling was observed[14]. In this thesis, we present a highly stable, integrated fiber-semiconductor laser that benefits from the narrowband evanescent coupling between an ARROW waveguide and a side-polished fiber, while avoiding the foregoing alignment and packaging complexities of the conventional modules.

1.2 Thesis organization

This thesis is organized as follows. In chapter 2, we review the theoretical background of this work. The hybrid ARROW-fiber system is analyzed in more detail in chapter 3. The initial light emission experiments are described in chapter 4, while chapter 5 reviews amplifier designs and simulations. The side-coupled fiber laser architectures are studied extensively in chapter 6 and the experimental data are presented to verify the theories. We finally conclude this thesis in chapter 7. The fabrication process and the ARROW epitaxial design are further elaborated in Appendices A and B.

Chapter 2

Theoretical background

This chapter serves as an overview of the underlying physics of the devices presented in this thesis. We briefly describe optical fibers and waveguides, evanescent coupling methods, and semiconductor lasers. At the end of this chapter we also review the simulation tools that are extensively used in this research.

2.1 Optical fibers

A conventional optical fiber is a cylindrical waveguide that confines and guides the light in its core through total internal reflections from the core-cladding interface. These core and cladding layers are typically made of ultrahigh-purity silica that is highly transparent in the infrared frequency band used in telecommunications. Confinement is produced by a slightly higher refractive index in the core than the cladding of the fiber, due to a small doping in the core. Signal attenuation in conventional glass fibers is mostly determined by Rayleigh scattering and multi-phonon absorption at different wavelengths. For silica fibers, the minimum loss at 1.5-1.6μm can be as low as 0.2dB/km.

Several other kinds of optical fibers exist for different applications. While conventional fibers do not preserve the signal polarization, polarization-maintaining (PM) fibers can achieve this by using stress-induced birefringence. Moreover, photonic crystal fibers[15] (or holey fibers) use small air holes instead of or in addition to the cladding, to effectively confine the light in the resulting bandgap structure. Such fibers are particularly useful in nonlinear or high power applications.

2.1.1 Multimode fibers

Multimode fibers have large core diameters and high index contrasts. Consequently, they support numerous modes that can travel concurrently with low loss. Given that such modes propagate at different speeds, these fibers are particularly prone to group delay dispersion and severe pulse-broadening occurs after rather small distances (typically ~100m for 10Gbs signal). To mitigate this effect, the index profile may be graded to reduce the dispersion. An important figure of merit for optical fibers is their numerical aperture (NA). NA is defined as the sine of the largest angle (θ_{max} with respect to the fiber axis), at which light can directly couple into a fiber from air. In a step-index fiber the NA is defined as:

$$\mathrm{NA} = \sin\theta_{\max} = \sqrt{n_{core}{}^2 - n_{clad}{}^2}$$

where n_{core} and n_{clad} stand for the core and cladding indices of the fiber. Multimode fibers have relatively large NA (~0.3), which together with their large core area make coupling into these optical waveguides a relatively easy task. Core diameters usually range from 50-100μm in such fibers. It is also worthwhile to study the normalized frequency or the V-number, which is defined as:

$$\mathrm{V} = ak_0\sqrt{n_{core}{}^2 - n_{clad}{}^2} \qquad k_0 = \frac{2\pi}{\lambda_0}$$

where λ_0 is the wavelength of light in air. This parameter can be used to quickly estimate the total number of modes in a fiber. It is possible to show that:

$$N = 4\frac{\mathrm{V}^2}{\pi^2} \qquad (\text{for} \quad \mathrm{V} >> 1)$$

where N is the number of confined modes. A fiber will be singlemode when V<2.405.

2.1.2 Singlemode fibers

To make a fiber singlemode, the refractive index of the core and cladding are chosen close enough to guarantee that only one mode is guided or constrained by the fiber. Since the V-number of singlemode fibers is less than 2.405, the NA and the core diameter trade directly with each other, making coupling into and out of these fibers

extremely difficult. Core diameters are usually smaller than 10μm, while NA values around 0.12 are typical in such fibers.

In order to find the modes of an optical fiber, or in general any optical waveguide, one needs to solve the wave equations in the core and cladding media and satisfy the boundary conditions:

$$\nabla^2 \vec{E} + k_0^2 n_{(x,y)}^2 \vec{E} = \beta^2 \vec{E}$$

where $n_{(x,y)}$ is the 2D index profile and β is the propagation constant in the z-direction. Such calculations can be found elsewhere[16] and will not be repeated here. These analytical solutions include Bessel functions and are, in general, complicated expressions of fiber parameters. However, there are valid empirical formulas that can be used in practice with reasonable accuracy to model step-index fibers. In particular, the electric field distribution for the lowest-order HE_{11} mode can be approximated with a Gaussian-envelope close to the cutoff frequency:

$$E(r) = E_0 e^{-\frac{r^2}{w^2}} \qquad \left(\frac{w}{a} = 0.65 + 1.619\mathrm{V}^{-1.5} + 2.87\mathrm{V}^{-6} \right)$$

where r is the distance from the center of the fiber, a is the core radius, and w is the mode-field radius, which is defined as the radius at which the electric field is reduced to e^{-1} of its maximum. Figure 2.1 depicts the relative electric field distribution of this mode for a singlemode fiber.

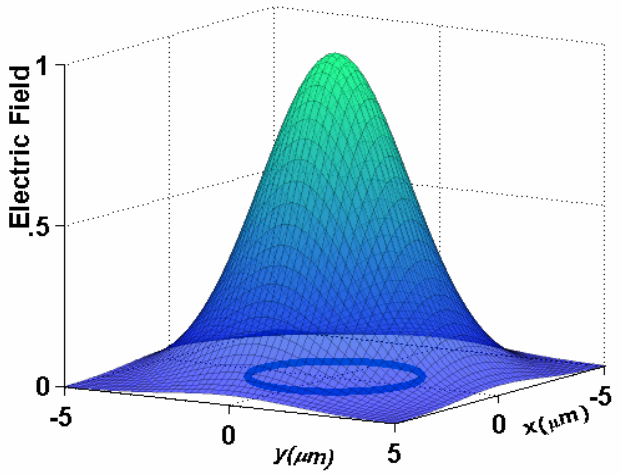

Figure 2.1: the electric field distribution in a singlemode fiber (outlined) at 850nm. z-axis has arbitrary units. The fiber parameters are: $n_{core} = 1.458336$, $n_{clad}=1.45253$, and $a = 2.27\mu m$. This fiber has a cutoff wavelength of ~780nm.

The following empirical formula gives the effective wave-number (β) of this mode:

$$\beta = \sqrt{k_0^2 n_{core}^2 - \frac{V^2 - (1.1428V - 0.996)^2}{a^2}} \qquad 1.5 \le V \le 2.5$$

2.1.3 Coupling to fibers

Coupling to fibers, especially to singlemode fibers, can be very complex. The small mode-field diameter often necessitates sub-micron alignment accuracies, which further complicates the free-space coupling procedures, as mentioned before. For a semiconductor laser this coupling is typically carried out in a butterfly package as depicted in Figure 2.2, where various components including lenses, isolators, and the monitoring devices are aligned and fixed in a hermetic package. The end result can therefore be far more expensive than the cost of the laser chip alone.

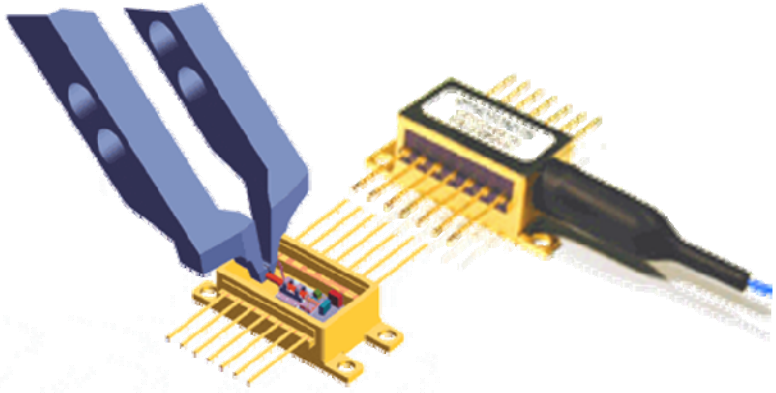

Figure 2.2: Component alignment in a butterfly package.

2.2 Optical waveguides

While fibers benefit from the ease of fabrication and the low loss of silica, they are not well suited for integrated optoelectronic applications. Instead, rectangular waveguides fabricated on semiconductor or glass substrates are widely used in most integrated PICs. A ridge waveguide is depicted in Figure 2.3.

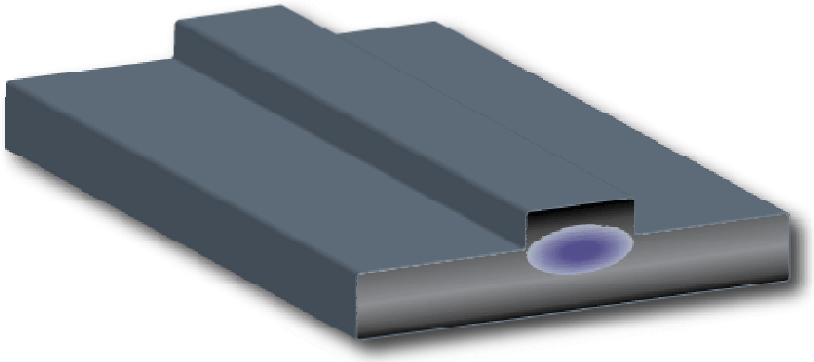

Figure 2.3: A ridge waveguide structure and sample mode profile.

Expectedly, total internal reflection is also the main confinement mechanism in these waveguides. While analytical solutions to the wave equation exist for some simple structures[16], most practical waveguides cannot be analyzed as easily. Instead, approximation methods, like the effective-index method, can be used in conjunction with simple one-dimensional analytical results to solve more general waveguide architectures. The accuracy of this approach nonetheless depends on how strongly the mode is guided and in more complicated structures a field-solver is typically required. Finite element[17], or finite difference[18] methods are generally invoked in such simulations to calculate the field distribution of an arbitrary waveguide structure.

2.3 Evanescent coupling basics

Evanescent coupling has long been used in optical devices, such as directional couplers and waveguide modulators. In this section we review this method and analyze an evanescently-coupled waveguide system. There are many books that describe the evanescent coupling theory[19], and the reader is referred to such texts for further detail.

2.3.1 Twin waveguides

A simple one-dimensional symmetrical waveguide structure is shown in Figure 2.4.

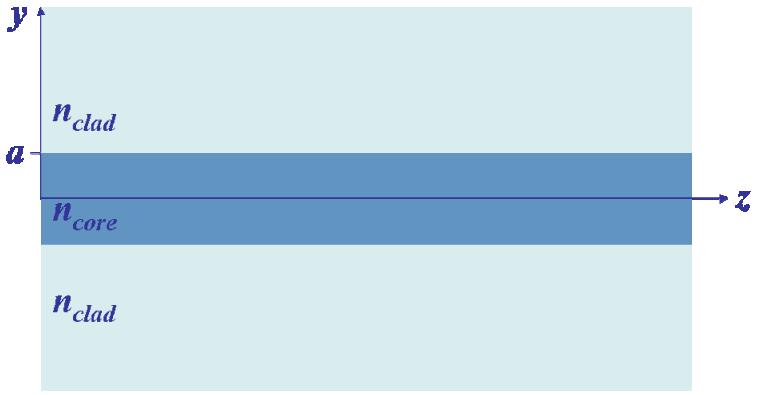

Figure 2.4: A 1D symmetrical slab waveguide.

To develop an intuition into the coupling mechanism, we first solve the scalar wave equation in this planar waveguide. For TE modes, the field-equations take a simple form in the corresponding regions:

$$Core: \quad \partial_x^2 E + k_0^2 n_{core}^2 E = \beta^2 E$$
$$Cladding: \quad \partial_x^2 E + k_0^2 n_{clad}^2 E = \beta^2 E$$

It is easy to prove that these equations have an e^{sx} solution in both regions. For a guiding mode however, s is imaginary in the core region and real in the cladding:

$$Core: \quad E = E_0 e^{\pm j\alpha x} \quad \alpha = \sqrt{k_0^2 n_{core}^2 - \beta^2} \quad |x| \le a$$
$$Cladding: \quad E = E_1 e^{\pm \gamma x} \quad \gamma = \sqrt{\beta^2 - k_0^2 n_{clad}^2} \quad |x| \ge a$$

where $k_0 n_{clad} \le \beta \le k_0 n_{core}$. The continuity condition of the electric field at the core-cladding interface determines the unknown parameters. The eigenvalue equation for β becomes:

$$\tan(2a\alpha) = \frac{2\gamma}{\alpha(1 - \frac{\gamma^2}{\alpha^2})}$$

where $2a$ is the core slab thickness. Depending on the waveguide index and thickness, this equation can have one or more solutions at any given wavelength. Figure 2.5 depicts the resulting electric field profile of an arbitrary mode (m=3) in this waveguide:

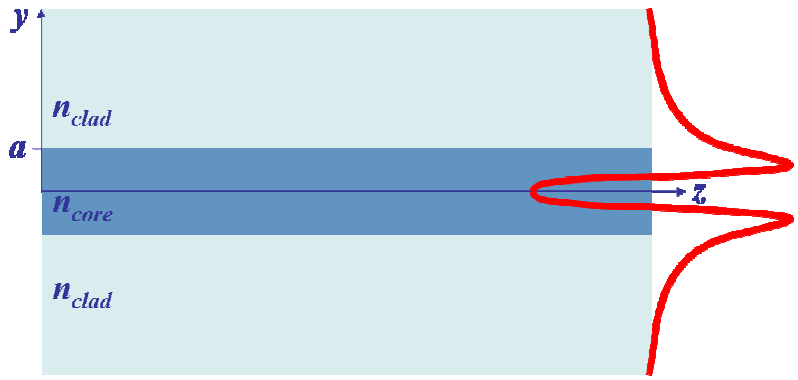

Figure 2.5: The lateral distribution of the electric field profile in an arbitrary mode (m=3) of the 1D slab waveguide.

It is possible to show that the solution in the core region can be decomposed into two simple plane waves traveling at angles $\theta = \pm \sin^{-1}(\alpha / k_0 n_{core})$ with respect to *z*-axis, consistent with the ray picture. On the other hand, the electric field decays exponentially in the cladding layers and the signal power is therefore confined in the center. Although there is no perpendicular flow of energy in the evanescent portion of the modes; insertion of a high-index layer can significantly alter this situation. In fact, in the case of twin waveguides shown in Figure 2.6, it is possible to show that a symmetric and an antisymmetric solution exist for every mode of the single waveguide structure. These new modes (eigenmodes of the coupled system) result from the interaction between the evanescent tails of the original modes with the adjacent waveguide.

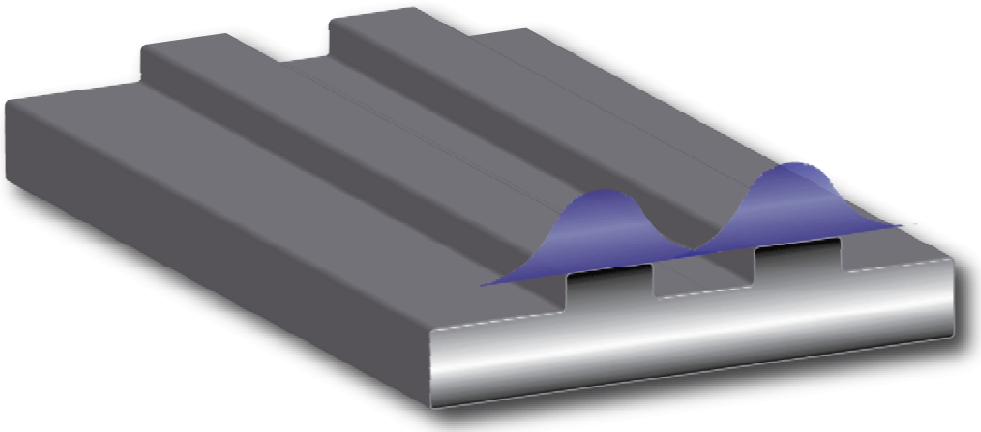

Figure 2.6: Overlapping modes of twin waveguides.

While analyzing the whole system can yield the exact solutions, it is possible to estimate the shape and indices of such modes in the weak-coupling regime by applying perturbation techniques to the wave equations. In this case, it is possible to show that the symmetric and antisymmetric modes of the coupled system can be described as a superposition of the modes in each waveguide:

$$E_S = \frac{1}{\sqrt{2}}\left(E_{wg1} + E_{wg2}\right)$$

$$E_A = \frac{1}{\sqrt{2}}\left(E_{wg1} - E_{wg2}\right)$$

where E_S and E_A stand for the transverse electric field distribution of the symmetric and antisymmetric modes, respectively, and E_{wg1} and E_{wg2} are the individual mode profiles of each waveguide. As the distance between the waveguides is reduced, the effective index of these modes deviates farther from the original values. These changes have important implications that will be studied more closely in the context of coupled-mode equations later in this document.

Assuming that the power is initially coupled to the first waveguide, the input field can be expressed as: $E_{in} = E_{wg1} \propto \left(E_S + E_A\right)$. The field distribution in this system at distance z from origin is therefore:

$$E_{(z)} \propto \left(E_S e^{-j\beta_S z} + E_A e^{-j\beta_A z}\right) \propto e^{-j\bar{\beta}.z}\left(E_{wg1}\cos(\frac{\Delta\beta.z}{2}) - iE_{wg2}\sin(\frac{\Delta\beta.z}{2})\right)$$

where $\bar{\beta}$ and $\Delta\beta$ are the average and difference of the symmetric (β_S) and antisymmetric (β_A) wavenumbers. Obviously, this difference ($\Delta\beta$) causes a progressive phase shift between the odd and even components of the optical beam that results in a complementary sinusoidal modulation of the original mode amplitudes in each waveguide. At all odd multiples of the coupling distance, defined as $l_{coupling} = \pi/\Delta\beta$, the modes interfere destructively at the original location and:

$$E_{((2m+1)l_{coupling})} \propto \left(E_S - E_A\right) \propto E_{wg2}$$

indicating that power is effectively transferred to the second waveguide. This beating behavior is depicted in Figure 2.7.

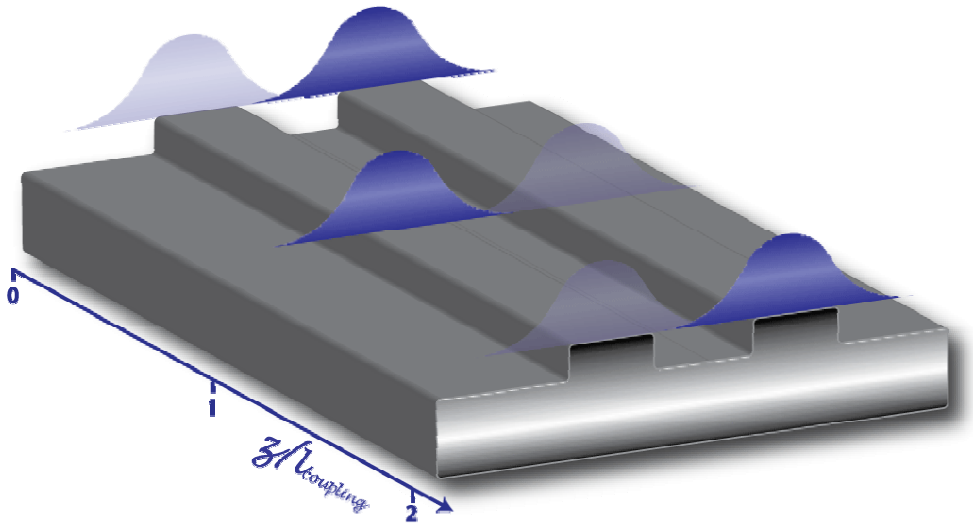

Figure 2.7: Illustration of the evanescent coupling as a function of normalized interaction length ($z/l_{coupling}$) in a twin-waveguide structure.

The index difference can be calculated, in the first order, by the overlap integral of the electric fields in these waveguides. While the exact algebra is found elsewhere[16], we quote the results without proof:

$$\kappa = \frac{(\beta_S - \beta_A)}{2} = \frac{k_0^2}{2\beta} \frac{\int (\Delta n^2 E_{wg1} E_{wg2}) dy}{\sqrt{(\int |E_{wg1}|^2 dy) \cdot (\int |E_{wg1}|^2 dy)}}$$

where κ is the coupling coefficient and Δn^2 is the perturbing permittivity caused by the second waveguide. These overlap integrals are used extensively in practice, since they provide a good approximation and valuable intuition into the coupling mechanism. It is worthwhile to note that such analysis tends to become invalid when the spacing between the waveguides becomes extremely small. In the strong coupling limit, the mode shapes change significantly due to strong loading effects and perturbation approximations will not hold.

2.3.2 Phase matching

The evanescent coupling method is not limited to identical waveguides. In general, coupling could happen between any two waveguide structures, once the phase-matching condition is satisfied[19]:

$$\beta_{wg1} = \beta_{wg2}$$

Under this condition, the interacting modes stay in phase as they travel along the waveguides and the foregoing analysis can be applied to these systems as well. Similarly, the index difference between symmetric and antisymmetric modes in such media results in the familiar spatial-swinging of power back and forth between the two waveguides in the propagation direction.

2.3.3 Coupled-mode systems

The behavior of a weakly coupled system can be simply modeled by these 1st-order linear coupled-mode equations[20]:

$$\partial_z A = -j\kappa B e^{jz\Delta\beta}$$
$$\partial_z B = -j\kappa A e^{-jz\Delta\beta}$$

where A and B are the amplitudes of the electric field in the first and second waveguides, respectively. κ is again the coupling coefficient, and $\Delta\beta$ is the difference between the k-vectors of two waveguides (zero at phase-matching). The solution under phase-matching conditions (for $A(0)=1$, $B(0)=0$) becomes:

$$A(z) = \cos(\kappa z)$$
$$B(z) = -j\sin(\kappa z)$$

which is similar to the oscillatory behavior derived in the previous section. If the coupled length is larger than the coupling length ($l_{coupling} = \pi/2\kappa$), the signal will start to couple back to the original waveguide. This overcoupling phenomenon is an important characteristic of these lossless coupled systems. When $\Delta\beta \neq 0$, the coupling quickly fades as the interacting waves will not retain their phase relationship over the propagation distance.

2.4 Semiconductor lasers

Semiconductor lasers were first realized in the early 60's. Original devices were cryogenic, operated with narrow pulses, and had very short lifetimes. However, today these devices are the best-selling type of lasers, thanks to the remarkable

progress in the material growth and fabrication techniques. Currently, semiconductor lasers cover a wide range of frequencies, can generate ultra-high powers[21], and can be tailored for high speed applications. This section provides a brief overview of this technology.

2.4.1 Introduction

A diode laser, as the name suggests, includes a p-i-n diode that is fabricated by epitaxial growth of semiconducting material on lattice-matched substrates. The current flowing through the forward-biased p-n junction creates electron and hole pairs in the depletion region, which can participate in the stimulated emission process and provide a gain medium for the optical signal. Like any other laser, semiconductor diodes need a resonant cavity and a saturation mechanism, in addition to the gain medium, to facilitate lasing. The cavity resonance is provided by placing mirrors on either side of the cavity in a Fabry-Perot etalon architecture. The mirrors are typically realized by the cleaved semiconductor facets or through a distributed Bragg reflector.

2.4.2 Population inversion in semiconductors:

Like other types of lasers, the semiconductor needs to reach population inversion in order for the stimulated emission and gain processes to dominate loss and absorption. Quantitatively, the gain in a semiconductor material can be expressed as[22]:

$$g = \frac{\pi e^2 \hbar}{n \varepsilon_0 c m_0^2} \frac{|M_T(E_{21})|^2}{E_{21}} \rho_r(E_{21})(f_2 - f_1)$$

where g is the gain per unit length of the semiconductor, f_2, and f_1 are the probabilities of finding a filled electron state in the conduction and valence band, respectively, and ρ_r and $|M_T|$ are the reduced density of the states and the matrix element corresponding to this transition energy (E_{21}). Consequently, for positive gain, f_2-f_1>0, and the carrier population between conduction and valence band should be inverted. It is easy to prove that in a semiconductor material, the difference between the electron and hole quasi-Fermi levels should exceed the band gap energy (F_n-F_p>E_{bg}) to achieve inversion. In homojunction lasers, where all the layers are made from the same

material, this condition is extremely hard to satisfy, as the required doping levels to reach degeneracy in the semiconductor may get prohibitively large. Moreover, the current density required to pump these devices beyond the transparency limit is too high (typically ~10kA/cm^2). In addition, the unpumped material beyond the depletion region will greatly absorb the optical signal; therefore even larger currents are required to further extend the depletion area (~1μm) and subdue this tail loss. Fortunately, a breakthrough came with the introduction of heterostructure lasers in the late 1960's. Not only did this technique solve the foregoing issues, it also added some electrical and optical features to these lasers that dramatically improved their performance. As a result, the threshold current densities of current diode lasers are lower by multiple orders of magnitude and the electrical-to-optical power conversion efficiencies (*a.k.a.* wall-plug efficiencies) are close to unity. These hetero-junction lasers are primarily grown by epitaxial growth of multi-layer lattice-matched semiconductors, *e.g.* AlGaAs/GaAs or GaInAsP/InP, to provide defect-free junctions and materials that significantly improve the efficiency and lifetime of these devices.

2.4.3 Double heterostructure lasers

In a double-heterostucture (DH) laser diode, an intrinsic narrow-bandgap material is sandwiched between n- and p-doped, wider bandgap materials. The small-bandgap material can be easily inverted here, as the potential barriers at the hetero-interface trap the carriers inside this material and reduce the otherwise-dominating diffusion of carriers out of this region. Moreover, not only is the wide-bandgap material transparent at the emission frequency of the laser (equal to the smaller bandgap energy), it also has a lower index of refraction that improves waveguiding and interaction between the optical wave and the gain region. Although the active region can be significantly thinner in DH lasers than in homojunction devices, the overlap integral between the optical wave and the gain region can diminish considerably at distances below 0.1μm, resulting in an increase in the laser threshold current density in these diodes. To quantify this effect, we can define a confinement factor (Γ) that captures this gain/field overlap:

$$\Gamma \approx \frac{\int_G EE^* n dx}{\int EE^* n_0 dx}$$

where n is the material index function, and n_0 is the propagation index of the mode. The numerator integral is calculated over the gain region, while the denominator is integrated over all the space. The modal gain is therefore: $g_{mode}=\Gamma.g_{material}$

2.4.4 Quantum well lasers

Apart from the clear advantages of these simple double-heterostructure lasers, they also have a few shortcomings that limit their applications. For one, the spectral location of the gain peak moves significantly as the pump current increases. This is due to the fact that the 3D density of states in these materials is proportional to the square root of energy (E-E_{bg}), so the wavelength with the highest gain varies considerably at different carrier densities. Moreover, to get gain at different wavelengths in a simple DH laser, one has to change the material composition of the active region, which is highly undesirable from the fabrication standpoint.

The addition of quantum wells (QWs) to the DH structure was the second breakthrough in realizing low-threshold, highly-efficient lasers. Since the quantum well thickness is very small (~10nm), the required threshold current for inversion is significantly lower than DH lasers. Moreover, because the 2D density of states in QW has a stairlike pattern, the gain spectrum peak is very strong and moves slowly with current[22]. Despite the small confinement factor the overall gain can be reasonably high, which justifies the popularity of QW lasers. Additionally, the QW thickness can be used to vary the energy levels; therefore gain wavelength can be tuned independently by adjusting the well thickness rather than its composition.

2.4.4.1 850nm quantum well design

In this section we try to design a QW with a peak gain at 850nm. We choose GaAs as the QW material (bandgap=1.424eV). The classical formula for the first energy levels of an arbitrary QW (bound by infinite potential barriers) is:

$$E_1 = \frac{\hbar^2 \pi^2}{2ma^2}$$

where m is the carrier effective mass and a is the quantum well thickness. In reality however, the barriers are finite (for $Al_{0.20}Ga_{0.80}As$, E_{bg}=1.673eV) and the band energy is smaller than predicted by this calculation. This can be easily simulated by a computer program (using resonant tunneling and transfer matrix algorithms) to find the appropriate QW thickness for a desired wavelength. Figure 2.8 depicts the first transition wavelength (between first heavy-hole and electron bands) in such a QW as a function of its thickness.

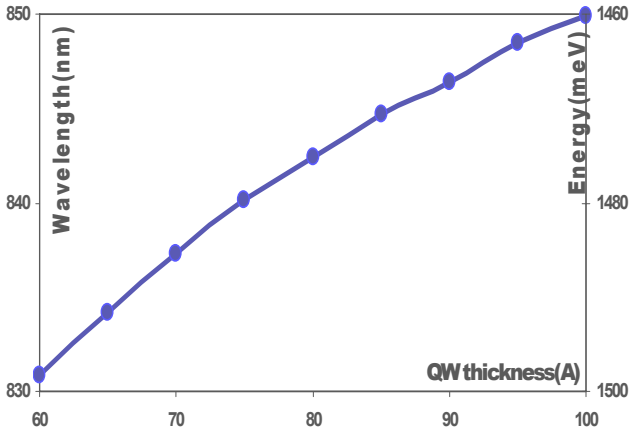

Figure 2.8: Wavelength of the first allowed transition as a function of thickness in a GaAs/ $Al_{0.20}Ga_{0.80}As$ quantum well.

According to this curve, for 850nm operation a thickness of ~100Å is required. In reality, however, several phenomena change the location of the gain peak from this number. Most importantly, carrier-induced bandgap shrinkage and junction heating tend to redshift (*i.e.* shift to longer wavelengths) the location of gain peak in these lasers. While theoretical analysis can be found elsewhere[22], a 10nm margin was empirically found to account for these redshifts. The optimal QW thickness is therefore ~80Å. Fortunately, this wavelength is quite insensitive to growth offset as shown in the figure.

The following empirical formula is typically used to model the gain (g) of these QWs in practice[23]:

$$g = mg_0 \ln(\frac{J}{mJ_{tr}}) \qquad g_0 = 1300\,\mathrm{cm}^{-1}, \text{and } J_{tr} = 110\mathrm{Acm}^{-2}$$

where J_{tr} is the current density at which the QW becomes transparent, and m is the number of such QWs.

2.4.5 Singlemode lasers

Since the semiconductor gain spectrum at nominal current levels is typically broad (>10nm), a large number of axial modes may simultaneously lase in an edge-emitting cavity. Figure 2.9 illustrates this phenomenon.

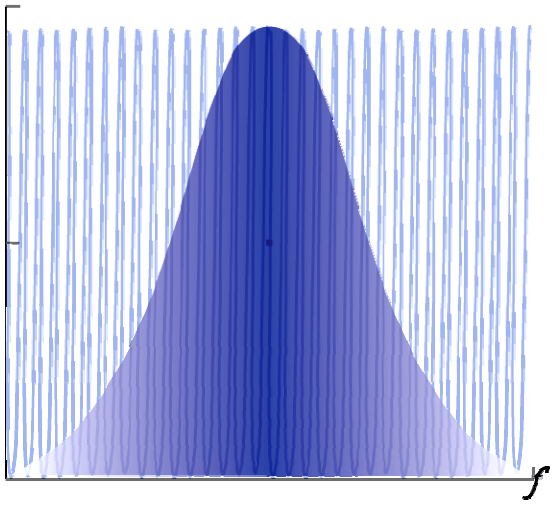

Figure 2.9: The transmission spectrum of the axial modes (fine) and the gain spectrum (broad) in a typical edge-emitting laser cavity.

The frequency spacing between these modes in an FP etalon cavity is constant:

$$\Delta f = \frac{c}{2nl}$$

where c is the speed of light in vacuum, while n and l are the index and length of the cavity. As an example, in a 400μm GaAs edge-emitting laser operating at 850nm, this spacing corresponds to only 0.25nm. It is therefore quite difficult to achieve single-frequency lasing in simple cleaved-facet, edge-emitting lasers.

Obviously, the FP cavity length should be drastically reduced in order to make a singlemode laser. Alternatively, a very fine filter can be added to the cavity to introduce selective loss to the other axial modes, so that only one mode experiences enough gain for lasing.

2.4.5.1 Single-frequency edge-emitting lasers

Such filters are typically realized by distributed Bragg gratings. These reflectors can replace one or both semiconductor mirrors and provide a narrow reflection band that effectively filters spurious modes. This is shown in Figure 2.10.

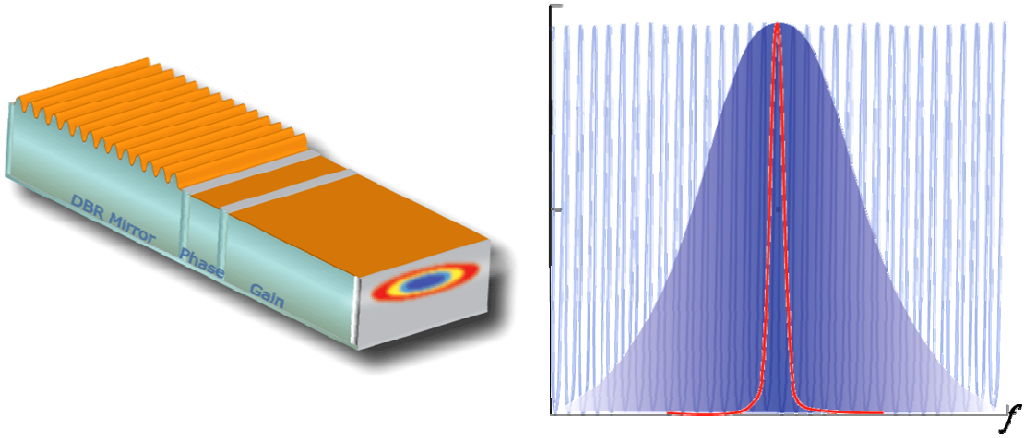

Figure 2.10: A DBR laser and the equivalent filter spectrum.

A periodic pattern (pitch~λ/2), typically formed by e-beam lithography and etching of the grown wafers, provides a highly wavelength-selective reflector for these lasers. Distributed feedback (DFB) lasers use only one grating that covers the pumped region of the device, while distributed Bragg reflector (DBR) lasers can have a more complicated design with separate mirrors and active regions. The laser cavity is typically divided into several such regions to provide extra control over mirror phases and add tunability, or to further amplify the output signal.

2.4.5.2 Vertical cavity surface emitting lasers (VCSELs)

Alternatively the cavity length can be reduced so that the gain spectrum overlaps with just one mode. Since the roundtrip gain in such a laser is very small, the mirror reflectivity and internal loss of these systems must be extremely low. The mirrors are therefore realized by highly reflective, epitxially-grown distributed Bragg reflectors (*e.g.* multiple AlAs/GaAs pairs) in vertical cavity surface emitting lasers (VCSEL). This is illustrated in Figure 2.11.

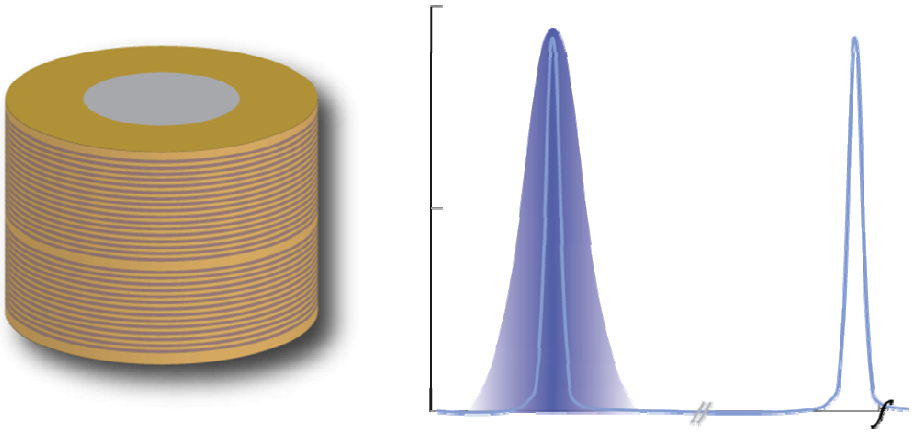

Figure 2.11: A VCSEL and its gain/axial-mode spectra.

VCSELs hold several advantages over edge-emitting lasers. To begin with, the output beam of VCSELs is circular and perpendicular to the surface of the wafer, thus fiber coupling and packaging of these devices are much simpler and cheaper than edge-emitting equivalents. Moreover, the small cavity length and pump area of VCSELs lead to single-frequency lasing, thermal stability, and high modulation speeds. Testing and fabrication of a VCSEL array is also much simpler than arrays of edge-emitting lasers.

2.4.6 Output beam profile

Since the index and gain profiles are largely different in the horizontal and vertical directions of an edge emitting laser, the output beam profile is highly elliptical and diverges at different angles, as shown in Figure 2.12.

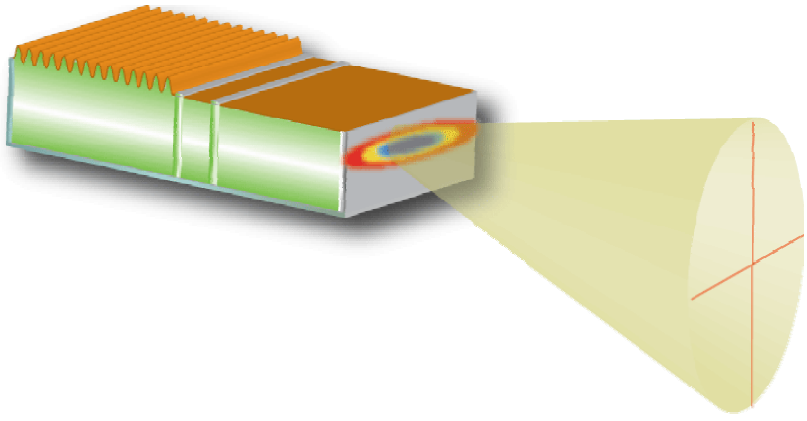

Figure 2.12: Typical mode profile in an edge-emitting laser.

This is particularly troublesome if this beam needs to be coupled to a small-core fiber. Special aspheric lenses are typically used to correct this and provide a circular beam at the fiber input (as shown in Figure 1.3 before).

2.4.7 High power lasers

It is also important to study the high-power failure methods of diode lasers as these devices are increasingly used to pump high-power solid state or fiber lasers. While failure due to heating is the main limiting mechanism for laboratory lasers, it is possible to mitigate this effect and accommodate higher current levels by improving the laser efficiency and proper heat sinking.

Another more troublesome failure method is the catastrophic optical damage (COD) of laser mirrors at high output powers. It is caused by the absorption of laser energy at the semiconductor facets, which leads to heating, mirror damage, and consequently more absorption. The resulting feedback process eventually leads to destruction of the lasing surfaces.

2.5 Simulation toolbox

We developed several Matlab codes to simulate different aspects of these systems and provide numerical models to test our designs. Here we briefly review some of the underlying techniques for these simulations.

2.5.1 Transfer matrix method

The transfer matrix method is a powerful 1D simulation algorithm that is extensively used to model reflectivity of multilayer thin-film optical structures. Amazingly, this simple approach can also be applied to complicated optical waveguide structures, *e.g.* ARROWs, to find the modal profiles and propagation indices[24] with reasonable accuracies. For a stack of materials shown in Figure 2.13, this method provides an analytical relationship between the incident and reflected components of the electric field at the initial and final layers.

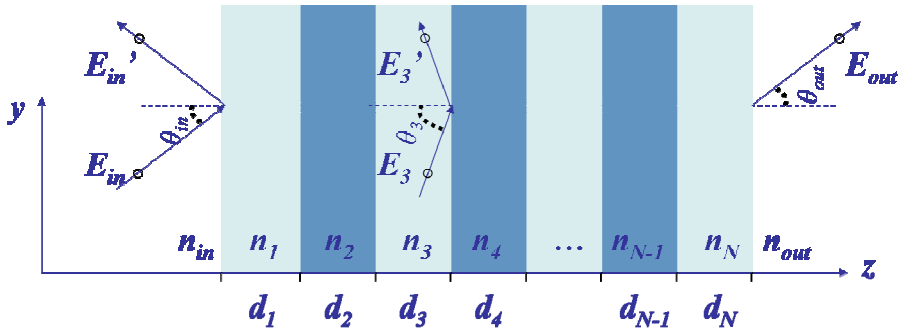

Figure 2.13: A multi-layer thin film stack and the corresponding incident and reflected electric fields in those layers for TE wave.

In this approach, every layer is modeled by a 2x2 transfer matrix that relates the two components of electric field on either side of that layer[25]:

$$\begin{pmatrix} E_{i-1} \\ E'_{i-1} \end{pmatrix} = M_i \begin{pmatrix} E_i \\ E'_i \end{pmatrix}$$

Consequently, the transfer matrix relating the first and last layers becomes:

$$\begin{pmatrix} E_{in} \\ E'_{in} \end{pmatrix} = M_1 M_2 \cdots M_N \begin{pmatrix} E_N \\ E'_N \end{pmatrix} = \begin{pmatrix} m_{11} & m_{12} \\ m_{21} & m_{22} \end{pmatrix} \begin{pmatrix} E_N^+ \\ E_N^- \end{pmatrix}$$

The only remaining task is to find this matrix for an arbitrary layer in general. It is possible to show that:

$$M_i = \frac{1}{t_i} \begin{pmatrix} \exp(j\phi_i) & r_i \exp(-j\phi_i) \\ r_i \exp(j\phi_i) & \exp(-j\phi_i) \end{pmatrix}$$

where $\phi_i = k_i \cos\theta_i d_i$ is the accumulated optical phase shift and r_i, t_i stand for the Fresnel reflection or transmission coefficients (for TE or TM polarizations) at the left interface to each layer. The transmission through this structure becomes:

$$t = \frac{E_{out}}{E_{in}} = \frac{t_{out}}{m_{11} + m_{12} r_{out}}$$

Since the waveguide modes are the characteristic resonance states of this system, they can be easily identified in a transmission graph (as a function of θ). It is important to note that the input and output layers should have high indices to allow coupling into the waveguide in the simulations. The mode index is simply: $n = \beta / k_0 = n_i \sin\theta_i$.

This method also yields the value of the electric field at each interface, thus a good approximation of the standing-wave profile can be found. Moreover, each layer can be divided into several same-index layers to improve the resolution of this calculation.

Apart from the core simulation code, a user interface was also designed for this program, which is depicted in Figure 2.14. Additional features, such as for simulating the reflectivity vs. time during an etch process or MBE growth were also added to this system to expand its usability.

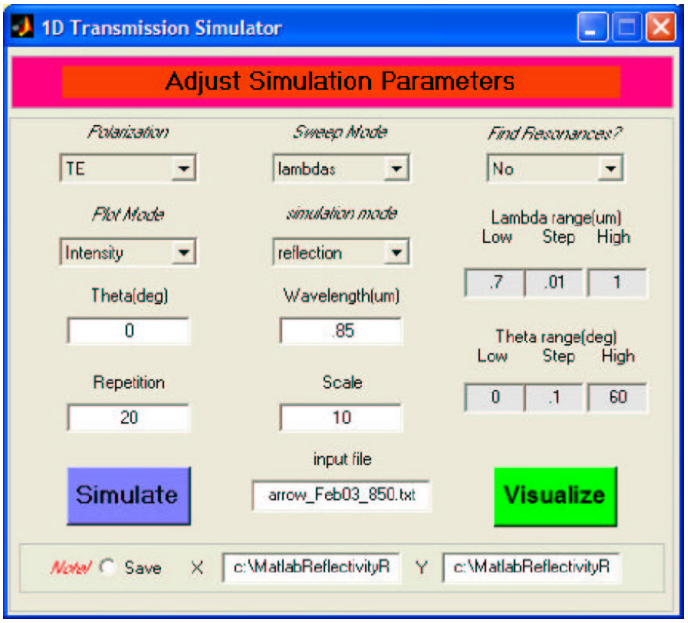

Figure 2.14: The user interface of the transfer-matrix/resonant-tunneling simulator (TRC).

It is also worthwhile to note that the same simulation algorithm can be applied to multiple quantum well structures as the Schrödinger equation in such systems is quite similar to the wave equation in the foregoing analysis. The exact form of the matrices and other details of this formulation can be found elsewhere[26].

2.5.2 Finite difference method

While simple methods like the foregoing transfer-matrix formulation or the effective-index method can be used to model waveguides, exact analysis of the modal profile requires a more accurate solution to the 2D wave equation in these structures. Here, we used a semi-vectorial finite-difference method[27] to find a reasonable

approximation to the waveguide modes. Since the ARROW modes have finite loss and very low indices, the original code[28] (or other commercial tools for that matter) is not suitable for simulating these structures. Therefore, a custom search algorithm was developed and added to this program to find the modes that have an eigenvalue in the vicinity of the fiber's index. This algorithm also filters out the solutions that do not decay exponentially out of the waveguide core.

Chapter 3

Evanescent coupling between fibers and semiconductors

Over the past two decades, different substrates have found applications in various photonic devices[2-5]. While semiconductor substrates, especially GaAs, are advantageous for integrated electrooptic devices and electronic circuits, most low loss waveguides have been fabricated on glass or lithium niobate substrates. Nevertheless, there has been a widespread research effort to expand the integration level on GaAs and InP based systems, and recently some highly-integrated PICs have been reported in the literature[1]. Glass waveguides on semiconductors have also been studied elsewhere[29]. But due to a large index contrast between glass and semiconductors, evanescent coupling between such waveguides is not feasible.

In this chapter, we introduce semiconductor antiresonant reflecting optical waveguides that enable evanescent coupling to glass waveguides and silica fibers. We discuss the properties of such hybrid systems and elaborate on their unique attributes that can be advantageous for many optoelectronic applications.

3.1 Material system

The material system used in this work is AlGaAs/GaAs, where lattice-matched $Al_xGa_{1-x}As$ layers are grown on a GaAs substrate by either molecular beam epitaxy (MBE) or metal-organic vapor phase epitaxy (MOVPE). The operating wavelength for the structures based on this material system is usually around 0.7-0.9μm, corresponding to the range of bandgap energies in these semiconductors. It is important to note that the $Al_xGa_{1-x}As$ bandgap[30] increases with the aluminum content,

while its index of refraction (at 850nm) decreases from roughly 3.4 in GaAs to 3 in AlAs[31]. This provides enough index contrast for high quality distributed Bragg reflector (DBR) mirrors in this technology. The semiconductor becomes indirect at about x~0.45.

Although this particular material system is described herein, it should not be construed in a limiting manner. Other systems, like InGaAsP/InP or InGaAsN/GaAs[32], can be used with minor design modifications to cover longer wavelengths.

3.2 Antiresonant reflecting optical waveguides

As studied before, in conventional waveguides the total internal reflection (TIR) is the main mechanism for confining electromagnetic energy in the waveguide core. Alternatively, high reflection mirrors can be employed to accomplish the same task. This technique is most appreciated in the context of microwave systems where metallic waveguides are widely used. Although metal films are highly absorbing at optical wavelengths, distributed Bragg reflectors (DBR) have little loss and make excellent mirrors for these applications. Special photonic bandgap structures, like antiresonant reflecting optical waveguides, use these DBRs to provide a medium for propagation of electromagnetic waves where conventional waveguides are not practical. Figure 3.1 compares the guiding mechanisms in conventional waveguides and ARROWs.

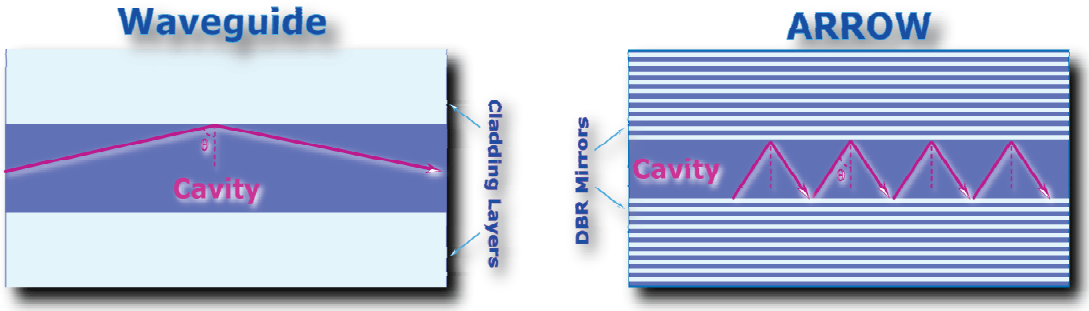

Figure 3.1: Ray traces in a conventional waveguide and an anti-resonant reflecting optical waveguide.

ARROWs can be regarded as a generalized form of vertical-cavity devices where the impinging rays can make arbitrary angles with respect to the DBR mirrors.

For a TE electromagnetic wave bouncing between two ideal mirrors at an angle θ, the modal solution should have zero tangential electric field at mirror boundaries and the rays should interfere constructively after two bounces. The wavefunction, therefore, has a sine-shaped envelope and the mode equation simplifies to:

$$2nd\cos\theta = m\lambda \qquad m = 1,2,..$$

where n and d are the refractive index and the thickness of the ARROW core, while m is the mode number that can be set to any integer value. While the top and bottom DBRs confine the ARROW mode vertically, the lateral confinement in a ridge ARROW structure, as shown in Figure 3.2, has to come primarily from the TIR at the ridge-air interface. This is in contrast with the passive devices presented in the previous work[11-13], in which no lateral confinement mechanisms were implemented.

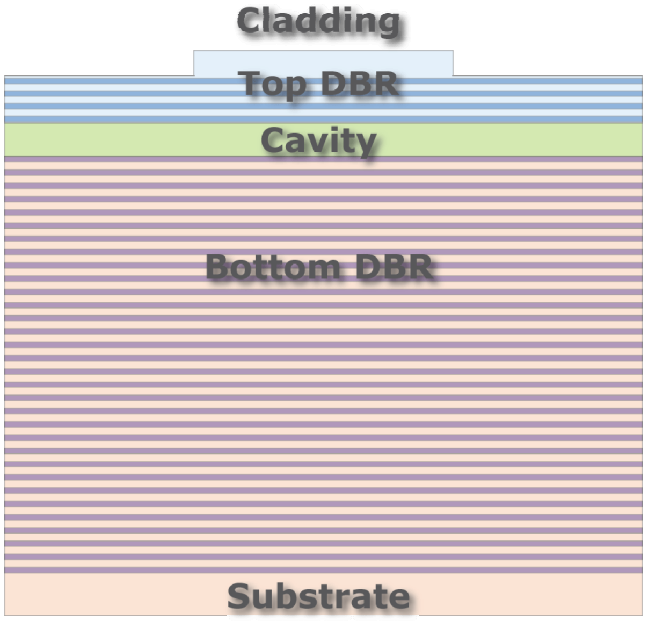

Figure 3.2: An illustration of a ridge ARROW structure.

Moreover, the top mirror is typically comprised of few DBR pairs, and a great portion of its reflectivity comes from the TIR at the top interface. We must therefore take the extra Goos-Hanchen phase shift (φ_{GH}) at the top interface into account when calculating phase relationships. The resonance condition for an ARROW with an ideal bottom mirror and no top DBRs becomes:

$$2\pi nd\cos\theta/\lambda + \varphi_{GH} = 2\pi m \qquad \varphi_{GH} = 2\tan^{-1}\left(\frac{\sqrt{n^2\sin^2\theta - n_0^2}}{n\cos\theta}\right)$$

where n, and n_0 stand for the index of the semiconductor and the cladding layer (either fiber or air), respectively.

3.2.1 Phase velocity

At small propagation angles, the effective phase velocity of the ARROW mode increases. By choosing an appropriate angle, around 25º in this case, we can design these waveguides to resonate evanescently with a singlemode fiber at a given wavelength. The effective phase index (n_{phase}) of such a mode for a semiconductor with index ~3.4 is:

$$n_{phase} = n\sin\theta \qquad n_{phase}\big|_{\theta=25^\circ} \approx 1.45$$

The large phase velocity of ARROWs may seem counter-intuitive at first. For one, it is almost twice as high as the speed of light in the semiconductor and it is in contrast with the ray picture of Figure 3.1, where shallow bouncing angles indicate a small propagation velocity. The answer to this paradox lies in the definition of the phase velocity. Since this parameter captures the rate at which the constant phase planes (as opposed to any physical information) travel in the space, it can practically exceed the velocity of light in the medium (c/n) without breaking any laws of physics. A packet of data, on the other hand, propagates in a waveguide at a speed that should always be equal or smaller than c/n.

3.2.2 Group velocity and dispersion

Group velocity is the speed at which a physical signal travels in a waveguide and therefore cannot exceed the speed of light in the medium. Theoretically, it is defined as $\partial\omega/\partial k$, rather than ω/k which identifies the phase velocity of the signal. A detailed discussion of the phase and group velocities can be found elsewhere[33]. While these velocities are quiet similar in conventional waveguides, they can be vastly different in ARROWs and other photonic bandgap structures. In fact, it is possible to prove that the product of phase and group velocities in an ARROW is constant. This is

again reminiscent of microwave waveguides, where the geometrical average of these velocities equals the speed of light in the medium. In a simple ARROW, it is easy to show that:

$$n_{group} = \frac{n}{\sin\theta} \qquad n_{group}\Big|_{\theta=25^\circ} \approx 8.1$$

Such a small group velocity has important implications. First off, the difference between phase and group velocities results in a large dispersion coefficient that effectively reduces the coupling bandwidth of the system. Below, we will calculate the dispersion for the ARROW waveguide of Figure 3.1. The general ARROW mode equation is:

$$2\pi.2n_{core}d\cos\theta/\lambda + \varphi_{DBR} = 2m\pi$$

In these calculations, n_{core} and d are the refractive index and the thickness of the ARROW core, while m is the mode-number and can be set to any integer value. λ_0, and λ are the original and the deviated wavelengths, respectively. φ_{DBR} stands for the phase shift accumulated from reflections off the top and bottom mirrors (φ_{DBR}= $\varphi_{bottomDBR} + \varphi_{topDBR}$). We therefore have:

$$-2\pi.2n_{core}d\sin\theta\,\partial\theta/\partial\lambda + \varphi_{DBR} + \left(\partial\varphi_{DBR}/\partial\lambda + \partial\varphi_{DBR}/\partial\theta\,\partial\theta/\partial\lambda\right)\lambda = 2m\pi$$

Since the DBR mirrors are designed at a center wavelength and angle of λ_0=850nm and θ_0=25º here, the original reflection phases are zero, but these can deviate significantly if the incidence angle or the wavelength of the optical beam changes. These phase slopes are calculated by a 1D reflectivity simulator:

$$\frac{\delta\varphi_{topDBR}}{\delta\lambda} \approx \frac{-85^\circ}{60^{nm}} \,\&\, \frac{\delta\varphi_{bottomDBR}}{\delta\lambda} \approx -\frac{115^\circ}{60^{nm}}$$

$$\frac{\delta\varphi_{topDBR}}{\delta\theta} \approx \frac{-90^\circ}{10^\circ} \approx -9 \,\&\, \frac{\delta\varphi_{bottomDBR}}{\delta\theta} \approx -\frac{70^\circ}{6^\circ} \approx -12$$

Plugging these numbers in the derivative of the phase-index equation (n_{phase}=$n\sin\theta$) yields:

$$\frac{\partial n_{eff}}{\partial\lambda} = \frac{3.14141}{\lambda_0(.4632m + 3.342)}(-m - 7.87)$$

Depending on the DBR mirrors, the index dispersion coefficient in our ARROWs can change from -5μm^{-1} to -10μm^{-1}. Such large dispersion coefficients entail a small coupling linewidth (less than 1nm), since the bandwidth in a coupled ARROW-fiber system is inversely proportional to this dispersion coefficient.

$$\Delta\lambda = \frac{\Delta\beta}{k_0(\partial n_{eff}/\partial\lambda)}$$

where $\Delta\beta$ is determined from the coupling equations. It is also noteworthy to study the dependence of this dispersion factor on important design parameters, like the cavity order and the number of the top DBR pairs. As mentioned earlier, the top ARROW mirror can be realized as a combination of both TIR and DBR mirrors and can therefore change the dispersion properties. While the DBR mirrors are generally more wavelength (and angle) sensitive, the GH shift at the TIR interface can also bring about such phase-shifts. Our simulations indicate that such variations can adjust the dispersion by a factor of two at most. While a thicker top DBR increases the dispersion, it also reduces the intensity of the evanescent field in the cladding layer and lessens the coupling strength of the system.

On the other hand, the dispersion coefficient is very insensitive with respect to changes in the cavity order. Figure 3.3 shows that such dependence is indeed very weak.

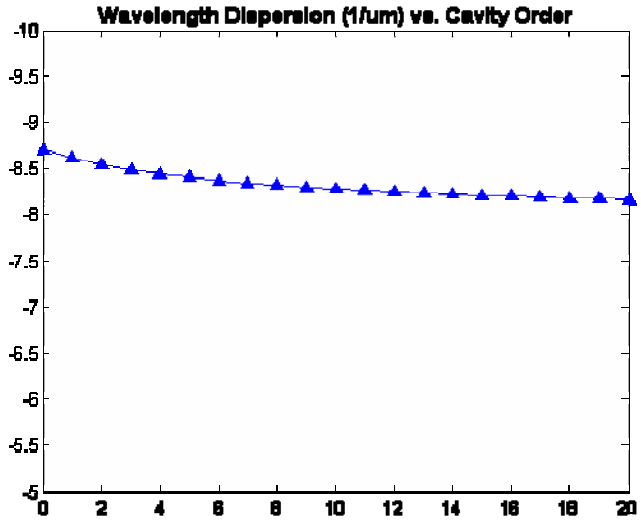

Figure 3.3: Wavelength dispersion factor vs. cavity order in the ARROW structure of Figure 3.2.

3.2.3 Loss (gain) enhancement in ARROWs

Another important implication of the small group velocity is an increase in the loss (gain) of the ARROW modes due to an amplified interaction with the propagation media. This enhancement factor, which is in addition to the standing wave gain-boosting of the VCSEL-like structures, can be calculated in many different ways. The ray picture is the simplest way to explain this phenomenon. Since the time taken by the mode to travel a certain distance is amplified by $\zeta=1/\sin\theta$, the effective loss (gain) also gets augmented by the same factor. Alternatively, a thorough EM analysis of the overall modal loss (gain) in such media can yield the same enhancement factor[21]. At $\theta\sim25^{\circ}$, this enhancement factor is roughly equal to 2.36. This is extremely desirable as it effectively doubles the material gain in our systems.

3.2.4 Loss

There are various sources of loss in ARROWs that can severely compromise the performance of systems employing such waveguides. In this section, we try to study and quantify some of these sources in the hope of improving the design methodology of these devices.

3.2.4.1 Mirror loss

Mirror quality is extremely critical in ARROWs, as it determines primarily the ARROW confinement quality and the leakage. The modal loss can be calculated by the Pointing-vector analysis of the mirror leakage, or through simulations of the optical mode in an electromagnetic field solver. Although Pointing-vector analysis can be somewhat inaccurate, it can nevertheless identify the trends and provide an invaluable design tool in such systems. In the following calculations, we try to evaluate the modal loss from the ray picture of Figure 3.1. We first notice that the beam gets reflected by the bottom mirror every $z_R = 2d\tan\theta$, where d is the thickness of the cavity. Every time the beam gets reflected, a portion of the power gets lost due to the mirror leakage. This portion is equal to: $P_{lost} = P_0 T$, where P_0 is the incident power and T is the transmission through this mirror. Therefore:

$$P(z) = P_0 e^{-\alpha_{mirror} z} \;\Rightarrow\; \alpha_{mirror} = \frac{T}{2d \tan\theta} \qquad (T << 1),$$

where α_{mirror} captures the contribution of this DBR to the ARROW modal loss. Figure 3.4 shows that for loss levels of less than 1cm^{-1}, at least 30 DBR pairs are required. $Al_{0.20}Ga_{0.80}As/Al_{0.93}Ga_{0.07}As$ mirrors were used for this analysis. For this calculation, we assumed $d=1\mu m$ and $\theta=25^o$.

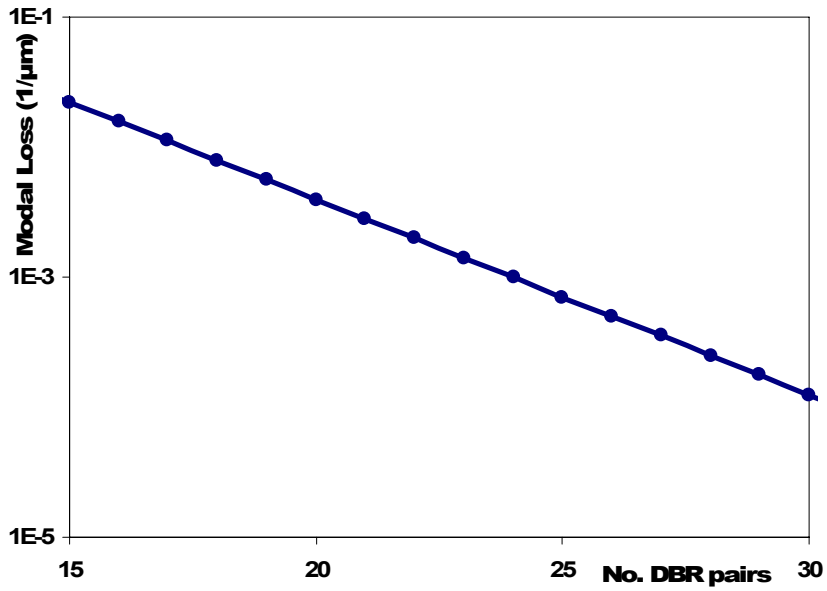

Figure 3.4: ARROW modal loss due to the mirror leakage for different number of bottom DBR pairs.

3.2.4.2 Material and doping loss

While the mirror loss can be significantly reduced by increasing the number of DBR pairs, material losses cannot be overcome as easily. In fact, most of the loss in these waveguides results from free-carrier absorption by the dopant atoms. This is more troublesome in p-type material as holes absorb more photons and have lower electrical mobilities. Free carrier absorption coefficients at 850nm for holes and electrons are 11cm^{-1}, and 5cm^{-1} respectively[34,35]. These values tend to go up significantly at longer wavelengths and the material loss becomes an increasingly bigger issue in design of telecommunications lasers.

3.2.4.3 Scattering loss

Another source of loss in ARROWs arises from scattering at the ridge sidewalls and oxide aperture fronts. Since this loss is proportional to the local field intensity, it is essential to reduce the electric field amplitude at the scattering centers. In particular, it is critical to keep these centers away from the standing wave antinodes. The sidewall quality can improve by avoiding high Al content alloys in the ridge area. A better etching process can improve the sidewall roughness and reduce the scattering loss. To minimize the interaction of the mode with the oxide aperture, a tapered oxide front can be implemented[36]. This way, the tip of the oxide sits at the node of the standing wave and the mode experiences little scattering.

3.2.5 Simulation of ARROW modes

Figure 3.5 depicts the two-dimensional electric field intensity profile of the fundamental mode in a ridge ARROW, with AlGaAs top and bottom DBR mirrors surrounding a 3rd order cavity in the center.

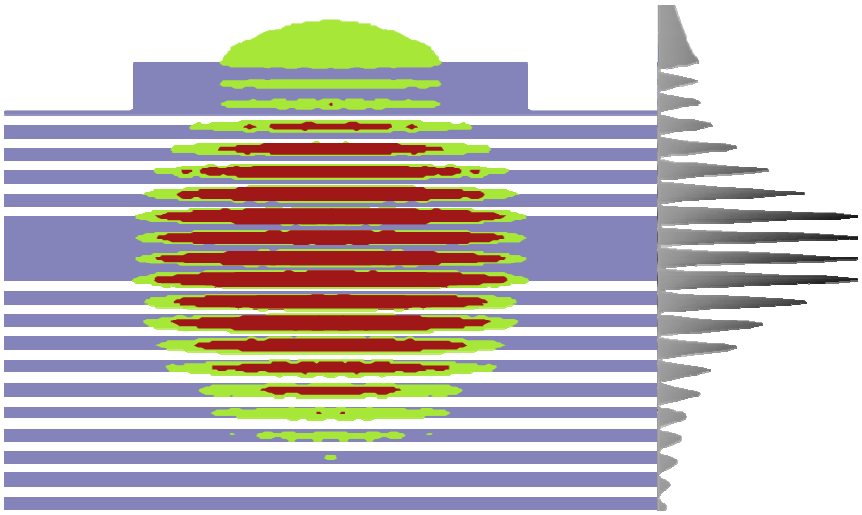

Figure 3.5: 2D profile of the fundamental mode of an ARROW. Vertical intensity distribution is also shown in this figure.

This graph clearly shows the VCSEL-like envelope in the vertical direction, as well as the lateral confinement from total internal reflections at the ridge sidewalls. This mode has an effective propagation index of 1.45, which almost exactly matches the modal index of the 5/125µm singlemode fiber in our test setup. The lateral mode-

width is designed to match the width of the fiber mode for stronger coupling efficiency.

3.3 Side-polished fibers

To facilitate coupling into a fiber to provide access to its evanescent field, most of the cladding layer has to be removed, at least on one side of the fiber. This is typically done by housing the fiber in another substrate and polishing the combined surface until the cladding material is mostly gone. An index matching liquid is used at this point to monitor the fiber transmission through the remainder of the polish process. Since evanescent power leakage is a strong function of the polish depth[37], this method can be used to determine the remaining thickness of the cladding layer. While a deeper polish eases access to the evanescent field of the fiber, it can also perturb the shape of the mode. For this reason, the polish typically stops short of the fiber core.

Since the polished area sits at the heart of our hybrid devices, its surface quality is extremely important. A rough surface can introduce significant scattering loss to the composite mode and severely limit the performance of the system. Moreover, this loss is not easily modeled in our first-order equations as it can be significantly different for the symmetric and antisymmetric modes of the coupled system. While the electric field distribution of the antisymmetric mode is typically minimal at the coupling interface, the symmetric mode component can be significantly large. Consequently, it is critical for the fiber to have a clean, finely polished surface on the fiber for side-coupling applications. Index-matching fluids can also leave residues on the fiber which are difficult to remove, and therefore should be used very sparingly.

The fiber used here is singlemode at wavelengths larger than 780nm, with a typical mode field diameter ~4.5μm, a numerical aperture ~0.13, and an allowed bend radius of larger than 2cm. This fiber is housed in a rather bulky glass substrate (2mm wide, and 1.5mm thick), which makes electrical probing of the evanescently-coupled waveguides very difficult. Alternatively, side-polished fibers housed in silicon V-grooves[38] can be used to realize fiber half-couplers. This approach has numerous

advantages compared to the glass couplers used in this work (from Canadian Instrumentation and Research Ltd.); as array configurability, substrate bonding, and other well-developed processes are readily available in silicon technology.

3.3.1 Fiber half-coupler models

While exact 2D simulation of the side-coupled fiber-ARROW system is very tedious, it is possible to find an easier planarization technique that greatly simplifies the analysis of these systems. Such planar structures can be plugged easily into the transfer-matrix calculations to estimate the mode profiles and corresponding index values. Since fiber half-couplers are used extensively in directional couplers, there are numerous studies of these devices in the literature. In particular, one group[39] presented a planarization method that closely preserves the mode indices, as well as the lateral mode profile compared to the 2D structure. This method is described in Figure 3.6.

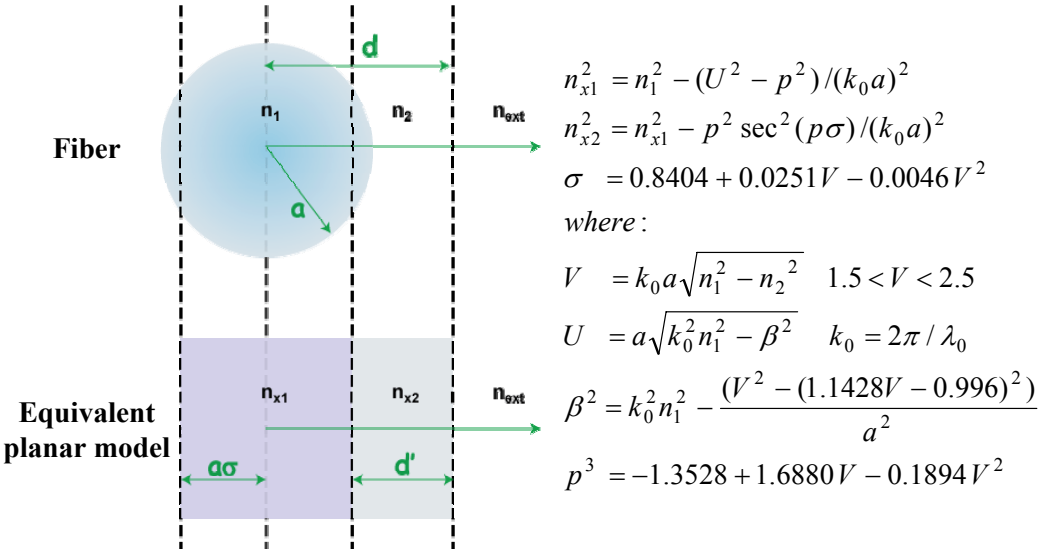

Figure 3.6: Sharma model and the corresponding equations.

where n_1, n_2, n_{ext} are the indices of fiber core, cladding and the external material (*e.g.* ARROW), whereas n_{x1}, n_{x2} are the indices of equivalent slab structure of Figure 3.6. a and d stand for the fiber radius and the fiber-ARROW separation, while σa stands for the thickness of the equivalent slab waveguide. β is the propagation index of the fiber mode, and V is its normalized frequency, which were previously discussed.

3.4 Coupling between ARROWs and fibers

An illustration of the ARROW-fiber coupled system is shown in Figure 3.7. As in conventional twin waveguide structures, this system possesses both symmetric and an antisymmetric modes (eigenmode) that result from the superposition of the respective fiber and ARROW modes under phase matching conditions. Similarly, the difference between the effective indices of these modes primarily determines the coupling coefficient of this system.

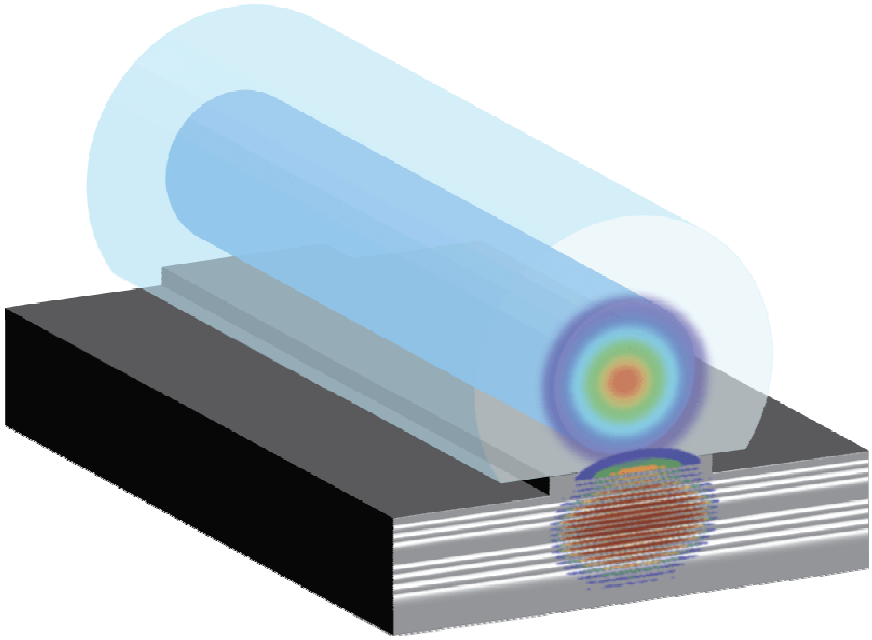

Figure 3.7: Interacting fiber and ARROW modes in a side-coupled structure.

In this section we analyze different aspects of this hybrid ARROW-fiber system and provide various experimental results to validate the theoretical analysis.

3.4.1 Coupled-mode equations

We can use the first-order coupled-mode equations of the previous chapter to analyze the coupling behavior of an ARROW-fiber system. However, a second term should be added to the ARROW equation in order to account for the losses in that waveguide:

$$\partial_z F = -j\kappa A e^{jz\Delta\beta}$$
$$\partial_z A = -j\kappa F e^{-jz\Delta\beta} - A/l_{loss}$$

where A and F are the amplitudes of the electric field in the ARROW and the fiber, respectively. l_{loss} is the loss length of the ARROW waveguide for the electric field amplitude (not intensity). Obviously this length will be negative if the waveguide has gain. Although these equation can be solved analytically[40], in this section we present some numerical analysis to gain insight into the effects of coupling, wavelength, and loss parameters on the performance of this system.

3.4.1.1 Behavior under phase matching

Under the phase matching condition, ($\Delta\beta=0$), and the equations simplify to:

$$\partial_z F = -j\kappa A$$
$$\partial_z A = -j\kappa F - A/l_{loss}$$

It is easy to show that these equations have an exponential e^{-sz} solution. Therefore:

$$s^2 + s/l_{loss} + \kappa^2 = 0 \Rightarrow s = \frac{-1 \pm \sqrt{1 - 4\kappa^2 l_{loss}^2}}{2}$$

This equation implies that the coupled system has two distinct regions of operation, depending on the loss of the ARROW waveguide. If $|2\kappa l_{loss}|>1$ the solution is primarily oscillatory with an exponential envelope, while such oscillations fade completely when $|2\kappa l_{loss}|<1$.

Figure 3.8 illustrates how the electric field amplitude in the fiber changes as a function of the length of the coupled region and loss of these waveguides under phase-matching conditions. Although the introduction of loss in these systems does not completely wipe out the coupling phenomenon, it can significantly reduce or increase the coupled power over different interaction lengths. Power is initially coupled to the fiber in the following simulations. The coupling distance, $l_{coupling}$, for this calculation is set to 100μm ($l_{coupling}= \pi/2\kappa$). The location of the first zero of the fiber (complete power transfer out of fiber) is extremely important. At this point, a slight change in loss can significantly modulate the signal in the fiber, while at other lengths the

change may not be considerable. There is therefore an optimal length for the coupled region, if efficient modulation is desired.

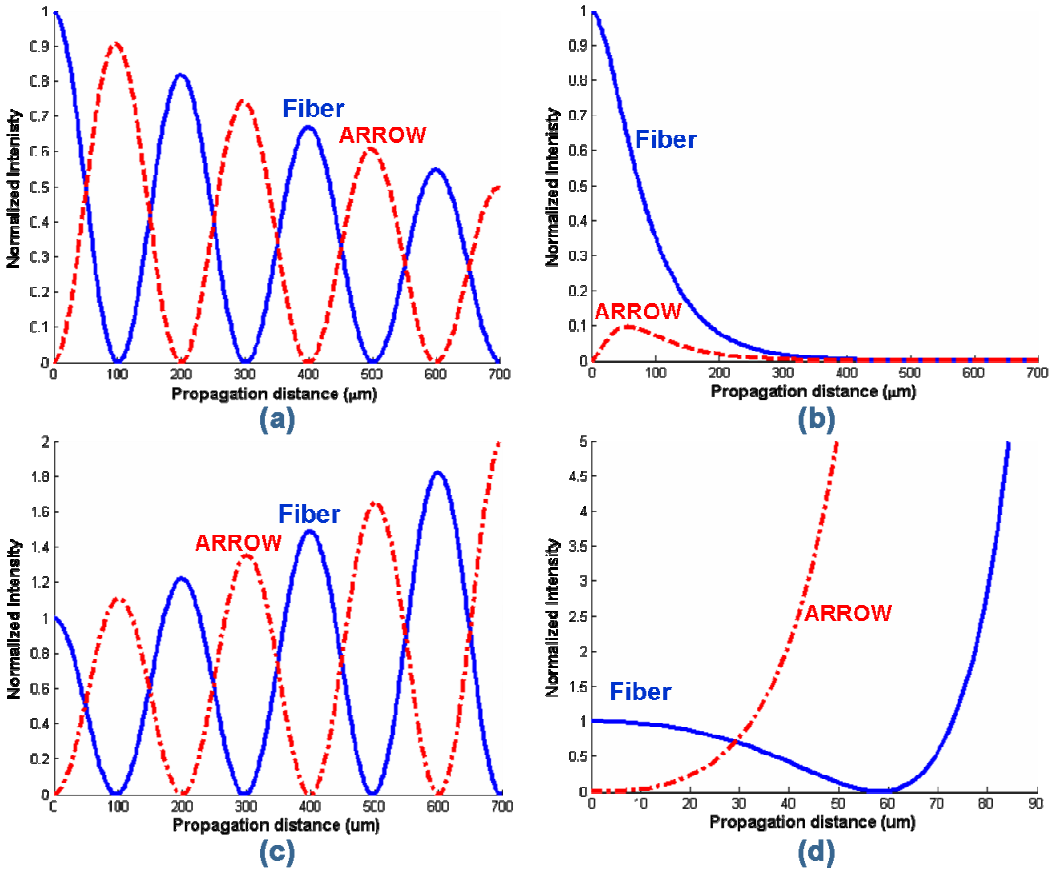

Figure 3.8: Simulated power coupling curves between fiber and ARROW for different loss/gain levels: (a) $2\kappa l_{loss}=30$, (b) $2\kappa l_{loss}=0.8$, (c) $2\kappa l_{loss}=-30$, (d) $2\kappa l_{loss}=-0.8$

In the under-damped regime ($|2\kappa l_{loss}|>1$), it takes longer distances for lossier ARROWs to completely extract the electromagnetic energy out of fiber; whereas in the over-damped regime ($|2\kappa l_{loss}|<1$) complete power transfer or over-coupling will never take place. This is the case, for instance, if several unpumped QWs are placed in the waveguide. At finite gain, the fiber gets depleted of the electromagnetic energy over a shorter distance. While the oscillatory behavior vanishes at $l_{loss}>-1/2\kappa$, the signal initially decreases and couples out of fiber (like oscillatory systems) before it starts to strengthen exponentially. It is also clear that the fiber signal experiences amplification at sufficiently high gain levels in the waveguide. It is worthwhile to note

that in practice, the maximum length of the coupling region is limited to the extent of the polished area of the fiber.

3.4.1.2 Wavelength dependence of coupling

Since the fiber transmission spectrum is an important, easily measured attribute of these systems, we discuss the wavelength dependence in some detail. In general, the spectrum changes significantly as the loss/gain of the ARROW is tuned. In order to simulate the spectrum however, we need to determine the dispersion curves of ARROWs and fibers. The single core singlemode fiber has very small dispersion coefficients that can be safely ignored, whereas ARROW dispersion is much larger and should be properly accounted for in order to correctly model these systems.

The first set of graphs (Figure 3.9) show the fiber and ARROW spectra at different lengths of the coupled region for the lossless ARROW of Figure 3.5. Clearly, the bandwidth shrinks and the resolution improves as the coupling between the waveguides extends over a longer distance.

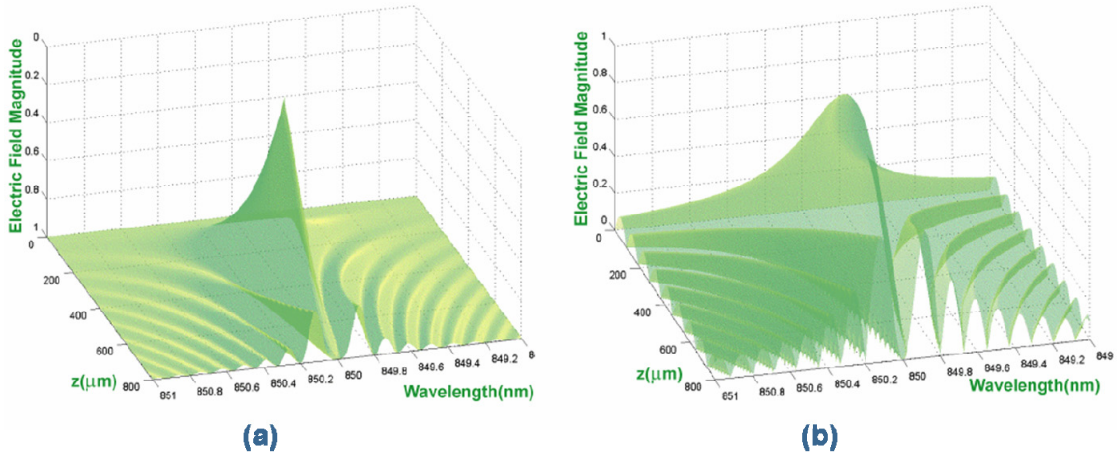

Figure 3.9: Lossless electric field amplitude spectra at different interaction lengths for (a)fiber and (b)ARROW. The coupling length is assumed to be 400μm.

The following figure gives more details on the effects of loss (gain) on the fiber transmission spectrum at different coupling lengths.

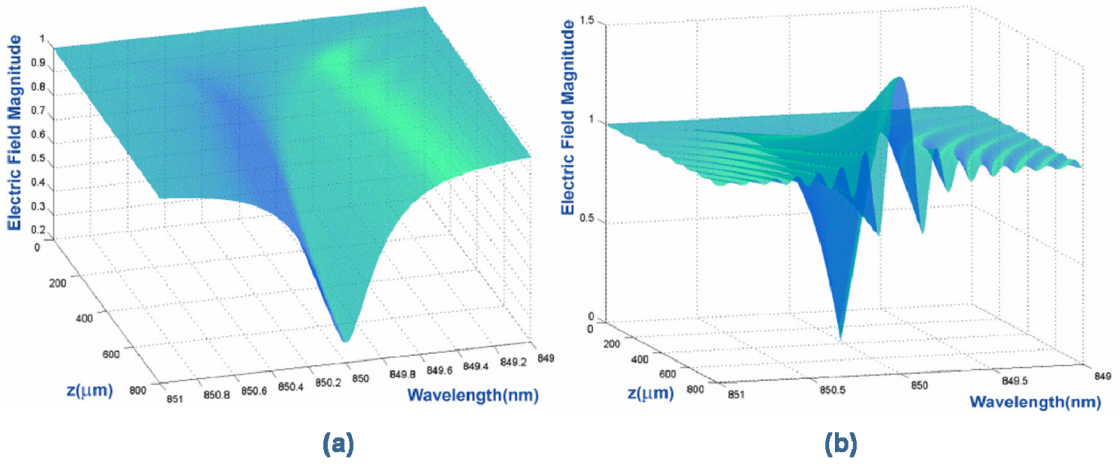

Figure 3.10: The electric field amplitude spectra of fiber at different interaction lengths for (a) $2\kappa l_{loss}=0.8$, and (b) $2\kappa l_{loss}=-8$. The coupling length is assumed to be 400μm.

It is clearly seen that spectral ripples are washed away and the spectrum broadens if the fiber is coupled to a lossy ARROW, while the opposite happens when gain is added to the system.

3.4.2 Coupling coefficient

The coupling coefficient primarily determines the behavior of a coupled mode system, so it is instrumental to analyze this parameter in an ARROW-fiber system. While exact calculation of this coefficient requires a detailed simulation of the odd and even modes of the system[41], we instead focus on deriving the dependencies of this coefficient on various system parameters. Since the coupling coefficient is proportional to the overlap integral of the modes, we have:

$$\kappa = \frac{\pi}{2l_{coupling}} \propto \frac{\int (\Delta n^2 E_{fiber} E_{ARROW}) dy}{\sqrt{(\int |E_{fiber}|^2 dy) \cdot (\int |E_{ARROW}|^2 dy)}}$$

where E_{fiber} and E_{ARROW} are the electric field distribution of fiber and ARROW respectively. The above overlap integral can be calculated either by taking the fiber core as the perturbing medium for the ARROW mode, or vice versa. (The resulting overlap integrals should be the same; otherwise energy will not be conserved in this system.) As shown in Figure 3.11, the ARROW integral is rather hard to compute because its mode has a fast oscillatory behavior inside the semiconductor. Instead we

calculate the easier overlap integral over the fiber core. It is also important to note that the spacing between the fiber core and the ARROW (cladding layer in the figure) can be filled by other materials (*e.g.* an air gap) instead of silica. We will discuss the effects of this layer on the coupling factor first. We assume that this cladding layer is included in the ARROW mode simulations, so that fiber core is the only perturbing medium in our analysis.

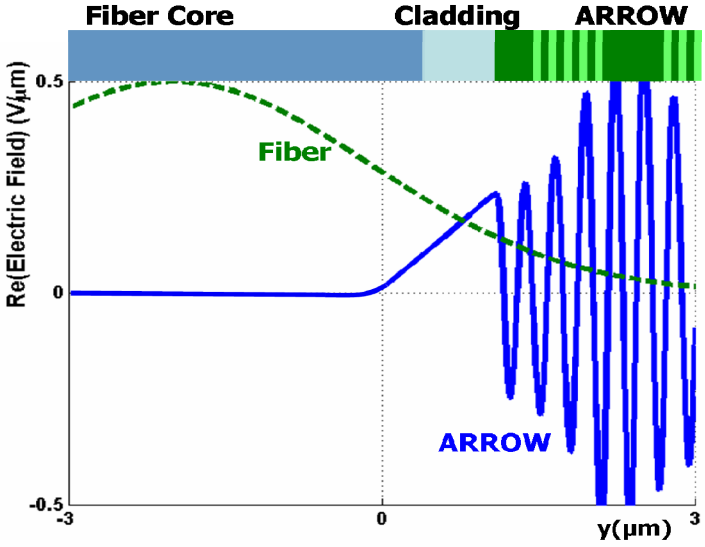

Figure 3.11: The interacting vertical electric fields of fiber and ARROW.

The coupling coefficient therefore becomes:

$$\kappa = \frac{\pi}{2l_{coupling}} \propto \frac{\int_{fiber\ core} (n_{core}^2 - n_{clad}^2) E_{fiber} E_{ARROW} dy}{\sqrt{(\int |E_{fiber}|^2 dy) \cdot (\int |E_{ARROW}|^2 dy)}}$$

The ARROW mode can be approximated by a decaying exponential outside of the semiconductor:

$$E_{ARROW} = E_{top}\, e^{\gamma (y - y_{top})}$$

where E_{top} and y_{top} are the electric field amplitude and the location of the top semiconductor surface in Figure 3.11. γ is the damping coefficient, which depends on the cladding index n_{clad} and the mode propagation parameter:

$$\gamma = \sqrt{n_{clad}^2 k_0^2 - \beta^2} = k_0 \sqrt{n_{clad}^2 - n_{eff}^2}$$

where n_{eff} is the effective index of the ARROW mode that is matched to the fiber's index. Moreover, the fiber mode is conveniently estimated by a Gaussian profile as discussed in the previous chapter. So, the resulting overlap integral becomes:

$$\kappa \propto \frac{\int_{fiber\,core} E_{0\,fiber} e^{\frac{-r^2}{w^2}} E_{top} e^{\gamma(y-y_{top})} dy}{\sqrt{(\int |E_{fiber}|^2 dy) \cdot (\int |E_{ARROW}|^2 dy)}}$$

It is now an easy task to estimate the change in the coupling coefficient as a function of various design parameters, like the intermediate material properties:

$$\kappa \propto E_{top} e^{-\gamma . l_{spacing}}$$

where $l_{spacing}$ is the thickness of the cladding layer in Figure 3.11. This formula implies that the coupling coefficient degrades exponentially as the spacing between the waveguide and fiber is increased. It is therefore critical to keep this spacing small. This formula also indicates a strong frequency dependence, as the characteristic distance is proportional to the wavelength:

$$l_{clad} = 1/\gamma = \lambda_0 / 2\pi \sqrt{n_{clad}^2 - n_{eff}^2}$$

At 850nm, without any gaps between the substrates (except the remaining fiber cladding), this characteristic distance is roughly ~1.3μm, while in the case of an air-gap this distance reduces to 130nm. Since this value is extremely small and difficult to control in practice, it is common to use an index-matching liquid to fill such gaps. Nonetheless, because these liquids leave residues and add loss, they were avoided in our experiments. Moreover, it is important to note that index-matching oils often have strong temperature (and wavelength) dependence; therefore the matching can be thermally unstable. The optimal solution to this problem lies in the implementation of a robust bonding technique that assures optical contact without requiring such liquids. Anodic or fusion bonding techniques, as well as various epoxies can be implemented in this context[42].

It is also instrumental to study the effect of the top DBR on the coupling coefficient. Obviously, the coupling factor is proportional to the electric field amplitude at the ARROW-fiber interface, which decreases exponentially as more top

DBR-pairs are employed. This reduction is however balanced with an increased modal confinement of the ARROW mode. The dependence is therefore not very strong for small numbers of top DBRs. In general, computer simulations are used to quantify this effect.

3.4.3 Transmission spectrum vs. the coupled length

As described previously, the coupling bandwidth can be very small. In reality, this bandwidth is a complex function of loss, coupling length, interaction region dimensions, and growth nonuniformities. Fiber transmission spectra for different coupling lengths of an ARROW-fiber system are shown in Figure 3.12. An 850nm laser is biased below threshold to provide a broadband source at the input of the fiber.

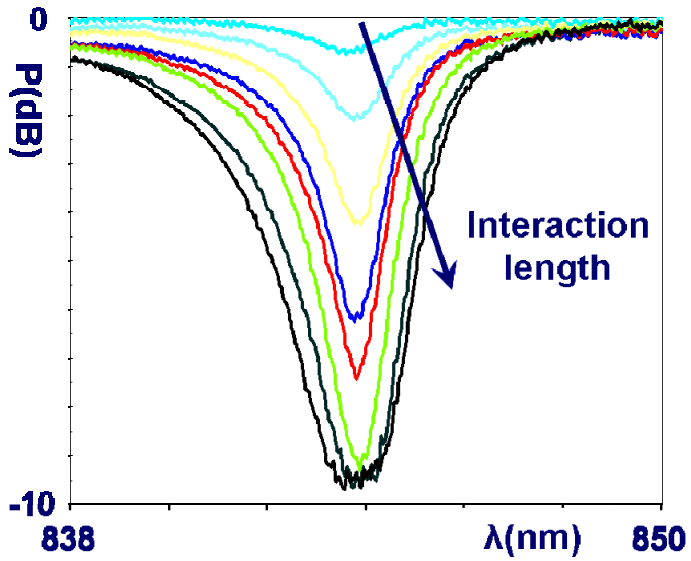

Figure 3.12: Change of fiber transmission spectrum as a function of the ARROW-fiber interaction length. Different curves correspond to $l_{coupled}$=0.1, 0.4, 0.5, 0.7, 0.9, 1.0, 1.2, 1.5mm. These measurements often accrue large errors due to alignment difficulties. Details of the ARROW structure in this experiment are discussed in section 6.4.

Due to the cavity and QW losses, passive ARROWs often operate in the monotonically-decaying regime and no overcoupling effect is observed. While the phase-matching valley gets deeper at larger distances, the bandwidth also increases, indicating that a large growth taper exists in these MOVPE-grown ARROWs.

In practice, it is very difficult to determine the coupling coefficient from these passive transmission spectra. For one, the coupling coefficient is sensitive to substrate

misalignments and large horizontal or vertical offsets (*i.e.* an air-gap) greatly reduce this parameter. Unfortunately, such offsets are unavoidable in the manual substrate alignment method we used for these proof-of-concept demonstrations. Moreover, thickness taper caused by growth nonuniformities can change the observed spectrum to a great extent. Finally, limited degree of polarization at the input source reduces the maximum measurable coupling depth to ~10dB.

Despite these conditions, it is still possible to find a lower limit for the coupling coefficient as all these phenomena tend to weaken the coupling and reduce/broaden the depth/width of the observed spectrum. For instance, if the measured spectral notch is 10dB deep, it is possible to show that $l_{coupling}$<500μm. In this calculation, we assumed a conservative QW loss estimate of 200cm^{-1}, and an interaction length of 1mm, which is determined by the polished extent of the fiber evanescent block.

3.4.4 Polarization dependence

Due to growth offsets, the DBR phase shifts accumulated by the TE and TM modes of an ARROW waveguide can be different. This is clearly visible in Figure 3.13, which depicts the TE and TM transmission spectra of the previous ARROW structure. The TM modes can also experience significant absorption by the surface plasmons of the metal contacts on the ARROWs[43].

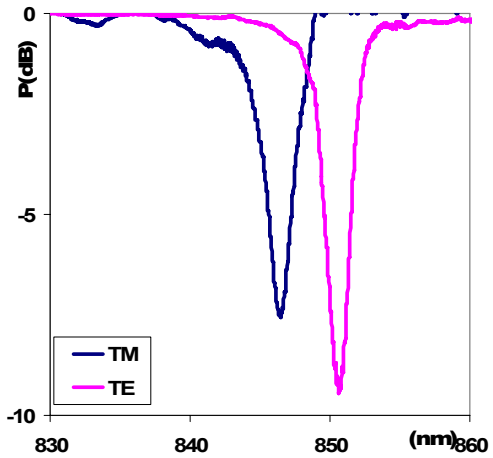

Figure 3.13: Effect of input field's polarization on the transmission spectra in a sample ARROW.

Unfortunately polarization can change significantly as the signal travels in symmetrical singlemode fibers. In order to control the signal polarization over the interaction region, a fiber polarization controller is inserted between the input laser and the coupling medium, unless the fiber is extremely short.

3.4.5 Temperature dependence

Since the ARROW-fiber coupling depends merely on the indices of the semiconductor and silica material, the temperature coefficient of the phase-matching wavelength is determined by the thermal change of such indices. For AlGaAs material, the index changes ~$2x10^{-4}$/ºC with temperature[44]. This translates into a small wavelength variation of ~0.06nm/ºC, which is an excellent number in most optoelectronic applications. This dependence is depicted in Figure 3.14. This temperature dependence is the same in all hybrid ARROW-fiber devices, including fiber lasers of chapter 6.

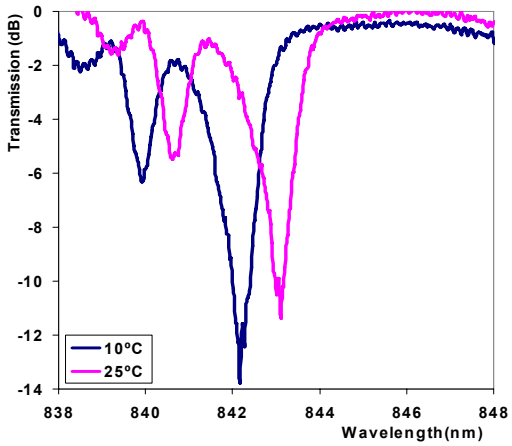

Figure 3.14: Sample fiber transmission spectra at different temperatures.

3.4.6 Previous work

Previously, a hybrid narrow-band detector[11], and a modulator[12] were demonstrated in this technology. Although these devices may be useful in some applications, the inherent wavelength selectivity and polarization sensitivity of these systems limit the applications of such devices in the real world. Moreover, previous

ARROW implementations were all one-dimensional and no lateral confinement mechanism was used, which contributed heavily to the loss of those waveguides.

3.5 Test setup

ARROW chips are mounted on a thermoelectric cooler (TEC) in an electrical probing station, using a conductive paste. The chip is brought into contact with the polished side of the fiber, which is glued to the translation arm of an x-y-z stage. The critical waveguide-fiber alignment procedure is monitored through an IR CCD camera placed on top of the probe station. Both fiber and ARROWs are clearly visible in the CCD image. Moreover, the interaction area of the fiber can be identified through its scattering pattern at high input powers. The waveguide active region can also be captured by the infrared camera through the spontaneous emission pattern once it is pumped. The outline of the test setup is depicted in the following figure. The TEC module sits on a tilt-rotation stage that provides additional degrees of freedom for the critical substrate alignment procedure.

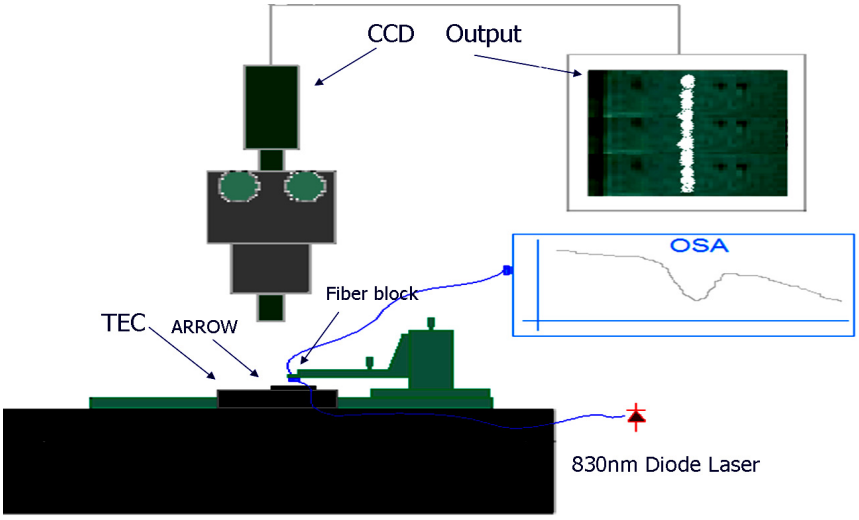

Figure 3.15: An illustration of the test setup.

The fiber is connected to a laser source that is biased below threshold in order to attain a broad spectrum for alignment and gain characterization purposes. Once the fiber and the ARROW were aligned and in contact, a larger forward bias is applied on the ARROW p-i-n junction and the system properties are analyzed through

comparison of the before-and-after OSA spectral data. A fiber polarization controller is inserted between the light source and the coupled region of the fiber to assure TE (or TM) polarized signal passing over the coupling region. Figure 3.16 further illustrates how different elements are positioned when coupling takes place.

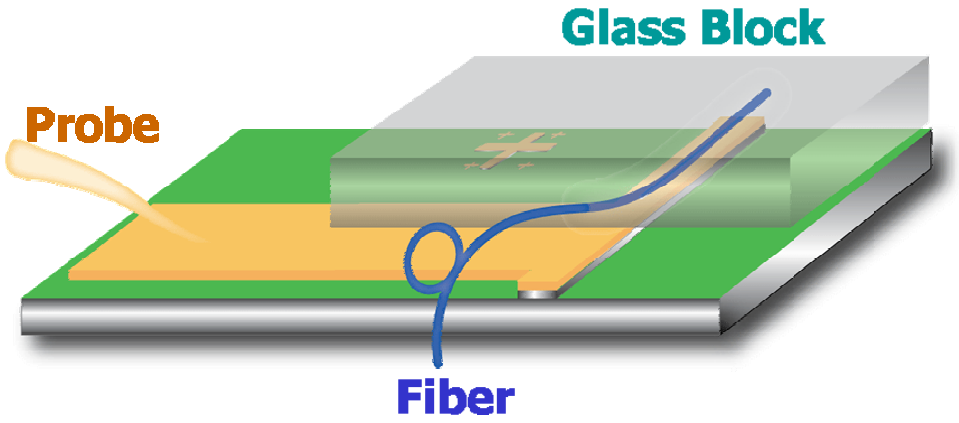

Figure 3.16: The schematic of the side-coupling and electrical probing to a hybrid ARROW-fiber system.

Chapter 4

Incoherent emission in side-coupled semiconductor fiber devices

The very first step in the way of realizing an inline fiber laser is to observe and improve the incoherent light coupling into the fiber from the semiconductor ARROW waveguides. This chapter studies this phenomenon in detail and lays the foundation for the more advanced active devices that follow in the next chapters.

4.1 Theory and operation principle

The light emitter structure of Figure 4.1 is the first active device possible in this technology, as it only requires minimal coupling between the fiber and a forward-biased ARROW.

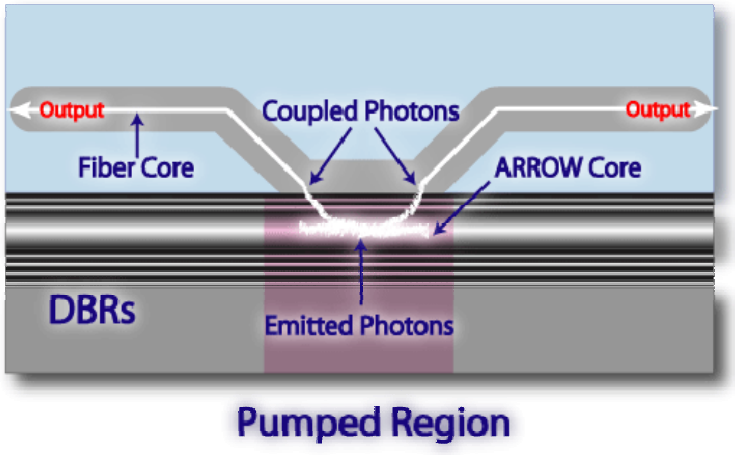

Figure 4.1: The schematic of a side-coupled ARROW fiber light emitter.

At the phase-matching wavelength, photons that are electrically generated in the semiconductor and coupled to the fundamental ARROW mode will travel into the fiber over a certain coupling distance and create a narrowband power spectrum at the output of the fiber. Since the spontaneously-emitted photons have random directions and phases, the actual power coupling efficiency can be very small.

In the absence of other recombination processes, most of the generated carriers in the semiconductor active region take part in the spontaneous emission process and release their energy by emitting incoherent photons into the existing modes of the surrounding cavity. The emitted power is therefore proportional to the pump power, and has a broad radiation spectrum due to various broadening mechanisms in the semiconductor. For an electrically-pumped light-emitting diode, the total generated power is:

$$P = \eta \frac{h\nu}{e} I$$

where η is the LED internal efficiency and $h\nu/e$ is the photon energy in eV. Although the overall electrical-to-optical energy conversion, a.k.a. wall-plug efficiency, may be up to 50% in state of the art LEDs[45], the coupling efficiency into a particular optical mode is quite small. In fact, it is inversely proportional to the number of optical modes in the waveguide. In typical edge-emitting lasers this value[22] is close to 10^{-5}. The planar ARROWs used in the previous work[14] had extremely low efficiencies $<3\text{x}10^{-8}$, and less than 7nW of power coupling into a singlemode fiber was observed. This low efficiency is mostly attributed to the lack of lateral optical and electrical confinement mechanisms in those planar devices. To get around these issues, an etched rib as well as an oxide aperture layer is added to the ARROW design to improve photon/carrier confinement in these waveguides.

4.2 Device layout

The epitaxial structure of these ARROWs is comprised of a 33-pair bottom p-DBR and a 5-pair top DBR enclosing a 2nd order AlGaAs cavity in the center. The structure is similar to that of the first generation lasers (Figure 6.7 in chapter 6) and

will be discussed in more details later in that chapter. A 75Å GaAs QW in the center of the cavity traps and recombines the pumped carriers into photons. The QW is designed to have a photoluminescence peak at 840nm to compensate for the red-shift due to heating and bandgap shrinkage effects. Following the epitaxy, the ARROW waveguides are fabricated on the substrate after multiple dry-etch, oxidation, passivation, and metallization steps that will be described in appendix A. These waveguides are the centerpiece of our devices that sit under the exposed fiber core in the coupling experiments.

4.3 Results

Following device fabrication, the waveguides were brought into contact with a singlemode fiber. The ARROWs were pumped by a pulsed current source, at a pulse width of 1 μs and 1.6 kHz repetition rate, to create carriers in the quantum wells without generating too much heat.

Figure 4.2 illustrates the L-I data for a 10x800μm ARROW. A maximum of 12 μW power is directly coupled into a singlemode fiber in our experiments. The power-coupling efficiency, defined as the ratio of the power detected in the fiber to the total optical power generated in QWs, is around $4x10^{-6}$, which is about two orders of magnitude larger than the previous work and closer to the values for conventional edge-emitting lasers. This improvement is mainly attributed to the lateral optical and electrical confinement implemented by the etched rib and the oxide aperture.

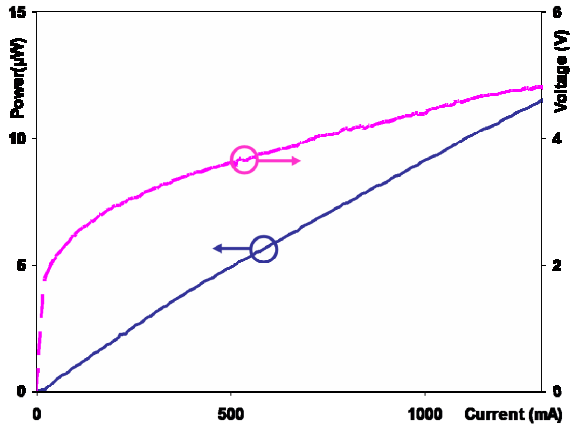

Figure 4.2: The L-I-V curves of the side-coupled light emitter.

Figure 4.3 shows the spectrum of the spontaneously emitted photons (from the GaAs QW) that couple into the fiber in the phase-matching window. The resonance peak is located at 846.5nm. Since the original GaAs SE spectrum is very broad, this measurement is an effective indicator of the resonance wavelength of these systems. For comparison, the spontaneous emission spectrum from a microcavity structure on the same wafer is also shown in the figure. As expected, this spectrum is very wide and spans more than 60nm. The large ripples in the microcavity SE spectrum are a result of spectral modulation by the off-resonance reflectivity peaks of the DBR.

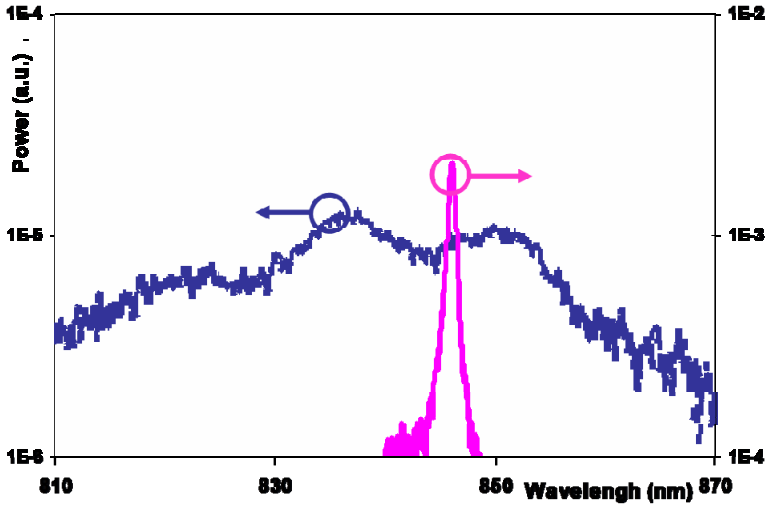

Figure 4.3: Relative spectra of the broadband spontaneous emission from a micro-cavity (pink curve) as well as the ARROW-fiber light emitter (blue curve).

Although using an oxidized two-mesa ARROW structure, a significant boost in the coupling efficiency is achieved, the output power is nowhere near sufficient for most optoelectronics applications. A laser, on the other hand, can get around the SE limitation as it couples most of the carrier energy into the lasing mode through the stimulated emission process. Possible laser architectures will be studied in the next chapters.

Chapter 5

Side-coupled semiconductor fiber amplifiers

In this chapter we present a design that can be used as a fiber semiconductor optical amplifier. Although this device suffers from the same shortfalls of the modulators, namely polarization dependence and narrow bandwidth, it is an important stepping stone to the fiber lasers of the next chapter.

5.1 Introduction

Advances in fiber amplifier technologies in the last decade have paved the way for rapid growth of high capacity networks worldwide. Erbium doped fiber amplifiers (EDFAs) have been widely used as the gain medium in optical networks, mostly due to unique advantages they hold over semiconductor amplifiers, including bandwidth, noise, insertion loss, and polarization independence. Nevertheless, semiconductor optical amplifiers (SOAs) benefit from large gain and nonlinearity of semiconductors and have been used in some applications where a smaller and cheaper alternative to EDFAs is favored[46,47]. However, reduction of fiber insertion losses and suppression of the spectral ripples caused by facet reflections remain a challenge for these systems. Consequently, high quality SOA modules can be similarly expensive, due to the complicated alignment procedures involved for coupling into singlemode fibers and for the precise antireflection coatings needed on the facets. Again, we can take advantage of the evanescent coupling between a side-polished fiber and an active GaAs device here in order to replace the conventional chip-to-fiber butt-coupling method.

5.2 Amplifier architectures

Figure 5.1 depicts the schematic of the proposed amplifier. Ordinarily, we would like the interaction length to be around two coupling lengths, so that the light gets back into the fiber after coupling to the semiconductor.

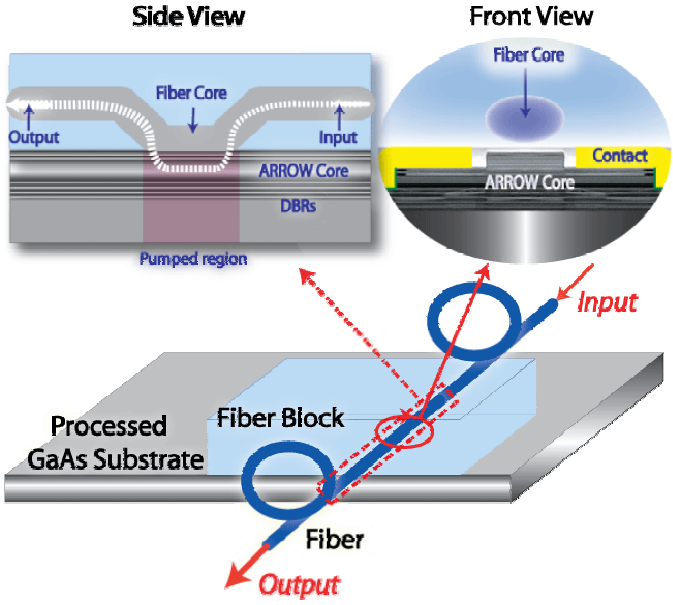

Figure 5.1: The schematic of a hybrid ARROW-fiber amplifier.

If the semiconductor is pumped, the QW gain can translate into a net amplification of the input fiber signal through the evanescent coupling process. This amplification level is nevertheless dependant on the coupling factor and varies considerably at different gain and loss numbers, as shown in the following figure.

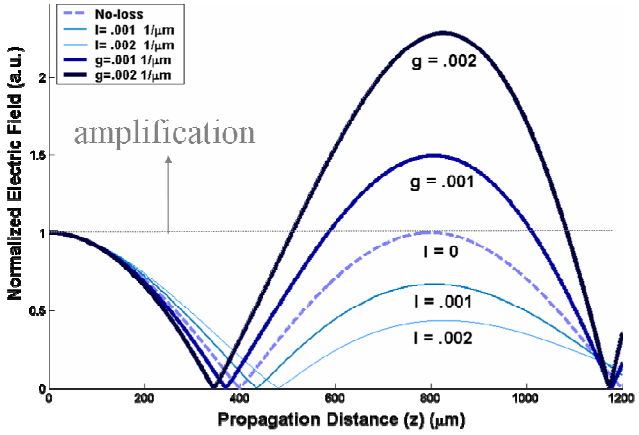

Figure 5.2: Electric field amplitude in the fiber as a function of the coupled-length for various loss/gain levels in the ARROW. The coupling length in these calculations is 400μm.

Since the evanescent coupling process is highly wavelength-selective, the resulting amplification spectra are very narrowband. Figure 5.2 captures this dependence for different loss and gain levels. This derivation assumes an interaction length ~1mm and a coupling length ~0.5mm. The spectrum is also very sensitive to the input polarization, since the QW gain is typically small for TM signals.

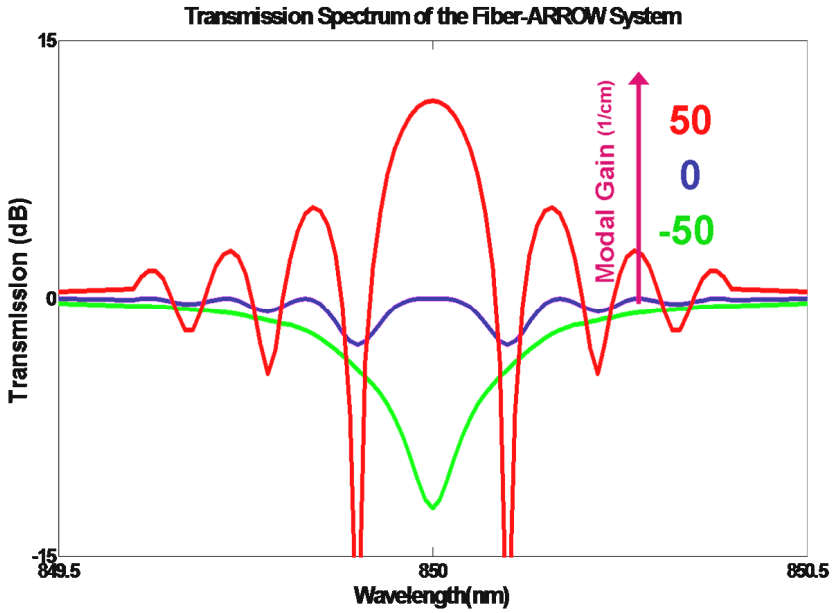

Figure 5.3: Simulated fiber transmission spectrum for different modal intensity-gain levels in a hybrid fiber-ARROW amplifier of Figure 5.1.

With no current passing through our devices, the optical loss of the ARROW results in a clear notch at the phase-matching wavelength, indicating a slow power transfer from the fiber into the ARROW waveguide. As the pump current increases however, the QW becomes transparent and the waveguide loss drops significantly; therefore the notch initially gets narrower and deeper as the effective coupling length is reduced. At higher currents, the coupling increases and results in a narrow amplification peak. This is accompanied by some ripples in the spectrum, as the coupling factor change is highly wavelength dependant. This behavior perfectly matches the intuition developed from the coupled-mode equations as described in the previous chapters.

As a result of the small phase-matching linewidth, the amplified spectra have very sharp peaks. Although such a small linewidth and high polarization sensitivity

may not be ideal for wideband amplification of multiple fiber channels, it can be an ideal gain cell for lasers. Moreover, these devices can be attractive for pre-amplification of weak laser signals. The system bandwidth can increase if needed; either by reducing the coupling dimensions or through a cavity taper implemented to widen the operating linewidth of these devices.

While this amplifier architecture is very straightforward, it is not very efficient, as only a slight portion of the generated carriers in the active region are used to amplify the fiber signal. To quantify this effect, an equivalent gain length (l_{eff}) is defined so that the net amplification in the fiber (G) is equal to: $G=exp(g.l_{eff})$. Figure 5.4 plots ratio of the effective gain length to the pumped area ($l_{eff}/l_{coupled}$) as a function of the normalized interaction length for various waveguide intensity-gain levels.

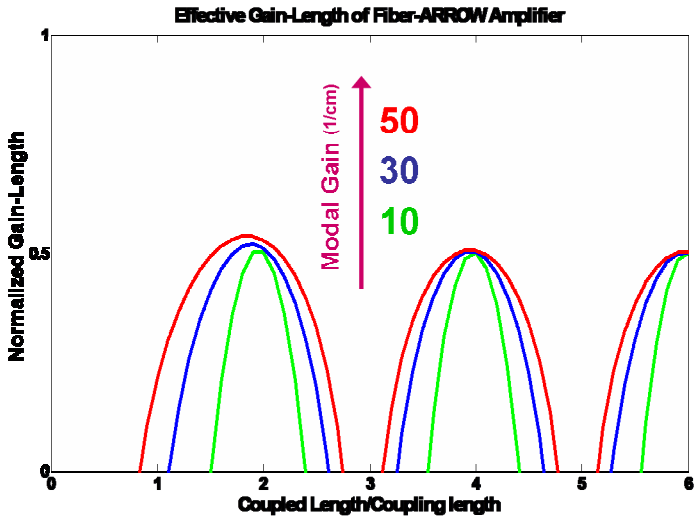

Figure 5.4: Effective gain length ($l_{eff}/l_{coupled}$) of the fiber amplifier as a function of the normalized coupled length ($l_{coupled}/l_{coupling}$). The physical interaction length is set to 1mm.

A more efficient architecture can be conceptualized by folding the direct amplifier structure of Figure 5.1 to effectively half the pumped region at the same total gain level. This will require a mirror on the ARROW side, which can be realized by cleaving the semiconductor facet. This reflective amplifier is the centerpiece of the inline lasers in the next chapter, and will be studied in more detail later. Figure 5.5 depicts such a reflective amplifier.

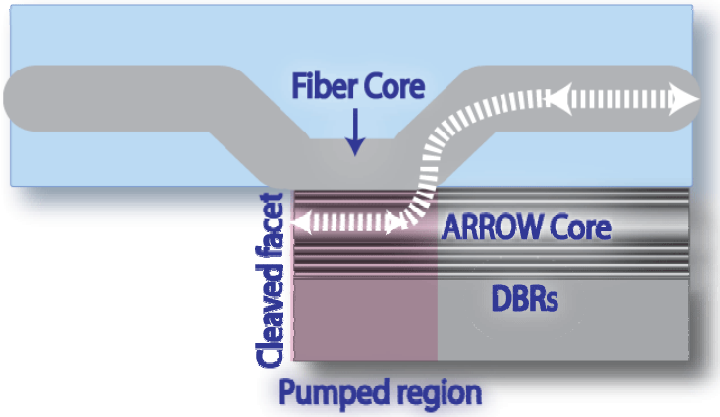

Figure 5.5: An illustration of a reflecting fiber-ARROW amplifier.

An even more efficient design involves partitioning the interaction region into separate coupling and gain areas. In this method, the coupling regions are designed to transfer the power completely from one medium to the other, while the center region can be pumped heavily and independently for maximum gain. Since the modal power is confined in the ARROW over the entire gain region, the interaction is maximized and the normalized gain length ($l_{eff}/l_{coupled}$) gets close to unity. Figure 5.6 shows an illustration of this idea for the forward-path amplifier of Figure 5.1.

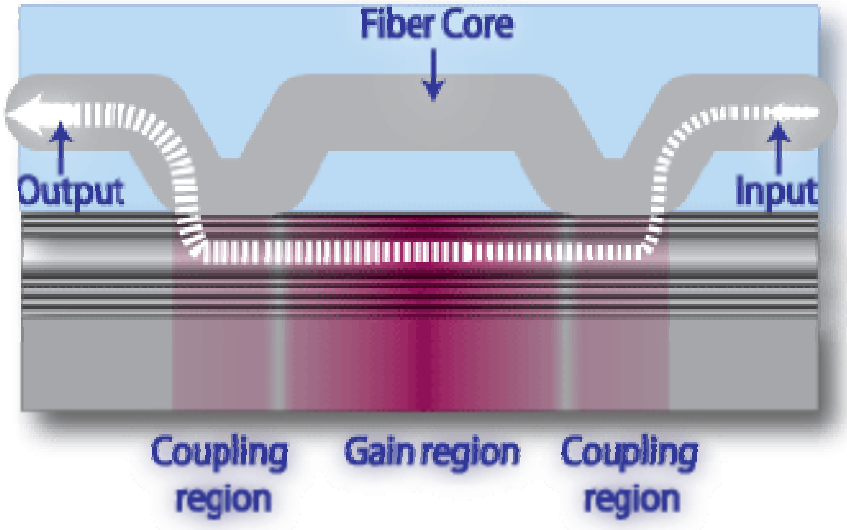

Figure 5.6: A high efficiency design for a hybrid fiber-ARROW amplifier.

5.3 Device layout

The ARROW design used for these amplifiers is similar to the epitaxial structure of second generation lasers (Figure 6.19 from next chapter), which will be studied later in this document. This design includes 33 and 5 pairs of bottom and top DBRs, respectively, along with 6 QWs to provide enough gain at the operation wavelength (850nm).

5.4 Testing amplifiers

Testing these amplifiers is very challenging, not only because the spectrum is very narrow, but also due to spectral masking by the aforesaid coupling of spontaneous emission. This phenomenon occurs when the broadband input source is too weak to overpower the spontaneous emission power that is coupled into the fiber when the ARROW waveguide is pumped. The SE can overwhelm the weaker gain spectrum and provide erroneous results. Even with a narrowband laser signal, unwanted reflections as well as the ARROW spontaneous emission can couple back to the input source and alter the lasing spectrum. It is therefore mandatory to use a fiber-coupled tunable laser source with an isolator to provide a reliable input signal for this measurement. Unfortunately, such a laser source was not available to us at the time and direct measurements of the amplification spectra were not possible. The peak amplification level can be indirectly measured however, if the amplifier is used as a gain cell in a fiber laser. At threshold, the gain of this amplifier has to be equal to the external losses of the laser cavity. For the reflective amplifier structure of Figure 5.5, we can measure the gain using this technique. Such measurements indicate that at 300mA, the amplifier has a single-path gain of around 5dB. Details of this calculation will follow in the next chapter.

Chapter 6

Side-coupled semiconductor fiber laser

Since their invention in the early 1960's, semiconductor lasers have dominated the market for coherent light worldwide. They have found widespread application in telecommunications, optical storage, and many other markets. This has resulted in an extensive research effort in the past decades, on such lasers, even after the substantial market shrinkage following the 2001 economic downturn. A great part of this effort has been focused on fabrication of cheap high quality lasers for telecom applications, where high speed data transmission sets strict limits on the spectral purity of the laser signal. Although some progress has been reported[32], material and process restrictions have largely limited the success of such devices. In this chapter we present an alternative device that carries many of the advantages of the high-quality fiber-coupled lasers into a small, potentially cheap package that can be batch-fabricated in a conventional semiconductor processing technology.

6.1 Introduction

Evanescently coupled light sources, particularly lasers, are well suited for telecommunications, not only because butt-coupled counterparts are costly and inefficient, but also because the inherent polarization sensitivity and narrow linewidth of these devices are ideal for these applications. In the following sections, we discuss the advantages of this side-coupled architecture over conventional laser modules and describe its operation principles. Finally we present the experimental data from first and second generation devices fabricated on this platform, and compare the results

with the theoretical expectations. Figure 6.1 depicts the schematics of the described fiber-ARROW laser system.

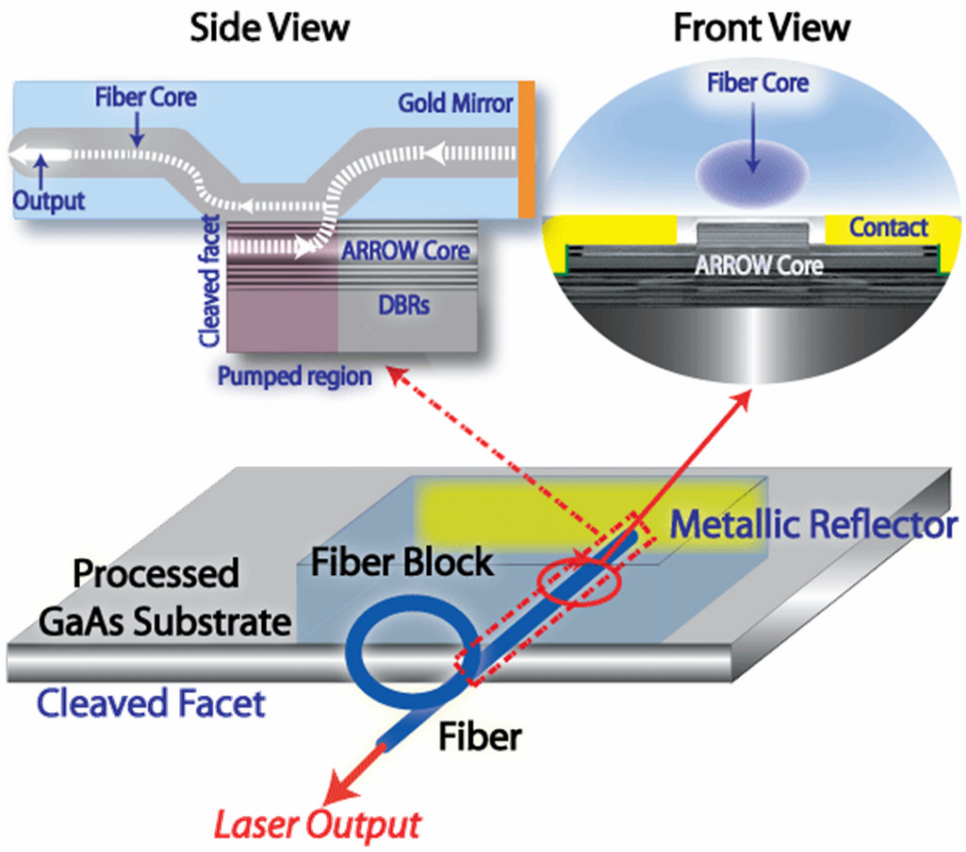

Figure 6.1: Schematics of a side-coupled fiber-ARROW laser.

6.2 Advantages over free space coupled lasers

In addition to the challenging alignment and packaging process that was discussed in the earlier chapters, conventional edge-emitting lasers suffer from other limitations that further compromise their performance. Most importantly, semiconductor edge-emitting lasers have many closely-spaced axial modes that result in low spectral purity and strong wavelength-temperature dependence. Consequently, distributed feedback (DFB) or distributed Bragg reflector (DBR) techniques have been used to ensure stability and single-frequency operation in these lasers, further adding to the device fabrication cost and complexity.

6.2.1 Mode selection and side-mode suppression ratio

A laser with multiple axial modes can be stabilized by adding a high-Q filter to the feedback loop in order to suppress lasing in all out-of-band modes. A DBR laser, as discussed previously, is an effort to implement such a filter in an otherwise multimode edge-emitting laser. The small resonant linewidth of the ARROW-fiber system is extremely advantageous in this context, since it acts as a virtual grating that stabilizes the lasing wavelength and insures singlemode operation. An important figure of merit for singlemode lasers is the side-mode suppression ratio (SSR), which is defined as the ratio of power in the desired lasing mode divided by the power in the largest axial side-mode. An SSR value of more than 30dB is typically required in high speed telecom applications.

6.2.2 Thermal stability

In addition to multimode operation, simple edge emitters are also very temperature sensitive, since the wavelength is primarily determined by the material gain, which is a strong function of temperature. Stabilized lasers such as DFBs, on the other hand, show a much weaker dependence, because the wavelength is fixed by physical dimensions and refractive indices, which vary slowly with temperature. Similarly, the lasing wavelength in this hybrid ARROW-fiber laser is highly stable, as it merely follows the refraction indices of the semiconductor. Like the tunable DBR lasers, the wavelength of this ARROW-fiber laser can be thermally tuned within a range of few nanometers.

6.2.3 Catastrophic optical mirror damage

Since the power extraction in an edge-emitting laser is through a semiconductor cleaved facet, these devices are prone to catastrophic optical mirror damage (COMD) at high output power levels. Interestingly, here the output coupler will be in the fiber and nothing exits the semiconductor facet. This greatly diminishes the prospects of catastrophic optical mirror damage in these devices, as the effective

light intensity at semiconductor facets is very small. These lasers are thus excellent candidates for high power applications.

6.2.4 Batch fabrication and laser arrays

One of the biggest advantages of the fiber-ARROW lasers is the possibility of batch fabrication. An array of these devices can be fabricated on the same substrate and bonded to a V-grooved side-polished fiber chip[38] to realize a fiber laser array, as depicted in Figure 6.2.

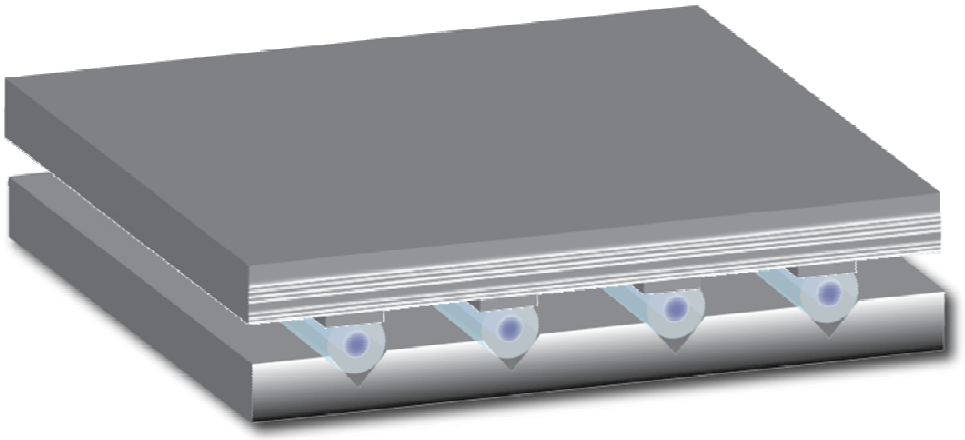

Figure 6.2: Evanescent coupling between a V-grooved polished fiber chip and ARROW waveguides.

Instead of multiple fibers, one fiber can be wrapped around to feed all the devices. This topology can be very useful for high power applications. Moreover, if we intentionally taper the ARROW cavity, the coupling wavelength changes from one device to the other, thus multiple wavelengths can simultaneously lase and couple into this fiber. With careful design, some level of wavelength tuning can therefore be realized in these lasers.

6.3 Operation principle

Figure 6.3 illustrates the feedback method employed in this architecture. At the phase-matching wavelength, a portion of the electrically generated photons in the fundamental ARROW-mode couple into the fiber; get reflected by a mirror, and couple back into the semiconductor over the interaction region. The cleaved

semiconductor facet closes the feedback loop by providing a second mirror for this laser. The interaction length between the waveguide and the fiber is designed to allow a small portion of the circulating power leak out to the output port of the laser. In the following sections we explain some of the important attributes of these fiber-coupled devices.

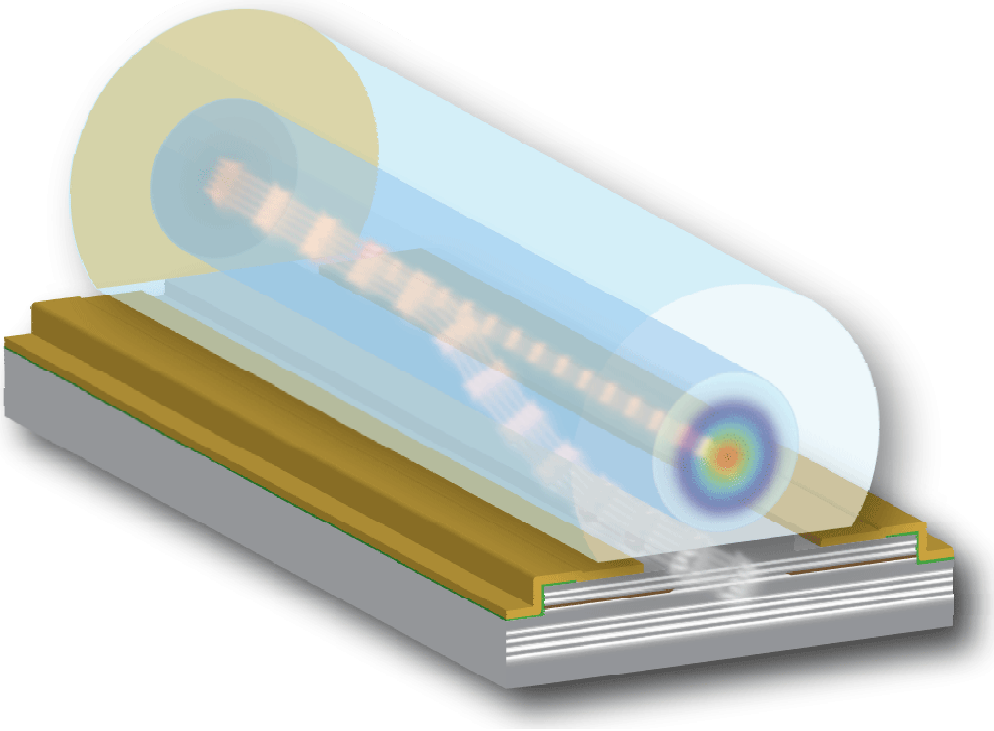

Figure 6.3: A 3D illustration of the side-coupled fiber-ARROW laser.

6.3.1 The coupling filter

The coupling spectrum is strongly dependent on the length of the interaction region as well as the gain of the quantum wells, which goes up slowly as we inject more current into the active region. This will in turn change the profile of the stabilizing filter until the system satisfies the threshold condition. After this point, the gain stays constant at its threshold value and filter characteristics becomes stable, provided that the temperature is kept steady. Figure 6.4 depicts the dependence of the roundtrip gain spectrum on the coupling parameters and modal intensity gain in the laser implementation of Figure 6.1.

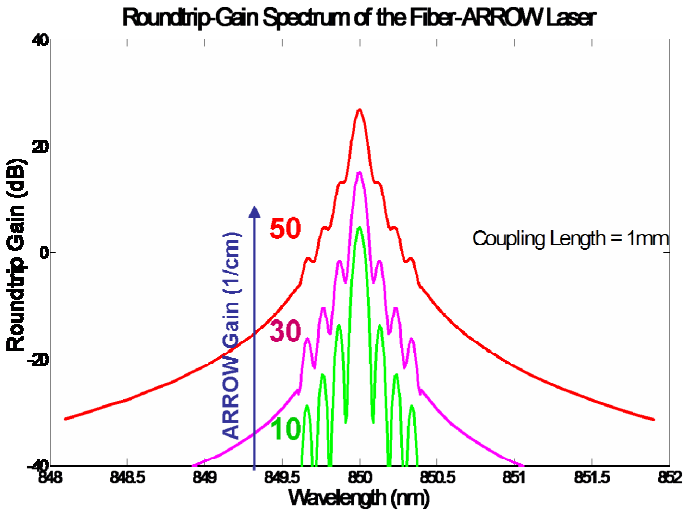

Figure 6.4: Round trip gain spectrum of the hybrid laser at different gain levels ($l_{coupling}$= $l_{coupled}$=1mm).

The above curves state that for a threshold roundtrip gain of ~10dB at 850nm, the filter introduces selective loss of at least 10dB over a 0.2nm spectrum, which is enough to guarantee singlemode operation unless the length of the cavity becomes excessively large.

6.3.2 The laser mirrors

Unlike edge emitters, the cleaved semiconductor facet here is an almost-perfect reflector, since the mode rays meet the interface at an angle larger than θ_c (critical angle), as shown in Figure 6.5.

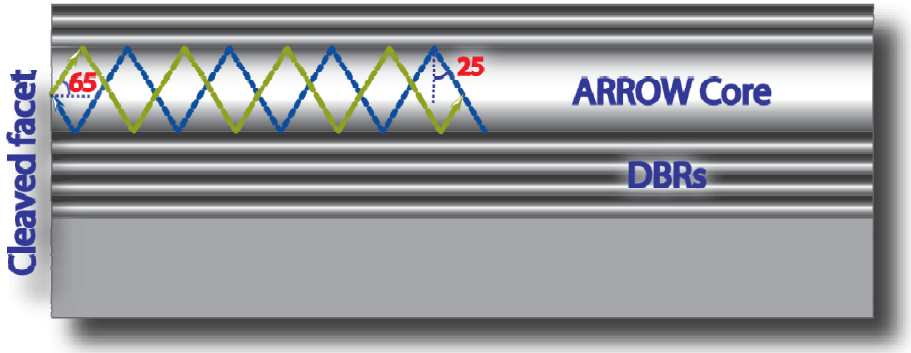

Figure 6.5: Illustration of the high facet reflectivity for ARROW modes. θ_c~17º at GaAs-air interface.

However, due to facet roughness, as well as loss of the evanescent field (the portion travels without reflection in the fiber cladding), this mirror shows some loss.

The power lost in this evanescent portion of the ARROW mode may contribute up to ~1-2dB to the mirror loss, depending on its epitaxial structure. Implicit in this derivation is the assumption of an air cladding over the ridge structure.

The fiber mirror can be realized either by inline gratings or through metal deposition on a polished tip of the fiber. Although fiber gratings are very versatile and have low insertion loss, they are hard to fabricate at 850nm. Moreover, these gratings are usually very narrowband, thus careful alignment of the reflection band and the coupling bandwidth is essential. Instead, metal coated tips provide a wide-band reflector and are cheaper to fabricate at small scales. The reflectivity of various metals[48,49] is listed in table 6.1.

Metal	***Wavelength (nm)***	***n***	***k***	***Normal Reflectivity***	***Mirror Loss (dB)***
Aluminum	850	2.1	7.1	0.86	0.67
Gold	850	0.1	5.5	0.99	0.05
Silver	850	0.1	5.8	0.99	0.05
Titanium	820	3.2	4.0	0.61	2.13

Table 6.1: Optical charactristics of different metals for fiber mirrors.

While gold is an ideal candidate, it rarely sticks to any surface, so we used aluminum to coat the fibers in this implementation. The resulting fiber mirror together with its connectors shows a cumulative loss of around 3dB. It is important to note that the nominal FC/PC connector loss at 850 nm is around 0.5 dB, but can reach as high as 1dB in practice.

6.3.3 Suppression of the edge-emitting modes

While the preferred mode of lasing is in the aforementioned hybrid (ARROW+fiber) cavity, other modes can coexist with this one in these lasers. The semiconductor edge-emitting modes are especially troublesome, as they can sweep the

generated carriers into their own lasing modes and eventually dominate over the desired composite mode. It is therefore essential to provide a mechanism to eliminate the prospects of lasing in such modes. In order to prevent reflections into the semiconductor and suppress lasing inside the AlGaAs material, we etch one end of the ARROWs at an angle with respect to the waveguides, as shown in Figure 6.6. This effectively reduces any coherent reflections off this facet and makes only the hybrid-mode lasing feasible. This feature can also be seen on the ARROW SEM images of Figure 6.9.

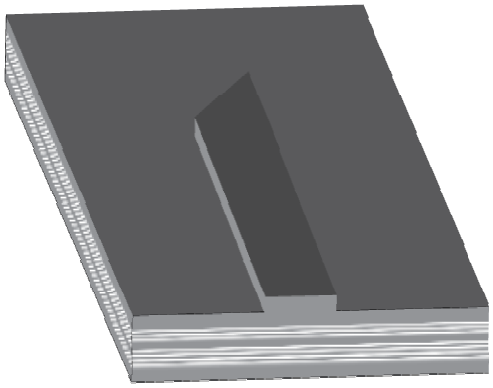

Figure 6.6: The angle-etched facet, as well as the cleaved facet of the ARROW designed for hybrid lasers.

6.3.4 Polarization

One of the most important sources of loss in this laser is polarization mismatch. As discussed before, the QW gain is highly polarization dependant, with minimal matrix elements for the TM polarization. Therefore, these devices can only lase efficiently in the TE mode. Moreover, the phase-matching wavelength is very different for the two polarizations. It is therefore critical to keep the polarization unidirectional in the round trip; otherwise the feedback factor becomes prohibitively small.

Polarization loss is especially troublesome here, since long fiber lengths are used to overcome various technical challenges and to recycle the fiber blocks between many experiments. It is therefore essential to carefully control the polarization for these lasers to assure proper operation. It is worthwhile to note that in a batch

fabrication process, the polarization-rotation loss becomes negligible, since the fiber length can be made very small.

6.4 First generation lasers

The first generation devices were fabricated by metal-organic vapor phase epitaxy (MOVPE) of the epitaxial structure on an n+ GaAs substrate. The layer stack, shown in Figure 6.7, is comprised of a p-i-n diode structure that included a 33-pair n-doped $Al_{.2}Ga_{.8}As/Al_{.95}Ga_{.05}As$ bottom DBR with an $Al_{.98}Ga_{.02}As$ oxide aperture layer, an intrinsic active region containing three 75Å GaAs quantum wells, and a 5-pair p-doped upper $Al_{.2}Ga_{.8}As/Al_{.8}Ga_{.2}As$ DBR. The quantum wells had a photoluminescence peak at 840nm and lasing peak at 850nm, where the 10nm difference was due to carrier induced and thermal shrinkage of the bandgap during laser operation.

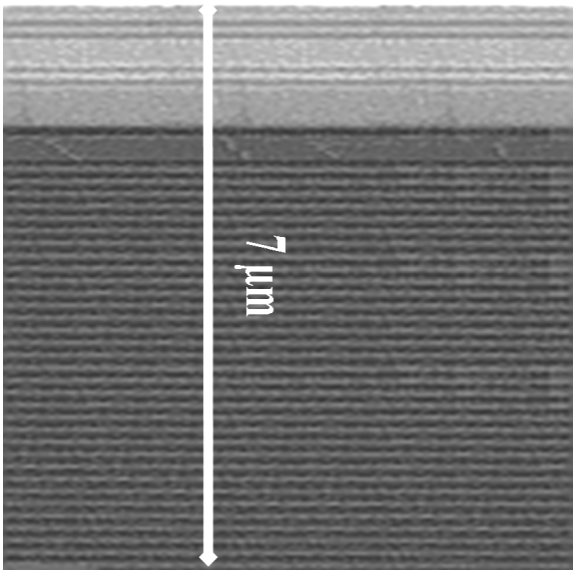

Figure 6.7: A SEM micrograph of a first-generation ARROW epitaxial structure.

Figure 6.8 also depicts the simulated modal profile of an etched ARROW. The outline of the epitaxial structure is also shown in this figure.

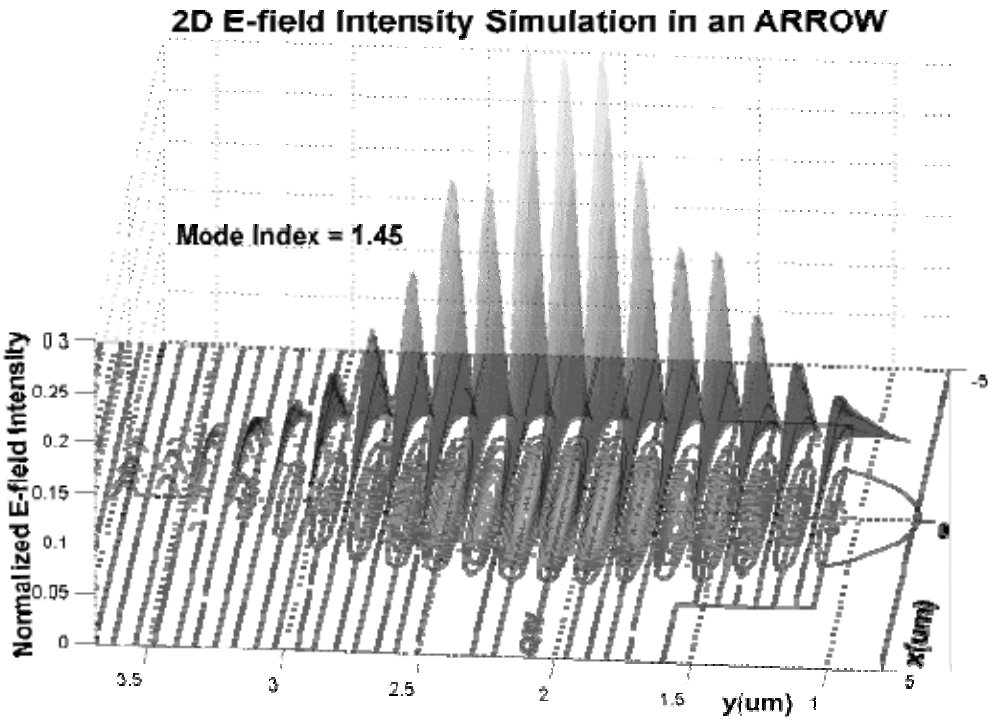

Figure 6.8: Electric field intensity distribution of the fundamental mode of the ARROW of Figure 6.7. Outline of the epitaxial structure is shown in the x-y plane.

A standard dry-etch step cuts through the cavity and stops under the oxide aperture layer to define the larger mesas used for metallization. Next, the substrate is patterned and dry etched to realize the ridge ARROWs and to expose the highly doped p-contact layer. This step is followed by oxidation in a hot steam saturated, N_2-ambient furnace to provide a current-confinement aperture in the center of the waveguide. To passivate the devices, a thin silicon nitride layer is deposited and patterned on the wafer. Photolithography, metal deposition, and lift-off processes are then carried out to make Ti/Au contacts to individual waveguides and interconnect these devices to the electrical probe pads. An n-contact metal stack is also evaporated and annealed on the backside. Details of the fabrication processes can be found in appendix A. The wafer is then cleaved into small pieces in order to couple to the fiber in our test setup. Scanning electron micrographs of the fully-processed ARROWs are shown in Figure 6.9.

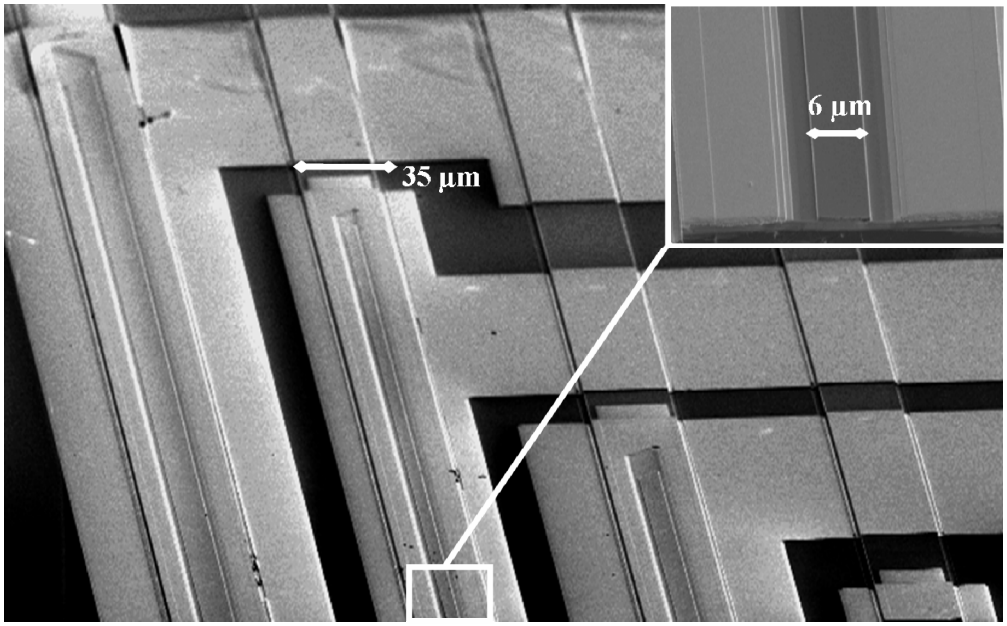

Figure 6.9: SEM micrographs of the fully-processed ARROWs.

6.4.1 Results

After coupling to the fiber, the ARROWs were pumped by a pulsed current source at a pulse width of 0.2 µs and a duty cycle of 0.2% to provide gain in the QWs without generating excessive amounts of heat.

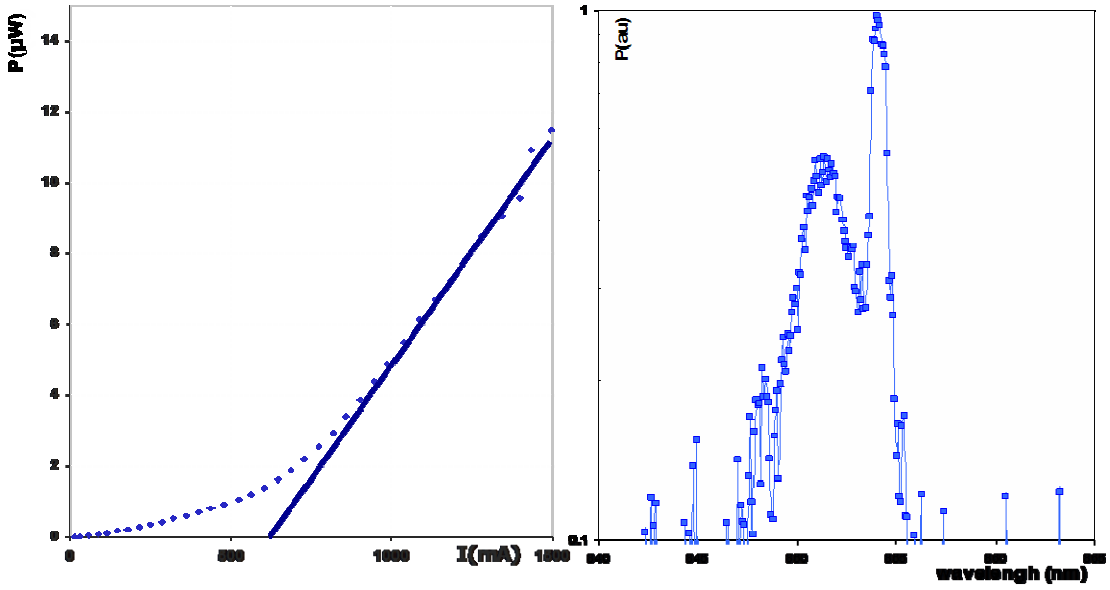

Figure 6.10: The L-I curve, as well as the spectrum of a first generation hybrid laser.

Figure 6.10 depicts the luminescence vs. current (L-I) curves and the lasing spectrum of a 20x1000μm ARROW, showing a slow turn on at 600mA (equivalent to a threshold current density of 3 kA/cm^2) and a narrowed spectrum at 854nm. The laser output power is nevertheless very small and only 12μW was detected.

6.4.2 Troubleshooting

The small power should not come as a surprise. The highly-doped top DBR layers contribute heavily to the ARROW modal loss, and poor current spreading in this region severely reduces the overlap between the gain profile and the optical mode. This becomes more evident in Figure 6.11, where a CCD camera is used to image the profile of spontaneously-emitted photons in the plane of the quantum wells.

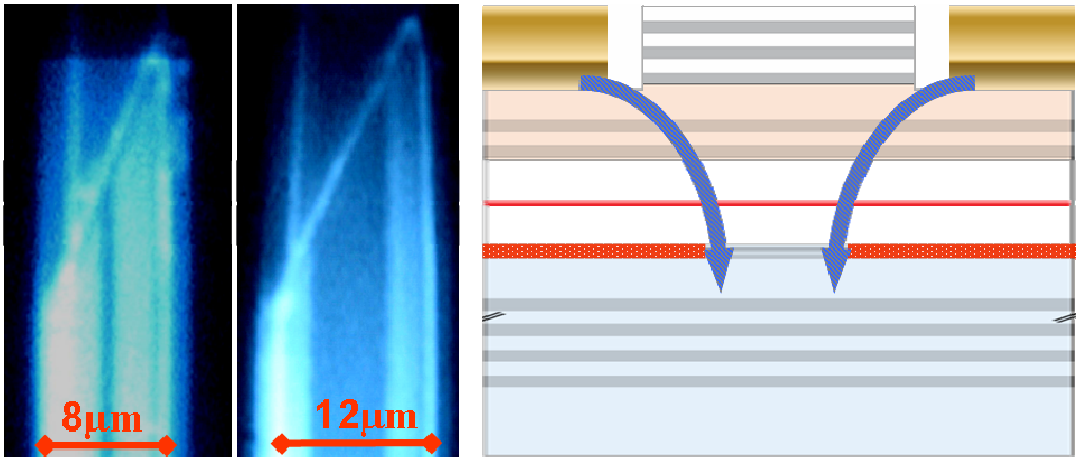

Figure 6.11: CCD images of two ARROWs with different current apertures, showing a dark area in the center. An illustration of the current distribution profile is shown on the right.

The center areas in both waveguides are clearly dark, implying that most of the injected current is crowding around the edges of the oxide aperture, rather than flowing toward the waveguide center. This is in spite of the high doping (~3x10^{19}cm^{-3}) at the top 0.5μm-thick DBR mirror. Moreover, this doping drastically increases the ARROW-loss and causes further reduction in the output power of the laser.

6.5 Threshold and quantum efficiency

Threshold and differential quantum efficiency are the two most important figures of merit for a semiconductor laser. In this section, we try to calculate these parameters and identify important design variables that can change these numbers. The result of this analysis is used in the following sections to greatly improve the overall performance of these systems.

6.5.1 Threshold calculations

To calculate the threshold of these lasers, we need to have an accurate estimate of various sources of loss in these devices. We use the data from chapter three to approximate the ARROW waveguide loss:

$$\alpha_{ARROW} = \zeta\, \alpha_{material} + \alpha_{scattering}$$

where $\alpha_{scattering}$, $\alpha_{material}$, and α_{ARROW} are the scattering, material and the total loss of the ARROW waveguide, respectively. ζ stands for the previously-defined loss enhancement factor of ARROW modes. The quantum well gain is also amplified by the same factor:

$$g = \Gamma\, \zeta\, m g_0 \ln(\frac{J}{mJ_{tr}})$$

This is the same formula as the one discussed in chapter 2, with the addition of ζ and Γ terms. Γ stands for the vertical confinement factor of the QWs, which is about 1% in the ARROW of Figure 6.7. The roundtrip gain is therefore: $G = \exp(2g \cdot l_{eff})$.

It is important to note that l_{eff} is different from the length of the pumped region, as it measures the effective gain-length seen by the mode. This is, in effect, an effort to quantify the longitudinal overlap between the lasing mode and the semiconductor gain medium. This factor is studied more closely in the context of differential quantum efficiency later in this chapter. All other losses in the system are lumped into the α_{cavity} parameter below. Main contributors are the output, mirror, coupling, scattering, and polarization-related losses:

$$\sum \alpha_{loss} = \alpha_{ARROW} + \alpha_{cavity} \qquad \left(\alpha_{cavity} = \alpha_{output} + \alpha_{mirrors} + \alpha_{coupling} + \alpha_{misc.}\right)$$

The threshold condition is therefore:

$$g_{th} = \sum \alpha_{loss}$$

6.5.2 Differential quantum efficiency

Compared to edge-emitting lasers discussed in the earlier chapters, the differential quantum efficiency (η_d) of these hybrid devices has some extra terms that require special attention.

$$\eta_d = \frac{\eta_{leakage}\eta_{coupling}\eta_i \cdot \alpha_{output}}{\sum \alpha_{loss}}$$

The first factor, $\eta_{leakage}$, takes into account the current leakage in the shunt resistive (or capacitive) paths. The leakage current cannot generate electron-hole pairs that can participate in the stimulated emission process and should therefore be excluded from the quantum efficiency calculations. It will also limit the threshold, as the current term in the gain formula should not include this lost fraction.

The coupling factor, $\eta_{coupling}$, is more subtle, and needs more detailed analysis. The origin of this term lies in the hybrid nature of this system. Since the composite mode travels between the ARROW and fiber, its interaction with the gain region can be much less than the modes that lie completely inside the semiconductor. Simply put, this term captures the overall effect of the optical-mode/gain overlap in the propagation direction. The effective gain length, $l_{eff} = \eta_{coupling}.l_{pumped}$, can therefore be considerably smaller than the pumped region. For instance, if the interaction length is twice the coupling length, the light is mostly coupled back into the fiber (at the output port in Figure 6.1), and little is reflected into the circulating laser mode (small l_{eff} and $\eta_{coupling}$). Figure 6.12 plots this dependence as a function of the normalized interaction length.

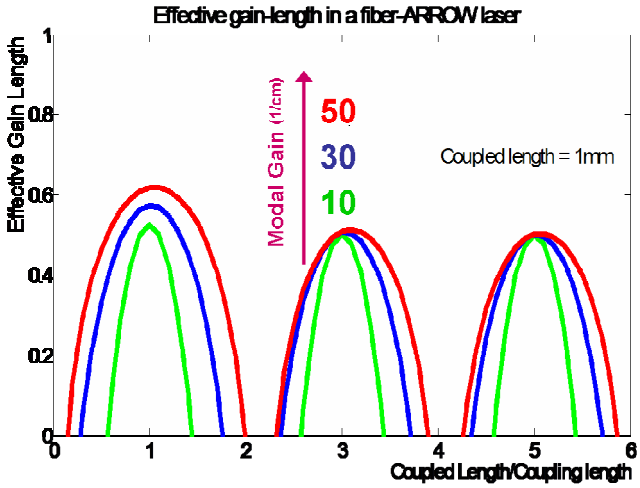

Figure 6.12: Normalized effective gain length ($l_{eff}/l_{coupled}$) of the fiber laser as a function of the normalized coupled length ($l_{coupled}/l_{coupling}$) for $l_{coupling}$=1mm.

It is clearly seen in this figure that the $\eta_{coupling}$ diminishes at even multiples of the coupling length, in line with our earlier remarks. The $\eta_{coupling}$ factor is nevertheless only half of the story. The output coupler, α_{output}, also needs to be taken into account for efficiency calculations. The following figure depicts the dependence of the output coupler on the normalized interaction length. Contrary to the previous case, the output coupling is maximized at even multiples of the coupling length, where most of the power gets coupled back to the fiber.

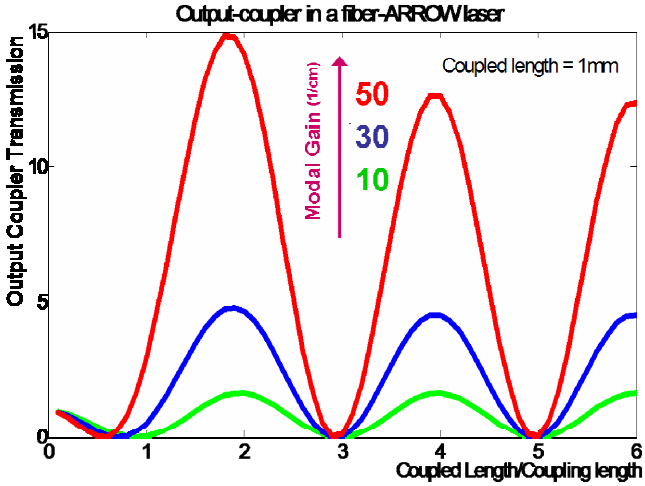

Figure 6.13: Transmission through the output coupler as a function of the normalized coupled length ($l_{coupled}/l_{coupling}$). Here $l_{coupling}$=1mm.

These opposing trends imply the existence of an optimal point for the coupling factor. It is clearly seen in Figure 6.14, which depicts the product if the two terms $\eta_{coupling} \cdot \alpha_{output}$.

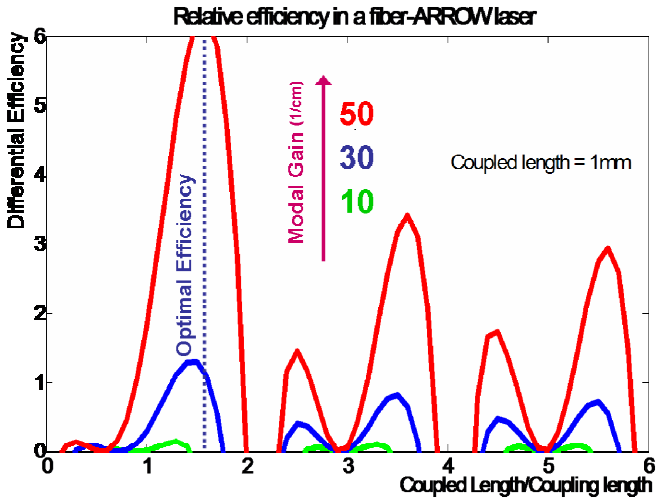

Figure 6.14: The relative differential efficiency of the hybrid laser as a function of the normalized coupled length ($l_{coupled}/l_{coupling}$). Here $l_{coupling}$=1mm.

If other losses in the cavity dominate ($\alpha_{output} < \sum \alpha_{loss}$), this graph fully depicts, aside from a proportionality constant, the dependence of the quantum efficiency on the normalized interaction length. It is nevertheless advantageous to somehow decouple these two trends, so that both can be independently optimized. Such an architecture will be presented at the end of this chapter.

It is also important to study the effects of an air gap between the waveguide and the fiber, on the threshold and quantum efficiency of these lasers. It is worthwhile to recall that the coupling strength between the waveguide and the fiber directly affects the quantum efficiency and the threshold of these lasers. Thus, in order to improve the performance, the fiber needs to be in optical contact with the waveguide; otherwise the coupling strength degrades exponentially as the thickness of the air gap between the ARROW and the fiber increases. As shown in Figure 6.15, a roughly 50nm air gap in this system is enough to completely suppress lasing in the hybrid mode. It is therefore essential to avoid such air gaps in the coupling setups. Although such alignment accuracy is hard to achieve in a manual coupling setup, a robust

bonding process can prevent this air gap and assure optical contact between the substrate and fiber.

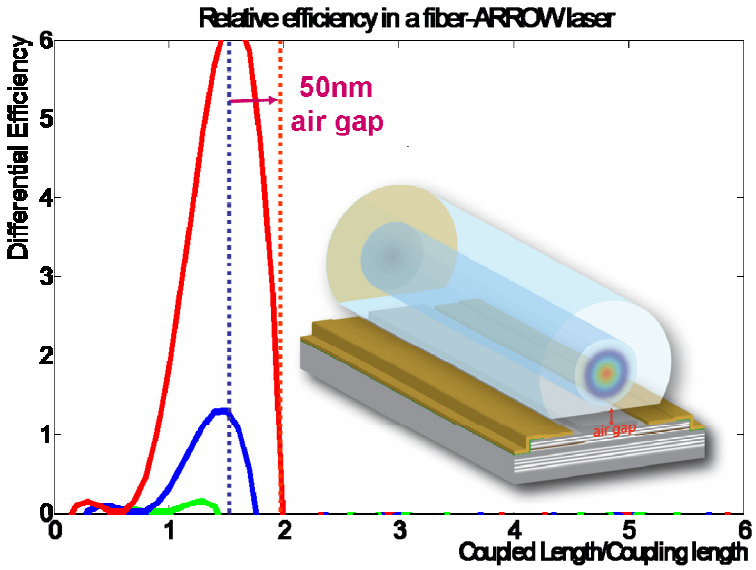

Figure 6.15: Effect of an air-gap on the laser quantum efficiency.

6.6 Current distribution profile

The tradeoff between the optical loss and conductivity of the top DBR mirror, which was encountered in the previous section, is in fact one of the biggest design challenges to realizing an efficient laser in this technology. Higher doping levels provide better conductivity, but at the cost of greatly increased optical loss. The low mobility of holes in GaAs further amplifies this problem. In this section, we try to model the injection profile and the current crowding phenomenon, in the hope of finding a better design paradigm that can somewhat relax the aforementioned tradeoff.

6.6.1 Modeling the current profile

In this section, we present a simple model consisting of only two diodes that can help us develop some intuition into the observed behavior. In this model, the left (or right) half of the device is divided into a central and an outer region, each modeled by a discrete diode, as shown below.

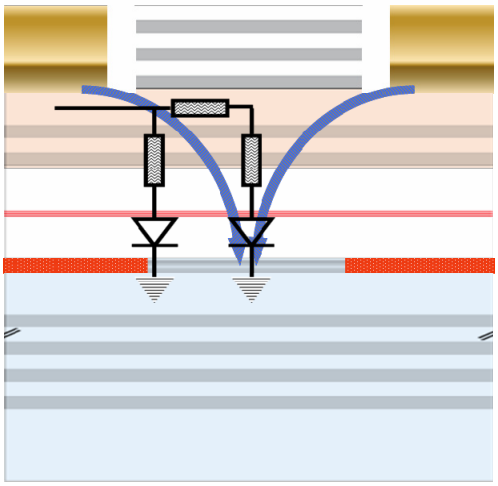

Figure 6.16: An illustration of the optimal current distribution, as well as the equivalent two-diode model for the spreading layer.

It is enlightening to study the ratio between the current in the outer and central branches of the above figure:

$$\ln(x) = -\frac{((R+r/2)x - r/2)I_1}{kT/q}, \text{where } x = \frac{I_2}{I_1}$$

$$I = -\frac{kT/q(1+x)\ln(x)}{((R+r/2)x - r/2)}, \text{ so if } I \to \infty, x \to \frac{r}{2R+r}$$

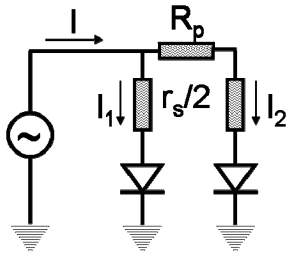

This formula implies that most of the current will flow in the first diode unless the downward resistance is at least comparable to the distribution resistance. This is an immensely important result, providing an alternative design approach that can optimize both the optical loss and the current distribution profile. The downward resistance can be increased by insertion of a low-doped layer, an abrupt potential barrier, or a combination of the two to balance the spreading resistance.

6.6.2 Series resistance and waveguide loss

Although such balancing of the lateral and downward resistances greatly improves the current profile, it can severely compromise total resistance in series with these lasers. This resistance should be kept at a reasonable value to minimize heating and allow continuous-wave operation. Moreover, free-carrier-absorption loss due to dopants should also be minimized in order to improve the threshold and quantum

efficiency. Unfortunately, the required doping levels in a balanced current spreading layer in p-type GaAs can be prohibitively large, which in turn may result in unacceptable levels of optical loss in these systems. To further shed light on this issue, we try to look at the doping dependence of the series resistance and the optical loss of a balanced p-DBR mirror. It is worthwhile to note that:

$$\alpha_{ARROW} \propto p, \text{ whereas } R_{series} \propto 1/p$$

where p stands for the density of p-type dopants in the material. Since mobility of holes in AlGaAs material significantly degrades at higher doping levels and aluminum concentrations, this tradeoff guarantees suboptimal performance of p-type mirrors; although composition and dopant engineering can slightly improve this tradeoff.

The electron mobility in GaAs, on the other hand, is drastically higher than holes[50,51], around ~3000cm^2/Vs at 10^{18}cm^{-3} compared to ~150cm^2/Vs for the same concentration of p-type dopants, which further reduces to ~30cm^2/Vs at higher doping concentrations ~3x10^{19}cm^{-3}. Moreover, the free-carrier absorption loss due to electrons is about half that for holes. Therefore, a much better approach involves use of an n-type mirror as the distribution layer. This can be done by adding a thin tunnel junction on top of the first p-region[52], to allow growth of high-mobility n-DBR mirrors instead of p-DBRs. In a tunnel junction, the doping levels at the p-n interface are so large that the carriers can easily tunnel through the potential barrier into the other side. This junction therefore acts like a resistor. Another approach, which is exploited in the second generation of fiber-coupled lasers here, involves growth on p-type GaAs substrates.

6.6.3 P-type vs. N-type substrates

Traditionally, most GaAs-based devices have been grown on n-type substrates. This has been partly due to the unavailability of high quality p-type substrates and dopant sources. These substrates are nonetheless highly advantageous in many applications, and the advent of quality carbon sources for both MBE and MOVPE has significantly improved the quality and reliability of p-type GaAs epitaxy. Moreover, major advances in the bandgap and dopant engineering of p-type DBR mirrors have

resulted in low-resistivity mirrors that can even surpass the n-type equivalents[53]. Although such a compositional grading is only possible in MOVPE, high performance step-graded[54] MBE mirrors have also been reported in the literature. The details of the DBR design for the second generation lasers, along with some simulations of the grading structure are presented in Appendix B.

6.6.4 Spontaneous emission spectrum

The spontaneous emission power generated in the plane of the quantum wells is proportional to the square of the carrier density: $R_{SE} \propto N^2 \propto J$

Mapping the spontaneous emission profile with a proper CCD camera is therefore a powerful instrument that can help quantify many electrical parameters of the device. This technique is used extensively in this project to assess current distribution patterns in the top DBR mirrors. For instance, the poor electrical behavior of the first generation lasers is indeed evident in the mapped spontaneous emission profile of Figure 6.11.

6.6.5 Medici simulations

Medici is a powerful device simulator that can be used to model the current profile of these devices. In the following figures we try to compare Medici simulations of the current density profile in an unbalanced and a high downward resistance p-region of a simple GaAs p-i-n diode. The *p*, *i*, and *n* regions are 0.7, 0.3, and 0.5µm thick respectively. The *p*- and *n*- doping levels are $3x10^{19}$ and $10^{18}cm^{-3}$, respectively.

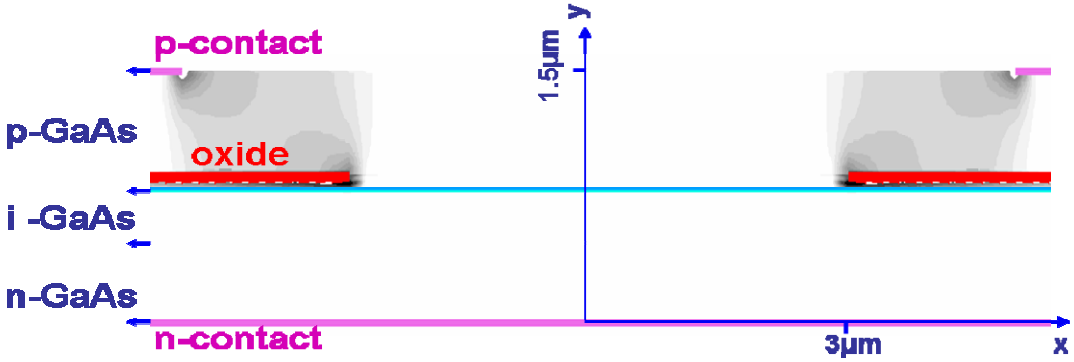

Figure 6.17: Medici simulation of the ARROW current profile at 3.5 $kAcm^{-2}$ (1.4V), for an ARROW with no spreading layers (uniform GaAs p-i-n diode).

As shown in the previous figure, the current in an unbalanced p-doped region mostly crowds around the edges of the oxide aperture. On the other hand, insertion of a thin 100nm low-doped ($5x10^{17}cm^{-3}$) $Al_{0.5}Ga_{0.5}As$ region above the oxide aperture layer (Figure 6.18 below) in the previous structure helps distribute the current more evenly over the aperture, as it introduces a significant potential barrier for holes in the vertical direction resulting in significant lateral spreading.

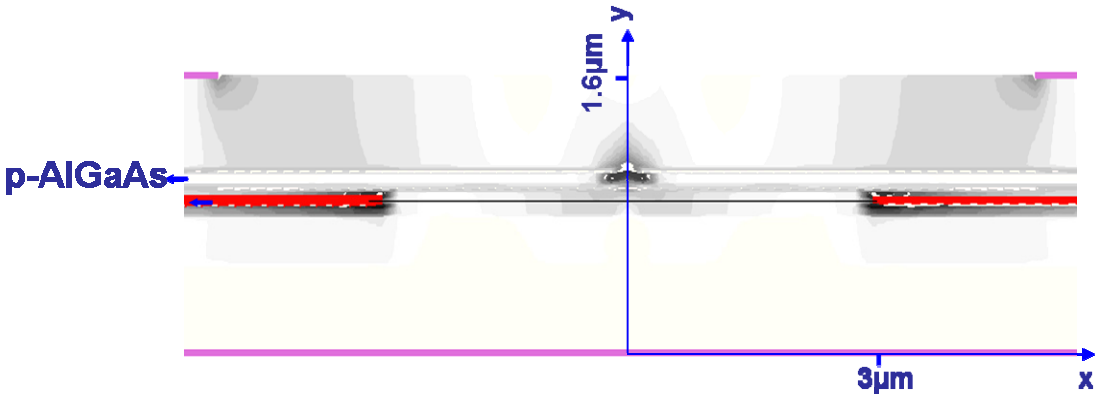

Figure 6.18: Medici simulation of the ARROW current profile at 800 Acm^{-2} (1.4V), for an ARROW with a 1000Å $Al_{0.50}Ga_{0.50}As$ spreading layer inserted before the oxide layer of the previous design.

These figures further validate the previously developed theory and reaffirm our previous conclusion that adjusting the downward resistance is indeed a critical requirement to produce a uniform gain medium in these lasers.

6.7 Second generation lasers

The epitaxial structure of the second generation ARROWs is comprised of a p-i-n diode waveguide structure that includes a 33-pair, graded C/Be:AlGaAs bottom DBR, an intrinsic active region, a thin 200Å oxide aperture layer, and a 5-pair upper Si:AlGaAs DBR. A cross-section SEM micrograph of the epitaxial structure is depicted in Figure 6.19. Details of the layer structure including the compositional and doping profiles can be found in appendix B.

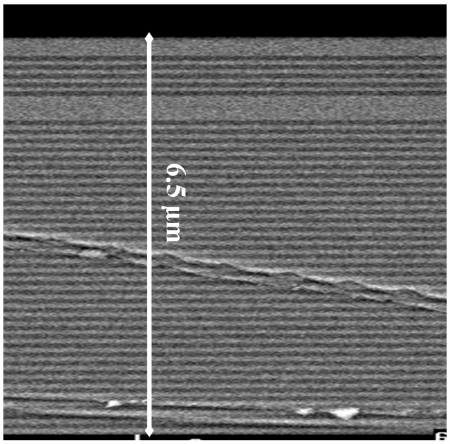

Figure 6.19: A SEM micrograph of a second-generation ARROW epitaxial structure.

Six 80Å GaAs quantum wells in the center cavity provide enough gain to overcome various sources of scattering and material loss in our system. The quantum wells are placed at the maxima of the modal electric field in the center cavity, to enhance the confinement factor (Γ). However, placing all six QWs close to each other significantly reduces the confinement factor for the lateral wells. The wells are therefore divided into two groups and placed at separate electric field maxima in a third-order cavity. The electric field intensity profile of the fundamental mode of a rib ARROW fabricated on this wafer is depicted in Figure 6.20.

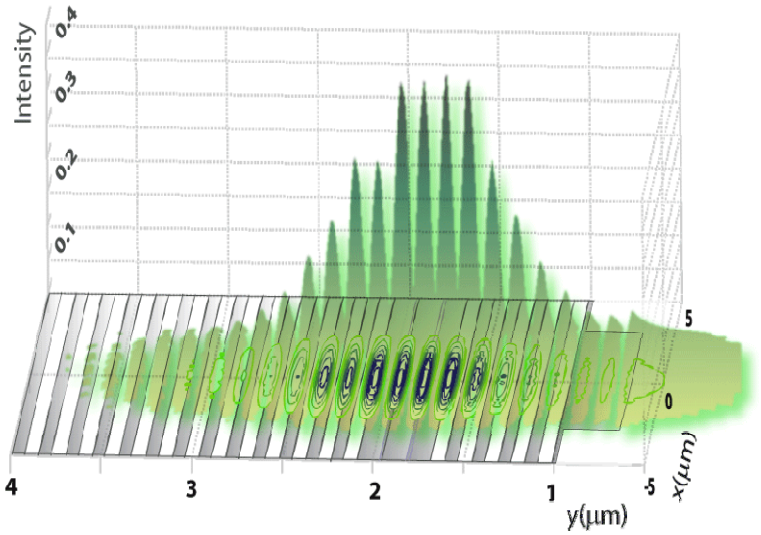

Figure 6.20: Electric field intensity distribution of the fundamental mode of the ARROW of Figure 6.19. Outline of the epitaxial structure is shown in the x-y plane.

Like the early devices, the fabrication process of these ARROWs includes two monitored dry etches, oxidation and silicon nitride passivation steps, as well as multiple angled evaporations for contact and interconnect metallizations. Details of the fabrication process are discussed in appendix A. Figure 6.21 depicts a scanning electron micrograph of the fully processed ARROW.

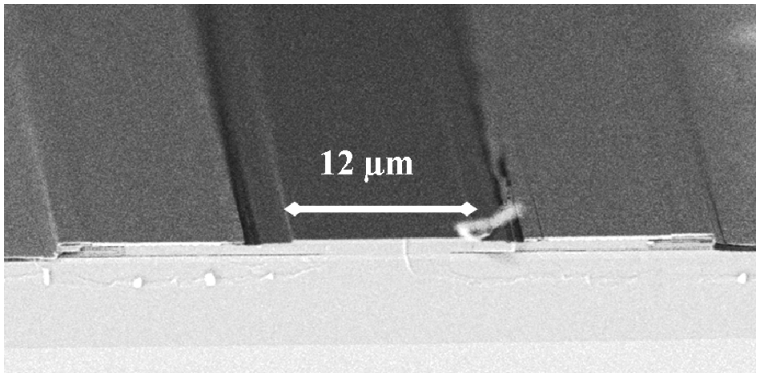

Figure 6.21: An SEM image of a fully-processed ARROW.

Following the device fabrication, the waveguides are brought into contact with the 5/125μm singlemode fiber for coupling experiments.

6.7.1 Features

The new design has many advantages over previous devices. Here we discuss important features of these lasers and compare them to the old structures.

6.7.1.1 Current Spreading

The new design employs DBR composition and doping engineering to reduce the optical loss whilst balancing the lateral and downward resisitivity, for an optimal current spreading profile. P-type GaAs substrates are used so that high-mobility n-type mirrors are grown on top, drastically improving the current-distribution profile and the optical losses compared to prior samples on n-type substrates. A special low-doped n-DBR pair is placed close to the cavity to provide a potential barrier for the electrons flowing into the active region, thereby improving their lateral spreading. The DBR design in this structure is very involved and requires extensive analysis and simulations to achieve optimal electrical and optical performance. Further details of

the DBR design will follow in appendix B. The total series resistance of the device, including the contact and p-DBR resistance, is measured ~$2x10^{-4}$ Ωcm^2. Unlike the old devices (Figure 6.11), the spontaneous emission profile, shown in Figure 6.22, is very uniform here, indicating that the current is distributed evenly across the waveguide.

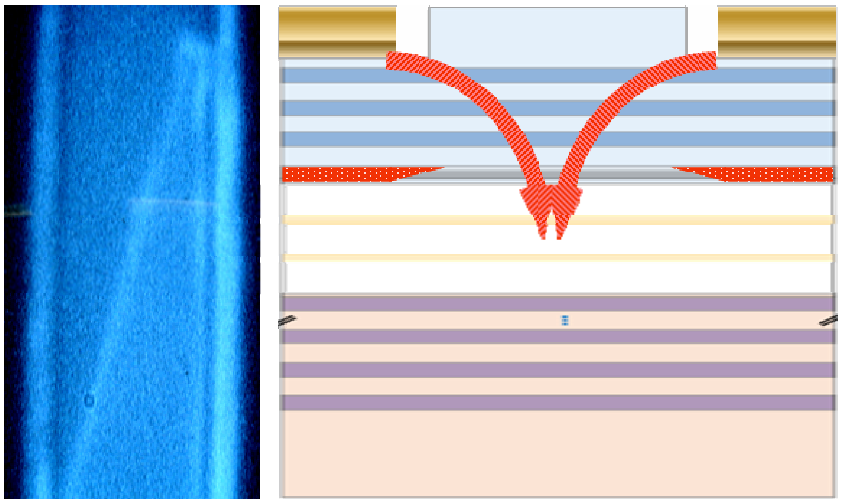

Figure 6.22: CCD image of the spontaneous emission off the QWs in a second-generation ARROW. An illustration of the current distribution profile is shown on the right.

Since the low-mobility p-region in this implementation sits adjacent to the thermo-electric cooler, the thermal characteristics of the system are also improved compared to the previous devices, making this architecture even more attractive for high-power applications.

6.7.1.2 Waveguide loss

In the new ARROW design, the mesas are entirely formed in the 5λ/4 top layer. This will result in considerably less sidewall roughness compared to the old devices where the high aluminum-content material was exposed and oxidized at the waveguide boundaries as shown in Figure 6.23 below. We therefore expect the scattering losses of these devices to be very small.

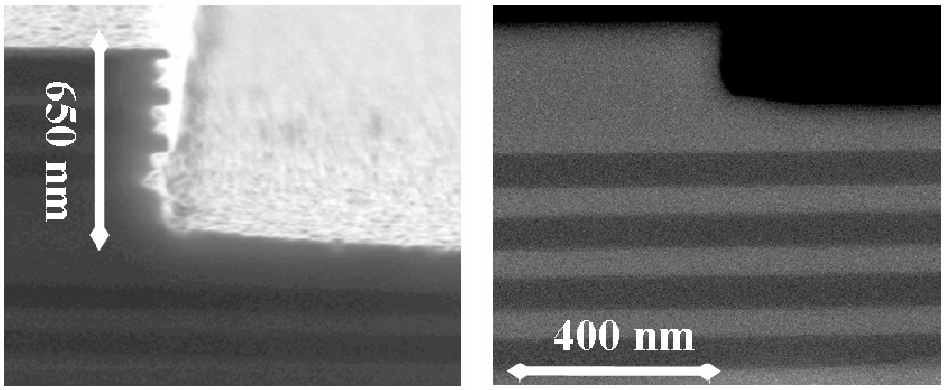

Figure 6.23:Comparison between the ridge sidewalls of the old (left) and new (right) ARROWs.

Moreover, free carrier absorption is reduced drastically in this design, as the dopant density is minimized in the vicinity of the cavity. Growing on a p-substrate is again highly advantageous, because a low-resistance balanced top mirror can be realized in a thin low-doped AlGaAs n-DBR. Such low concentrations of electrons only add minimal loss to the waveguide. On the other hand, such a mirror realized in the p-type material would necessitate prohibitively high doping levels, severely increasing the optical loss of the system. With the present design, total material losses in the system are calculated to be around $20cm^{-1}$, which is considerably better than the earlier devices which had optical loss of $\sim 200cm^{-1}$.

6.7.1.3 Oxide aperture

The oxide aperture in the new design is placed on top of the cavity to effectively force the injected carriers to flow to the center of the waveguide. Placement of the current aperture under the cavity in the old design was partly responsible for the low carrier densities observed at the waveguide center. Figure 6.24 compares the current apertures in the two designs. Moreover, the oxide aperture here is designed to have a tapered front to further minimize the scattering loss at the antinode of the electric field. The width of the aperture is also of great concern. While the oxide front is typically extended into the waveguide to induce some scattering loss for higher order axial modes, it also adds loss to the fundamental mode.

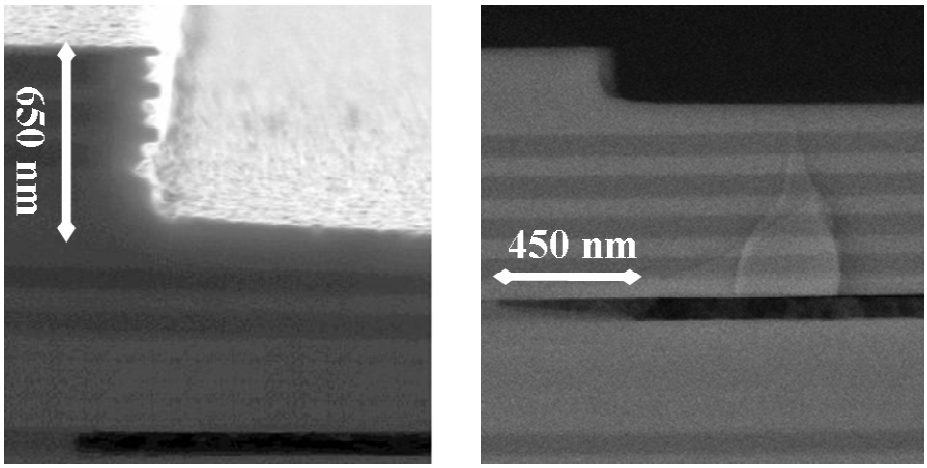

Figure 6.24: Comparison between the oxide fronts and their locations in the old (left) and new (right) ARROWs.

6.7.1.4 System design

The lithography masks were also redesigned to ensure that the evanescent coupling between the fiber and the waveguides was optimal and the deposited metal surfaces do not grow beyond the top ARROW surfaces. Since the probe tip sits about 2mm away from the waveguides (because of the wide fiber block), the metal layer thickness is limited to the ridge height in the current process; a long and wide interconnect is necessary. Nevertheless, a separate interconnect deposition process, along with a thicker (7λ/4 or higher) top layer can completely resolve this issue. Moreover, a hand polishing technique was developed to adjust the fiber polish-depth, in order to enhance the coupling and improve on the system performance.

6.7.2 Discussion

Despite all the measures taken in the design phase, several nonidealities present in our test setup gave rise to finite air gaps in the coupling medium. The air gaps severely limit the coupling strength, measured quantum efficiency and output power as described before. This is, however, a process-induced limitation, and can be overcome if the manual substrate alignment here is replaced with a more robust bonding procedure that assures optimal contact between the fiber and the waveguide. With further improvement in the fabrication process, such as optimization of the

aperture width and the waveguide thicknesses, as well as elimination of the air-gap in a robust bonding process, these lasers can produce a far more powerful output that can even be used to pump other lasers. Moreover, with better interconnects, these lasers are expected to perform as well in the continuous-wave regime.

6.7.3 Results

The ARROWs are pumped by a pulsed current source, at a pulse width of 0.5 μs and a 1 kHz repetition rate, to provide gain in the quantum wells without generating too much heat. Although the active region of these waveguide lasers can withstand large continuous-wave (CW) currents, thermal failure of thin interconnects limits the CW operation, since most of the 10Ω series resistance of this laser drops across these interconnects. Figure 6.25 depicts the L-I-V curve of a hybrid 10x1000μm ARROW/fiber system.

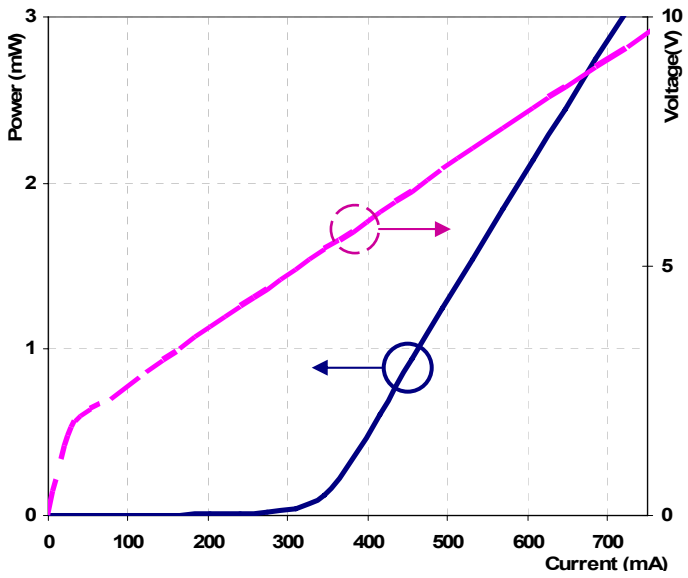

Figure 6.25: The L-I-V curves of a second generation ARROW-fiber laser.

The measurement shows more than 3mW of power coupling into the singlemode fiber. Depending on the coupling strength, the lasing threshold in these devices varies from 200-400mA (~0.3-0.6 kA/cm^2/QW). Figure 6.26 shows the normalized power spectrum of this device at 600mA. The spectrum does not show significant spurs and a side-mode suppression ratio of at least 27dB is easily achieved.

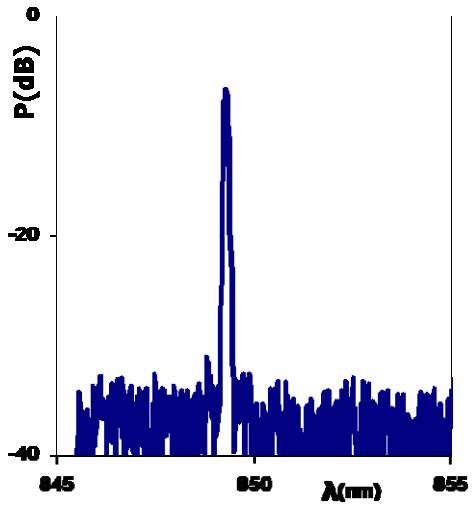

Figure 6.26: High resolution emission spectrum of the ARROW-fiber laser at 600mA. Power reference is arbitrary.

The SSR is mainly limited by the resolution of the spectrum analyzer. The spectrum of another device is depicted in Figure 6.27. Here the measured SSR is around 35dB, but the lasing linewidth appears wider since the OSA resolution has been changed.

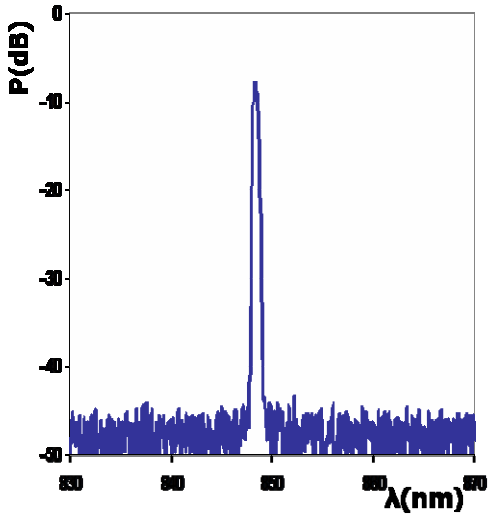

Figure 6.27: Low resolution emission spectrum of the ARROW-fiber laser at 600mA. Power reference is arbitrary.

Unlike simple edge emitters, the lasing wavelength is highly stable and merely depends on the material refraction indices, resulting in minimal variations with

temperature. The measured temperature dependence of the lasing wavelength is around 0.06nm/ºC, which corresponds to the known AlGaAs index change of about $2x10^{-4}$/ºC.

6.8 Amplifier-based hybrid lasers

Another architecture that can be used for hybrid lasing is based on the amplifier design of the chapter 5. Here, both mirrors are implemented in the fiber. Since one of the mirrors is used as the output coupler, previously described metal coating cannot be implemented. A fiber Bragg grating or a dielectric coated tip can be used instead to realize this partial reflector. Figure 6.28 depicts this architecture in more detail.

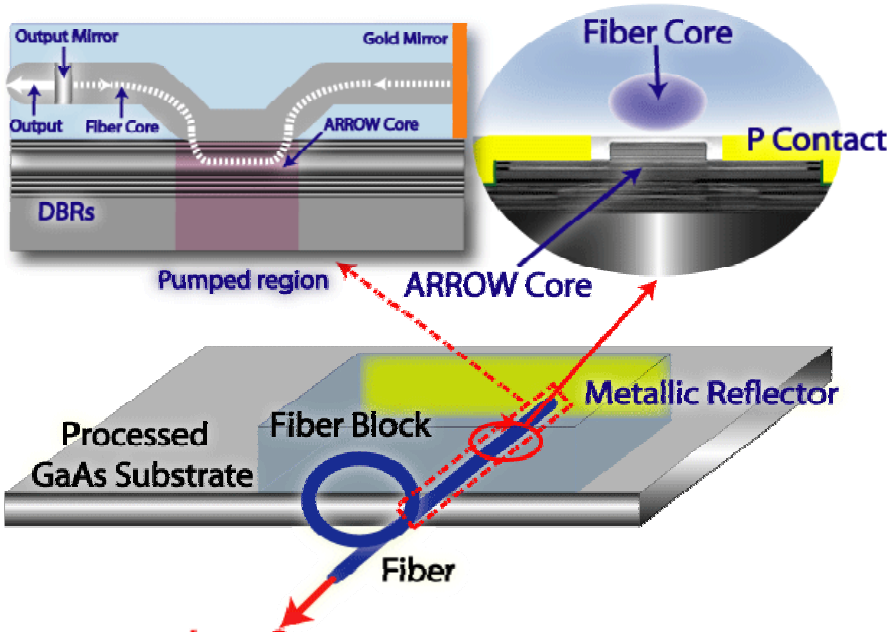

Figure 6.28: A hybrid laser based on the ARROW-fiber amplifier of the previous chapter.

This design is much less efficient because the bouncing mode has to travel inside the cavity and back into the fiber in a single path, severely degrading $\eta_{coupling}$ and the efficiency of these lasers. Nevertheless, this design does not need a cleaved semiconductor facet and can therefore be attractive in some applications. Moreover, the output coupler can be adjusted independently of the coupling characteristics, which was the main limiting factor in the previous design.

6.9 High efficiency architecture

The coupling-induced efficiency limitation of the current structure ($\eta_{coupling}$) can be tackled effectively if we somehow decouple the coupling and gain regions of these lasers. This idea is illustrated in Figure 6.29 below.

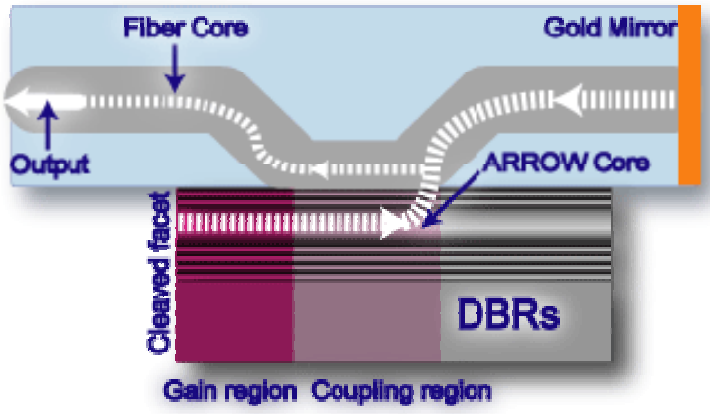

Figure 6.29: High-efficiency hybrid laser design with separate gain and coupling regions.

The coupling region is completely separated, *e.g.* by proton implantation, from the rest of the semiconductor, and is pumped lightly to the transparency level to compensate for the small ARROW loss. The length of this region is chosen to optimize the output coupling of this laser. The fiber should be shielded form the waveguide away from this region and the coupling should take place merely over this interaction area. Since most of the energy in the hybrid mode is transferred into the semiconductor over the coupling region, the heavily-pumped gain area overlaps perfectly with the hybrid mode ($\eta_{coupling} \rightarrow 1$) and the efficiency significantly improves. The efficiency formula for this structure is simply:

$$\eta_d = \frac{\eta_{leakage}\,\eta_i \cdot \alpha_{output}}{\sum \alpha_{loss}}$$

This structure is therefore expected to achieve quantum efficiencies comparable with the edge emitters, as the longitudinal overlap between the gain and the mode is optimized. Since a coupling length of ~200μm is easily achieved in this technology, the threshold power penalty due to the slight pumping of this coupling area is minimal. Moreover, the coupling can be changed significantly by tuning the

current, providing an additional adjustment knob that can be used for modulation or tuning of such lasers. This structure is nonetheless hard to realize in the manual alignment setup and use of a flip-chip bonding process is required.

As another interesting application, a part of the gain region could be used as a saturable absorber to facilitate mode-locking in this laser. Such a design requires a large coupling bandwidth, which could be achieved by a growth taper.

Chapter 7

Conclusions

7.1 Summary

In this thesis, we presented a novel hybrid fiber semiconductor topology that is capable of producing high quality lasers for telecommunication applications. The side-coupling approach adopted in this project is especially attractive because it can potentially replace the cumbersome free space alignment and packaging processes by a far more robust, misalignment-tolerant wafer-bonding technique that avoids the costly fabrication procedures of the foregoing butt-coupled lasers. In addition to the low-cost device fabrication, these systems lase at a single frequency without any additional gratings, and have the advantage of array configurability and the possibility of integration with other semiconductor or fiber devices.

In the initial chapters, we developed the underlying theoretical frameworks for this project. A side-coupled light emitter with high efficiency was presented in chapter 4, while a few architectures for side-coupled amplifiers were proposed and discussed in chapter 5. While these hybrid amplifiers (like modulators or detectors of the previous work) have limited applicability due to the small bandwidth and high polarization sensitivity, the side-coupled semiconductor fiber lasers actually benefit from these features. Chapter 6 includes the bulk of this work on such lasers. While the first generation designs were the first demonstrated hybrid lasers of its kind, they had very limited efficiency. An extensive analysis of the efficiency limiting processes, such as loss mechanisms and current profiles, resulted in multiple orders of magnitude improvement in the performance of second generation lasers. Finally, the details of the fabrication process as well as a brief discussion of the epitaxial design are presented in appendices A, and B.

7.2 Suggestions for future work

Although the devices presented in this thesis are proof-of-concept demonstrations, we also discussed possible changes in the design and fabrication process that can significantly improve the performance of these systems. These include the optimization of the epitaxial design (e.g. by using tunnel junctions), number of the QWs, and the width of the oxide aperture. We also presented some new designs for other applications like tunable, mode-locked, or high-power lasers. An interesting extension to these hybrid devices includes integration of a side-coupled modulator or an amplifier with our lasers, to generate a modulated or amplified signal in a small form-factor package.

Finally, it is important to note that by applying the same design methodology, the designs presented here can be readily applied to other material systems, such as the GaInNAsSb/GaAs system, in order to cover longer telecommunications wavelengths. This could drastically reduce the cost and complexity of commercial telecom fiber laser modules.

Appendix 1

The ARROW fabrication process

In this appendix we will review the fabrication procedure of ridge ARROW waveguides for the first and second generations of active fiber-coupled semiconductor modules.

A.1 The original process flow

The initial devices were all grown by metal-organic vapor phase epitaxy (MOVPE) on n-type GaAs substrates and were fabricated using four lithography masks. All lithography steps are carried out by a standard KarlSuss MA-6 Contact Aligner. An alignment accuracy of better than 1μm is consistently achieved with this system. Most fabrication steps are followed by a wet cleaning etch in a NH_4OH:H_2O 1:9 solution and a brief oxygen etch in a Drytek 100 Plasma Etcher to reduce the roughness and clean the surfaces from photoresists and other contaminations.

A.1.1 Epitaxy

The fabrication sequence begins by the MOVPE growth of the ARROW structure on a GaAs substrate. In an MOVPE reactor, semiconductor materials can be grown from the pyrolysis of organic compounds that contain the required chemical elements of the semiconductor. In molecular beam epitaxy (MBE) reactors, on the other hand, ultra-high purity elements are evaporated into atomic forms in ultra-high vacuums and are condensed on the wafer forming desired alloys. Most GaAs and InP laser are currently grown by MOVPE. Major advantages of MOVPE include low defect density, high quality regrowth capability, and compositional gradings, which

are not easily feasible in MBE reactors. Nevertheless, MBE is preferred for some compound alloys, like GaInNAs, where MOVPE technology is not quite mature.

The layer stack is typically comprised of a p-i-n diode waveguide structure that includes 30-35 pairs of graded Si:$Al_{.95}Ga_{.05}As$-$Al_{.20}Ga_{.80}As$ bottom DBR, an oxide aperture layer, an intrinsic active region containing few quantum wells. The 5-pair upper $Al_{.80}Ga_{.20}As$-$Al_{.20}Ga_{.80}As$ DBR is partitioned into two segments. A 2-pair p-doped material is grown adjacent to the cavity (including a 5λ/4 p-contact layer) to provide a pad for p-contacts and improve the current profile. Another 3-pair undoped DBR is grown on top to define the ARROW etching region without introducing extra loss. The typical grown structure is depicted in Figure A.1.

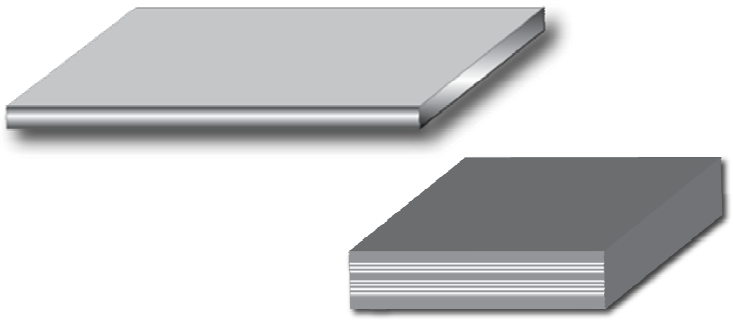

Figure A.1: Illustrations of an epitaxially grown ARROW wafer (Close-up view on the right).

A.1.2 First dry etch

The first fabrication step is a standard dry-etch that cuts through the cavity and stops right under the oxide aperture layer to define the larger mesas used for metallization. Underneath the oxide aperture lies a 3λ/4 layer that provides a thick etch stop layer to relax the timing accuracy of this etch process. This etch is done in a PlasmaQuest ECR GaAs etcher with a HeNe monitor laser that is used to effectively control the etch progress. The reflectivity is simulated in the TRC software and compared to the monitored plot to track the etching and identify the stop points. This etch step is illustrated in Figure A.2.

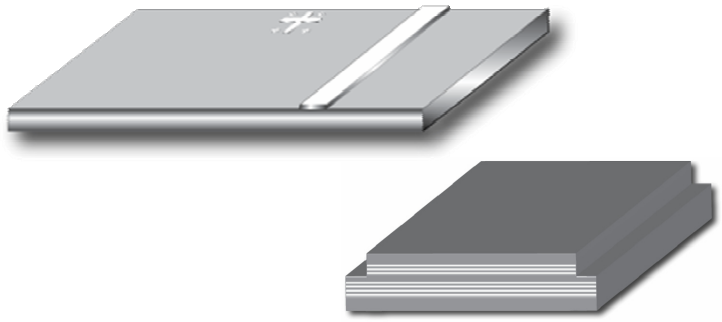

Figure A.2: Illustrations of the first etch process for defining larger mesas on the grown ARROW wafer.

A.1.3 Second dry etch

After resist stripping and other cleaning procedures, the substrate is patterned with the waveguide mask and dry-etched to realize the ridge ARROW in the center. This step immediately follows the first etch, with its etch time calculated directly from the reflectivity plots of the previous process. This defines the ridge ARROW waveguide and exposes the P-doped contact layer, which is used as a pad for contacts, as shown in Figure A.3. To improve sidewall profile, the patterned photoresist is briefly etched in an oxygen plasma prior to this waveguide definition process.

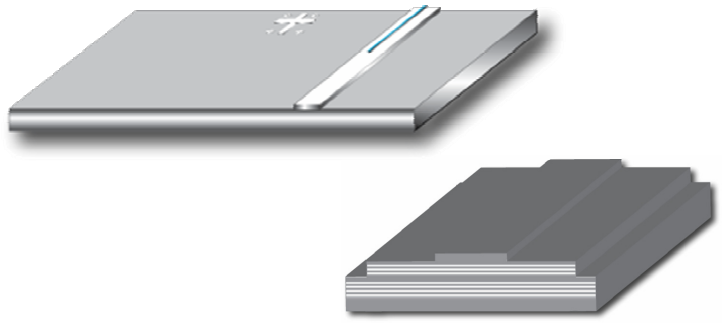

Figure A.3: Illustrations of the second etch process for defining the ridge waveguides on the grown ARROW wafer.

A.1.4 Oxidation

An $Al_{.98}Ga_{.02}As$ layer is grown right under the cavity to provide a current aperture to confine the carriers to the center region of the waveguide. The etch rate of $Al_xGa_{1-x}As$ is a strong function of the Al concentration and decreases very rapidly as

the Ga-percentage increases[55]. The typical oxidation selectivity of the $Al_{.98}Ga_{.02}As$:$Al_{.95}Ga_{.05}As$:$Al_{.80}Ga_{.20}As$ materials used in this process is roughly 35:.10:1, and the oxidation rate of the $Al_{.20}Ga_{.80}As$ material is negligible.

Oxidation is carried out in a hot steam-saturated, N_2 ambient furnace. The ambient and the water temperature are set at 440ºC, and 90ºC respectively. One or two calibration runs are typically done before each oxidation step to carefully adjust the extent of the oxide. The current aperture may slightly penetrate into the ARROW waveguide to provide better confinement and to introduce selective loss to the higher order transverse modes. The small oxidation of the top $Al_{.80}Ga_{.20}As$ waveguide walls is a side effect of this process and increases the scattering losses of the waveguide. This issue is solved in the second generation designs which follow at the end of this appendix.

A.1.5 Passivation

The preceding etch steps expose both the p-doped and n-doped regions of the device. Without an additional isolation layer however, the contacts cannot be evaporated on the devices for they will short the n-and p-regions of the laser diode.

To passivate our devices and isolate the n-doped regions, a thin (~500Å) silicon nitride layer is deposited and patterned on the wafer through chemical deposition and lithography. This Si_3N_4 deposition is carried out in an STS PECVD System at 350ºC. Figure A.4 illustrates this passivation step. Si_3N_4 is later patterned by a brief 1.5min SF_6 etch in the Drytek 100 Plasma Etcher to remove the isolation layer over the waveguide and contact areas.

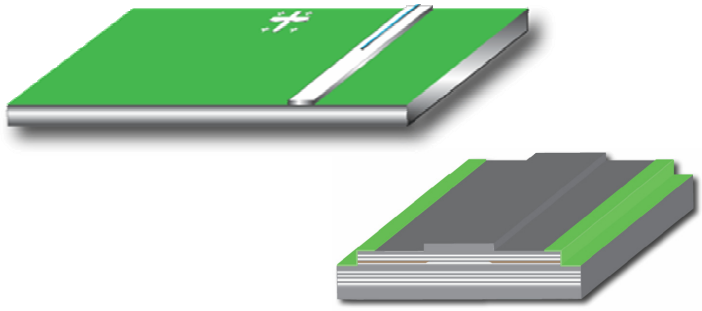

Figure A.4: Illustrations of the Si_3N_4 passivation step on the grown ARROW wafer.

A.1.6 Metallization

Before Si_3N_4 etching, the n metal stack Ge/Au/Ge/Au/Ni/Au is evaporated on the back of the GaAs wafer. The wafer is then annealed at 425ºC for 1min to provide low resisitivity contacts to our devices. A 1min $NH_4OH:H_2O$ 1:9 dip is necessary before each evaporation process in order to rid of surface oxides. Optionally, the wafer can be thinned prior to the n contact deposition to improve heat sinking and thermal performance.

Finally, the p-contact Ti/Au lift-off process is carried out to make contacts to the individual waveguides and interconnect these devices to the electrical probe pads. Since sidewall coverage is critical, a simple evaporation process will not be sufficient. A low-temperature sputtering is ideal, but it was not available at the time these devices were made. Instead, multiple angled evaporations are used to cover the sidewalls and reduce the interconnect resistance. Since the total metal thickness (plus the Si_3N_4 layer) should not exceed the waveguide etch depth, the total sheet resistance of the metal stack can be very small. We therefore have to use wide (~200µm) pads to reduce the series resistance of the interconnects. The final device is depicted in Figure A.5. Following the fabrication process, the wafer is cleaved into small pieces to prepare for fiber-coupling in our test setup.

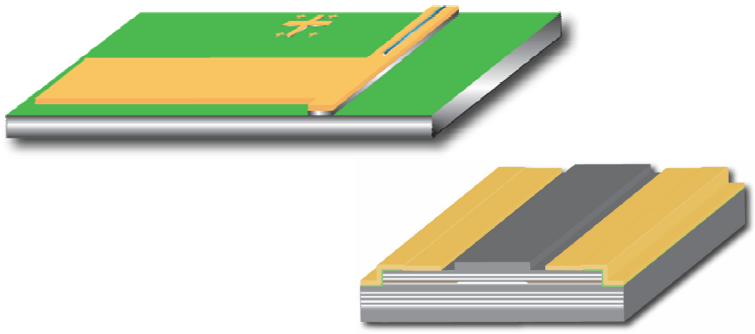

Figure A.5: Illustrations of the top-side metallization process on the grown ARROW wafer (fine view on the right)

A.2 The modified process flow

The bulk of the fabrication process for the second generation devices is the same as before, with few changes made to the process flow to accommodate reversed substrate doping, and to improve the current profile and optical loss of the system. These devices were all grown on p-type GaAs substrates for better current distribution profile over the active region.

A.2.1 Epitaxy

As mentioned before, molecular beam epitaxy (MBE) was used to grow the structures as MOVPE services were not available at the time. The layer stack is comprised of a p-i-n diode structure that includes a 33-pair, graded C/Be-doped $Al_{.91}Ga_{.09}As/Al_{.20}Ga_{.80}As$ bottom DBR, an intrinsic $Al_{.20}Ga_{.80}As$ active region, a tapered-tip oxide aperture layer, and a 5-pair upper Si-doped $Al_{.91}Ga_{.09}As/Al_{.20}Ga_{.80}As$ DBR. The top layer is comprised of a $5\lambda/4$ n-doped $Al_{.20}Ga_{.80}As$ material that acts as the p-contact and the etched rib layer. Three to six GaAs quantum wells (80Å) are placed in the center cavity to provide enough gain to overcome various sources of scattering and material loss in our system. The layer structure is depicted in Figure 6.19.

A.2.2 Dry Etches

The etching is done in two rounds as described before. The only difference is that the first etch here does not penetrate the n-region and stops in the cavity below the oxide layer. Moreover, the waveguide etch is limited to the top $5\lambda/4$ $Al_{.20}Ga_{.80}As$ layer to reduce the oxidation at the sidewalls of the ARROW. The allowed metal thickness is therefore small and interconnect resisitivity is larger than before.

A.2.3 Oxide aperture

To improve carrier confinement and reduce optical loss, the oxide aperture is grown on top of the cavity and is designed to have a tapered front. To achieve this, a thin $Al_{.98}Ga_{.02}As$ is grown atop of the first $Al_{.91}Ga_{.09}As$ layer, where the modal field is

minimal. As a result this DBR layer oxidizes with a fast rate and with a tapered front, which is easily seen in Figure 6.24.

A.2.4 Metallization

The n- and p-contacts are switched in the current device, but more or less follow the same flow as before. The n-stack is somewhat problematic as it may not stick well to the silicon nitride layer. This can be fixed if a thin Ti-layer is deposited on top of the nitride and the passivation etch is done in an HF solution.

Appendix B

Design of ARROW epitaxial structures

This appendix serves as a brief overview of the DBR design in second generation lasers. Since compositional grading is not available in MBE systems, low-doped low-resistivity p-DBR growth is very challenging. Moreover, to attain optimal current profile in the top DBR, thorough knowledge of the n-DBR downward resistance is required. In this chapter we study the resistivity and loss of the MBE-grown DBRs and present simulation data to validate our designs.

B.1 P-type DBRs

The p-DBR design, in particular, is very complicated and requires a detailed analysis as loss-resistivity tradeoff is most severe in p-type heterojunctions. The free-carrier absorption loss of holes can easily dominate the ARROW loss, so it is critical to keep its contribution small. On the other hand, the interface resistivity increases significantly at low doping levels. It is therefore essential to optimize the doping profile for best overall performance. More importantly, we need to study the compositional grading of the heterojunctions, as it can effectively relax the aforementioned tradeoff. Doping profile is analyzed afterwards in the next subsection. To achieve maximum doping flexibility, both carbon and beryllium sources are used in these p-DBR epitaxies.

B.1.1 Grading Profile

Complete analysis of heterojunction interfaces is beyond the scope of this writing, and the reader is referred to the literature for more details[56]. Although abrupt p-DBR interfaces are highly resistive due to sharp discontinuities at the valence band, compositional grading can significantly reduce this barrier and improve the interface conductivity. Such a grading can be easily achieved in MOVPE systems and the resulting p-DBRs are therefore very low resistance[23]. On the other hand, continuously graded junctions are impractical in MBE systems and such state-of-the-art p-mirrors cannot be achieved. Nevertheless, alternative grading techniques have been proposed for MBE systems and acceptable junction resistivities have been reported. Such methods include digital grading, step grading, and various interface doping profiles that all aim at improving the valence band profile at the interface. To reduce the number of shutter openings, we employ the following step-graded junctions in our p-DBRs:

Layers	*High index DBR*	*Grading layer 1*	*Grading layer 2*	*Grading layer 3*	*Low index DBR*
Composition	$Al_{0.20}Ga_{0.80}As$	$Al_{0.42}Ga_{0.58}As$	$Al_{0.50}Ga_{0.50}As$	$Al_{0.72}Ga_{0.28}As$	$Al_{0.91}Ga_{0.09}As$
Sources	$Ga_{1,2},Al_2$	$Ga_{1,2},Al_1$	$Ga_{1,2},Al_{1,2}$	Ga_2,Al_2	$Ga_2,Al_{1,2}$
Growth-rate (μm^{-1})	1.13	1.56	1.79	0.31	0.97
Thickness (Å)	487	72	49	79	586
Rel VB-offset (meV)	0	96	35	96	92
Index @ 850nm	3.4622	3.32	3.27	3.14	3.03

Table B.1: Interface compositional structure in the second generation MBE-grown p-DBRs.

The layer thicknesses are chosen to optimize the band diagram and reduce the overall potential barrier. While an increase in the overall grading thickness improves the resistivity, the mirror reflectivity deteriorates and additional DBR pairs may become necessary, in order to meet the reflectivity specifications. Here, a grading thickness of 200Å is used, hence 3 extra DBR pairs are added to counter the negative effect of junction grading on the reflectivity of the p-type mirror. The DBR thicknesses have to be modified to take the grading effects into account. Since the

intermediate alloys have different growth rates, dopant incorporation level varies significantly at the interface, unless doping sources are shuttered. Figure B.1 depicts Medici-simulated I-V curves of several graded and abrupt p-DBRs. It is clearly seen that step grading can significantly improve the junction resistivity. In this Figure A, G, and G- stand for abrupt, graded with variable-doping, and graded with uniform doping (shuttered) interfaces. Obviously, higher doping at the interface helps.

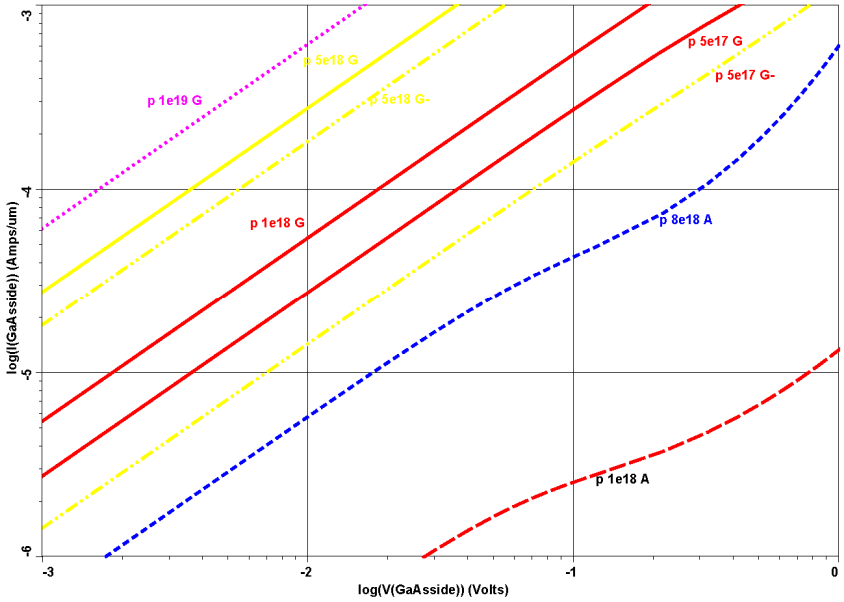

Figure B.1: Medici simulation of the I-V curves of various types of p-DBR structures.

B.1.2 Doping Profile

Since the modal electric field has a decaying envelope in the mirrors, the DBR layers adjacent to the cavity are most important and should have the least amount of doping. As we get farther from the cavity and move inside the mirror, the doping can increase, as these layers interact less with the electric field and their loss contribution is reduced. To model this effect we note that the modal intensity profile has an e^{-an} envelope in the DBR regions, as depicted in Figure B.2. n is the DBR number counting from the pair under the cavity.

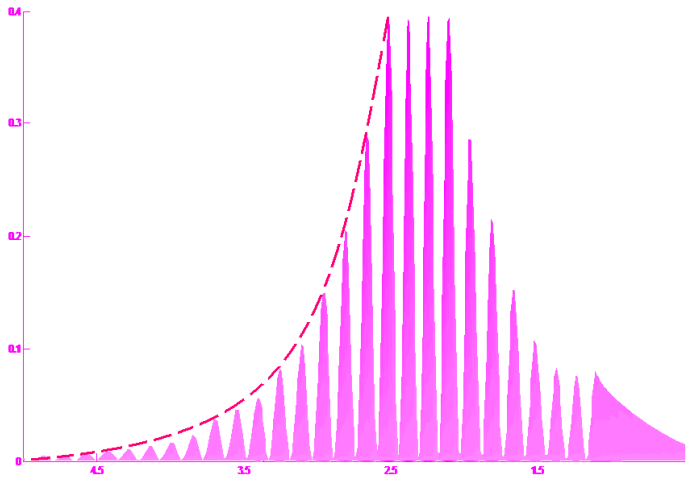

Figure B.2: ARROW vertical intensity profile with the exponentially decaying envelope.

Consequently, we can increase the doping exponentially (e^{+bn}) to take advantage of the reduced intensity in the farther DBR pairs. The overall contribution of this DBR to the waveguide loss becomes:

$$\sigma_{tot} = \frac{\int_{pDBR} EE^{*}\sigma(x)\,dx}{\int_{ARROW} EE^{*}\,dx} \approx \frac{\sum_{n} e^{-(a-b)n} \int_{n=1} EE^{*}\sigma(x)\,dx}{\int_{ARROW} EE^{*}\,dx}$$

where E stands for the modal electric field in the structure, and $\sigma(x)$ is the material absorption. Ideally we would choose $a \sim b$ to improve DBR conductivity, but growth rate variations can easily change a, so some margin is needed ($a>b$). Moreover, for acceptable growth quality, the doping cannot grow without bound and saturates after a few pairs, when $n>n_{sat}$. For the ARROW design of Figure 6.19 (second gen. lasers), the intensity decays roughly as $e^{-n/3}$, so the doping is designed to increase as $e^{+n/6}$ and saturate at ~10^{19}cm^{-3} after ~15 pairs. The first pair has a base doping of ~10^{18}cm^{-3}, and the interface doping is not shuttered (corresponding to the G-curves in the figure). The overall contribution of this DBR to the ARROW loss is therefore:

$$\sigma_{tot} < \frac{\sigma_1 \cdot \sum_{n} e^{-n/6}}{\sum_{n} e^{-n/3}} \cdot \Gamma_{pDBR} \approx 2\sigma_1 \Gamma_{pDBR}$$

where σ_1 is the total loss of the first DBR pair and Γ_{pDBR} stands for the portion of the modal electromagnetic power that penetrates this p-DBR:

$$\Gamma_{pDBR} = \frac{\int_{pDBR} EE^* dx}{\int_{ARROW} EE^* dx}$$

For this ARROW design, Γ_{pDBR} is around 0.3. Unfortunately, the interface resistivity is a more complicated function of doping. Furthermore, the compositional-grading profile at the junction strongly affects the overall conductivity of the interface. Nevertheless, over a limited range of doping levels and for a constant compositional grading profile, the doping-conductivity dependence can be approximated by a linear model. This is also evident in the Medici simulations of the Figure B.1 above. The overall resistivity is therefore:

$$\rho_{tot} = \sum_n \rho_n \approx \rho_0 \sum_{n<n_{sat}} e^{-n/6} + \rho_S \sum_{n>n_{sat}} 1 \approx 6.5\rho_0 + \rho_S (n_{tot} - n_{sat})$$

where ρ_{tot}, ρ_0, ρ_S stand for total, first DBR, and saturated DBR resistivities, respectively. From the Medici calculations of Figure B.1, we have ρ_0~2x10^{-6}, and ρ_S~2x10^{-7}. Therefore:

$$\rho_{tot} \approx 6.5 \times 2 \times 10^{-6} + 16 \times 2 \times 10^{-7} \approx 1.6 \times 10^{-5}\ \Omega\text{cm}^2$$

This value is nonetheless much smaller than the overall measured resistance of the ARROW structures (~2x10^{-4} Ωcm^2), which also includes contributions from the n-DBR and ohmic contacts. Aside from this doping envelope, the interface doping can significantly affect the resistivity and loss of the DBRs. Delta, dipole, and intensity-node doping schemes have been used[57] to improve the resistivity while adding minimal loss. These methods nevertheless require complex growth methods that may sacrifice the quality of the epitaxy. Here we only use elevated doping levels at the interface (G-curves in the Figure B.1) that arise normally from the reduced growth rate of the $Al_{0.72}Ga_{0.28}As$ layer to incorporate more doping at the interface.

B.2 N-type DBRs

Unlike p-DBRs, quality n-type mirrors can be grown easily in the MBE systems. This is due to the fact that the conduction band offset is maximum at

$Al_{.45}Ga_{.55}As$, therefore grading may even increase the effective barrier. Moreover, significant carrier tunneling can take place at moderate doping levels in abrupt n-type junctions. These mirrors are therefore low-resistance and low-loss, not only because the doping levels are not as high as p-mirrors, but also due to smaller free-carrier absorption coefficient of electrons. Nevertheless, the n-mirror design gets more complicated here, as balancing of the downward and lateral resistances in the top DBR becomes necessary. Figure B.3 compares the simulated I-V curves of the n-type mirrors with the aforementioned p-DBRs.

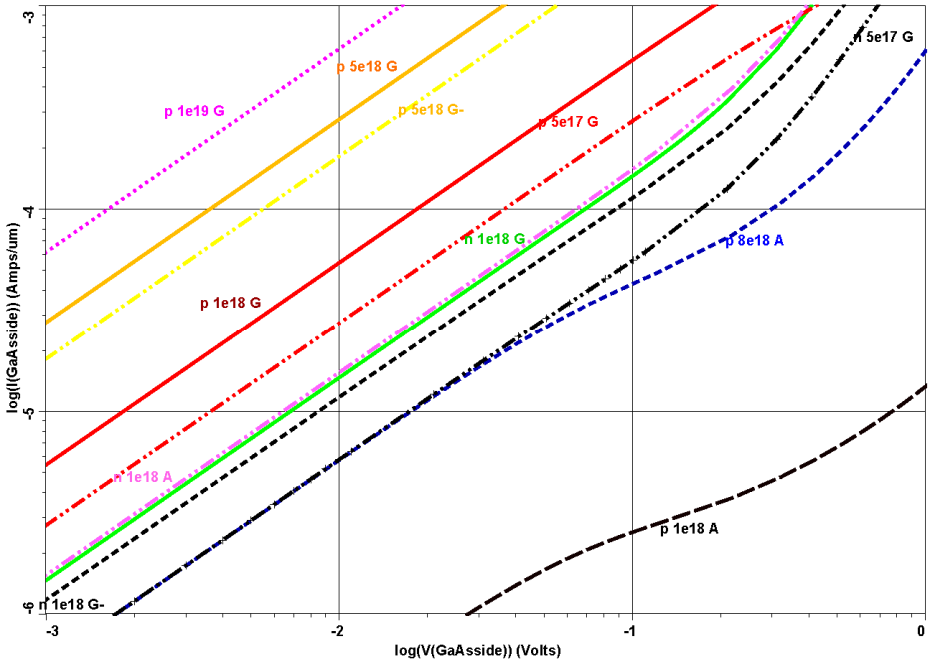

Figure B.3: Medici simulation of the I-V curves of various types of n-DBR (and p-DBR) structures.

In order to increase the downward resistance, we use low doping in conjunction with a step grade at the first DBR interfaces. The doping level is chosen to balance the spreading resistance of up to ~10 μm lateral distance in the top n-DBR. The top layers are doped higher (~$5x10^{18}cm^{-3}$) to make low-resistance n-contacts possible.

References

1 Nagarajan, R; Joyner, C; Schneider, R; et. al. “Large-Scale Photonic Integrated Circuits,” IEEE Journal of Selected Topics in Quantum Electronics; vol.11, no.1, p.50-65 (2005)

2 Suzuki, S; Sugita, A; “Recent progress in silica-based Planar Lightwave Circuits (PLCs),” NTT Technical Review; vol.3, no.7, p.12-16 (2005)

3 Ma, H; Jen, AKY; Dalton, LR “Polymer-based optical waveguides: Materials, processing, and devices,” Advanced Materials; vol.14, no.19, p.1339-1365 (2002)

4 Wooten EL; et. al. “Review of lithium niobate modulators for fiber-optic communications systems,” IEEE Journal of Selected Topics in Quantum Electronics; vol.6, no.1, p.69-82 (2000)

5 Sabnis, VA; Demir, HV; Yairi, MB; Harris, JS; Miller, DAB “High-speed optical switching based on diffusive conduction in an optical waveguide with surface-normal optical control,” Journal of Applied Physics; vol.95, no.5, p.2258-63 (2004)

6 McIntyre, PD; Snyder, AW “Power transfer between optical fibers,” Journal of the Optical Society of America; vol.63, no.12, p.1518-27 (1973)

7 Bergh, RA; Kotler, G; Shaw, HJ “ singlemode fibre optic directional coupler,” Electronic Letters; vol.16, no.7, p.260-261 (1980)

8 Takahashi, H; Suzuki, S; Nishi, I “Wavelength multiplexer based on SiO_2-Ta_2O_5 arrayed-wave-guide grating,” IEEE Journal of Lightwave Technology; vol.12, no.6, p.989-995 (1994)

9 Alferness, RC “Waveguide electrooptic modulators,” IEEE Transactions on Microwave Theory and Techniques; vol.30, no.8, p.1121-1137 (1982)

10 Duguay, MA; Kokubun, Y; Koch, TL; Pfieiffer, L “Antiresonant reflecting optical waveguides in SiO_2-Si multilayer structures,” Applied Physics Letters; vol.49, no.13 (1986)

11 Pezeshki, B; Agahi, F, Kash, JA “A gratingless Wavelength stabilized laser,” Applied Physics Letters; vol.69, no.19, p.2807-9 (1996)

12 Mao, E; Yankelevich, DR; Lin, CC; Solgaard, O; Knoesen, A; Harris, JS “Wavelength-selective semiconductor in-line fibre photodetectors,” Electronics Letters; vol.36, no.6, p.515-16 (2000)

13 Mao, E; Coldren, CW; Harris, JS; Yankelevich, DR; Solgaard, O; Knoesen, A “GaAs/AlGaAs multiple-quantum well in-line fiber intensity modulator,” Applied Physics Letters; vol.75, no.3, p.310-12 (1999)

14 Mao, E; Yankelevich, DR; Lin, CC; Solgaard, O; Knoesen, A; Harris, JS “Narrow-band light emission in semiconductor-fibre asymmetric waveguide coupler,” Electronics Letters; vol.36, no.16, p.1378-9 (2000)

15 Russell, P “Photonic crystal fibers,” Science; vol.299, no.5605, p.358-62 (2003)

16 See for instance: Pollock, CR "Fundamentals of Optoelectronics," © IRWIN Inc. (1995)

17 Scarmozzino, P; Gopinath, A; Pregla, R; Helfert, S "Numerical techniques for modeling guided-wave photonic devices," IEEE Journal of Selected Topics in Quantum Electronics; vol.6, no.1, p.150–162 (2000)

18 Stern, MS "Semivectorial polarized finite difference method for optical waveguides with arbitrary index profiles," IEE Proceedings J, vol.135, no.1, p.56–63 (1988)

19 See for instance: Chuang, SL "Phusics of Optoelectronics Devices," ©Wiley, Inc. (1995)

20 Yariv, A ''Coupled-mode theory for guided-wave optics,'' IEEE Journal of Quantum Electronics, vol.QE-9, no.9, p.919–933 (1973)

21 Crump, PA "High efficiency, high power 808-nm laser array and stacked arrays optimized for elevated temperature operation," Proceedings of SPIE - The International Society for Optical Engineering; vol.5336, p.144-155 (2004)

22 See for instance: Coldren, LA; Corzine, SW "Diode lasers and photonic integrated circuits," ©Wiley, Inc. (1995)

23 See for instance: Wilmsen, C "Vertical-Cavity Surface-Emitting Lasers: Design, Fabrication, Characterization, and Applications," © Cambridge University Press (2001)

24 Ghatak, AK; Thyagarajan, K; Shenoy, MR "Numerical-analysis of planar optical wave-guides using matrix approach," IEEE Journal of Lightwave Technology; vol.5, no.5, p.660-667 (1987)

25 Macleod, HA "Thin Film Optical Filters," Macmillan Publications Co. (1986)

26 Miller, DAB "Advanced optoelectronic devices," ee343 course notes, Stanford University (Spr. 2002)

27 Stern, MS "Semivectorial polarised finite difference method for optical waveguides with arbitrary index profiles," IEE Proceedings J, vol.135, no.1, p.56–63 (1988)

28 Sabnis V, "Optically-controlled electroabsorption modulators for future generation optical networks," PhD Thesis, Stanford University (2003)

29 Yan, YC; Faber, AJ; deWaal, H; Kik, PG; Polman, A "Erbium-doped phosphate glass waveguide on silicon with 4.1 dB/cm gain at 1.535 μm," Applied Physics Letters; vol.71, no.20, p.2922-4 (1997)

30 Vurgaftman, I; Meyer, JR; Ram-Mohan, LR "Band parameters for III–V compound semiconductors and their alloys," Journal of Applied Physics; vol.89, p5815-5875 (2001)

31 Aspnes, DE; Kelso, SM; Logan, RA; Bhat, R "Optical properties of $Al_xGa_{1-x}As$," Journal of Applied Physics; vol.60, p.754-767 (1986)

32 Harris, JS "GaInNAs long-wavelength lasers: progress and challenges," Semiconductor Science and Technology; vol.17, no.8, p.880-891 (2002)

33 See for instance: Kasap, SO "Optoelectronics and photonics principles and practices," Prentice Hall Inc. (2001)

34 Spitzer, WG; Whelan, JM "Infrared absorption and electron effective mass in N-type gallium arsenide," Physical Review; vo.114, no.1, p.59-63 (1959)

35 Henry, CH; Logan, RA; Merritt, FR; Luongo, JP "The effect of intervalence band absorption on the thermal-behavior of InGaAsP lasers," IEEE Journal of Quantum Electronics; vol.19, no.6, p.947-952 (1983)

36 Hegblom, ER; Thibeault, BJ; Naone, RL; Coldren, LA "Vertical cavity lasers with tapered oxide apertures for low scattering loss," Electronics Letters; vol.33, no.10, p.869-71 (1997)

37 Giles, I "Optical Fiber Evanescent Field Components: An overlooked technology?," Fiberoptic product news; p.18-21, (Apr. 2004)

38 Tseng SM; Chen, CL "Side-polished fibers," Applied Optics; vol.31, p.3438 (1992)

39 Sharma, A; Kompella, J; Mishra, PK "Analysis of fiber directional couplers and coupler half-blocks using a new simple model for singlemode fibers," Journal of Lightwave Technology; vol.8, no.2, p.143-51 (1990)

40 Hamilton, SA; Yankelevich, DR; Knoesen, A; Weverka, RT; Hill, RA; Bjorklund, GC "Polymer in-line fiber modulators for broadband radio-frequency optical links," Journal of the Optical Society of America B; vol.15, no.2, p.740–750 (1998)

41 Mao, E "Semiconductor in-line fiber devices for optical communication systems," PhD Thesis, Stanford university (2000)

42 See for instance: Tong, QY; Gösele, U "Semiconductor Wafer Bonding: Science and Technology," ©Wiley Inc. (1998)

43 Johnstone, W; Stewart, G; Hart, T; Culshaw, B "Surface plasmon polaritons in thin metal films and their role in fiber optic polarizing devices," Journal of Lightwave Technology; vol.8, no.4, p.538-44 (1990)

44 Talghader, J; Smith, JS "Thermal dependence of the refractive index of GaAs and AlAs measured using semiconductor multilayer optical cavities," Applied Physics Letters; vol.66, no.3, p.335-7 (1995)

45 Matin P "The future looks bright for solid-state lighting," Laser Focus World (Sep. 2001)

46 Durhuus, T; Mikkelsen, B; Joergensen, C; Danielsen, SL; Stubkjar, KE "All-optical wavelength conversion by semiconductor optical amplifiers," IEEE Journal of Lightwave Technology; vol.14, p.942–954 (1996)

47 Kelly, AE; Tombling, C; Michie, C; Andonovic, I "High performance semiconductor optical amplifiers," Optical Fiber Communication Conference; vol.2 (OFC 23-27 Feb. 2004)

48 Ordal, MA; Bell, RJ; Alexander, RW; Long, LL; Querry MR "Optical properties of fourteen metals in the infrared and far infrared: Al, Co, Cu, Au, Fe, Pb, Mo, Ni, Pd, Pt, Ag, Ti, V, and W," Applied Optics; vol.24, p.4493 (1985)

49 Ordal, MA; Long, LL; Bell, RJ; Bell, SE; Bell, RR; Alexander, RW; Ward, CA "Optical properties of the metals Al, Co, Cu, Au, Fe, Pb, Ni, Pd, Pt, Ag, Ti, and W in the infrared and far infrared," Applied Optics; vol.22, p.1099 (1983)

50 Rode, DL; Willardson, RK; Beer, AC; editors "Semiconductors and Semimetals," vol.10, p.1, ©Academic Press, NY (1975)

51 Wiley, JD; Willardson, RK; Beer, AC; editors "Semiconductors and Semimetals," vol.10, p.91, ©Academic Press, NY (1975)

52 Wierer, JJ; Evans, PW; Holonyak, N; Kellogg DA "Lateral electron current operation of vertical cavity surface emitting lasers with buried tunnel contact hole sources" Applied Physics Letters; vol.71, p.3468 (1997)

53 Lear, KL; Hou, HQ; Banas, JJ; Hammons, BE; Furioli J; Osidski M "Vertical cavity lasers on p-doped substrates" Electronics Letters; vol.33, no.9, p.783 (1997)

54 Tai, K; Yang, L; Wang, H; Wynn, JD; Cho, AY "Drastic reduction of the series resistance in doped semiconductor distributed Bragg reflectors for surface emitting laser," Applied Physics Letters; vol.56, p.2496 (1990)

55 Choquette, KD; et. al. "Advances in Selective Wet Oxidation of AlGaAs Alloys" IEEE Journal of Selected Topics in Quantum Electronics; vol.3, no.3, p.916 (1997)

56 See for instance: Wolfe, CM; Stillman, N; Holonyak, GE "Physical Properties of Semiconductors" ©Prentice-Hall Inc. (1998)

57 Peters, MG; Thibeault, BJ; Young, DB; Gossard, AC; Coldren, LA "Growth of beryllium doped $Al_xGa_{1-x}As$/GaAs mirrors for vertical cavity surface emitting lasers" Journal of Vacuum Science and Technology B; vol.12, no.6, p.3075 (1994)